

MESOPAUSE WINDS AND OH INTENSITIES AT MID-LATITUDES—
FABRY-PEROT INTERFEROMETER OBSERVATIONS OF THE OH EMISSION AT
8430 Å FROM BEAR LAKE OBSERVATORY

by

Carolyn Marie Vadnais

A thesis submitted in partial fulfillment
of the requirements for the degree

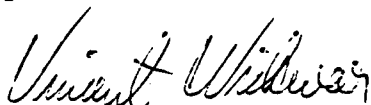
of

MASTER OF SCIENCE

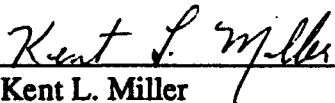
in

Physics
(Upper Atmospheric Physics)

Approved:



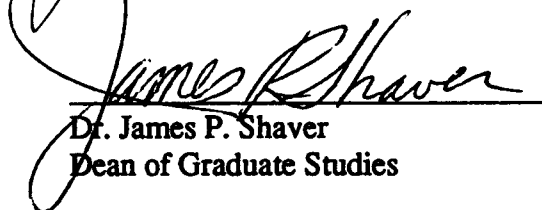
Dr. Vincent B. Wickwar
Major Professor



Dr. Kent L. Miller
Committee Member



Dr. James Wheeler
Committee Member



Dr. James P. Shaver
Dean of Graduate Studies

UTAH STATE UNIVERSITY
Logan, Utah

1993

Copyright © Carolyn Marie Vadnais 1993

All Rights Reserved

DTIC QUALITY INSPECTED 8

Accession For	
NTIS GRA&I	<input checked="checked" type="checkbox"/>
DTIC TAB	<input type="checkbox"/>
Unannounced	<input type="checkbox"/>
Justification	
By	
Distribution/	
Availability Codes	
Dist	Avail and/or Special
A-1	

ACKNOWLEDGMENTS

I would like to express my deep appreciation to Dr. Vincent Wickwar for his patience and willingness to help me not only to know, but to understand. I leave here with a much greater understanding and appreciation for the obstacles involved in scientific research, and in particular, the difficulties associated with making measurements which will be useful to anyone. Thank you also, Vince for the many things I learned which were totally unrelated to physics (nighttime carpentry, the effects of sleep deprivation, etc.). It has been quite an experience and I am sincere in saying that I am proud to have been associated with such a fine person.

Much of the credit for this project goes to the team at the Applied Physics Laboratory, University College of London. My sincere thanks to Anasuya Aruliah who answered countless questions about the data processing and who conceptually guided me through much of the data analysis.

Many thanks to Mike and Visnja Taylor for their analysis of the all-sky camera images which allowed intensity comparisons to be carried out with the Fabry-Perot. Their exactitude and his willingness to work under a tight deadline were commendable and greatly appreciated. Thank you also to Gary Swenson of Lockheed who allowed us to use his images.

Thank you to Pat Espy who produced some quick results from the Bomen Michelson Interferometer. His results were extremely useful, and discussions with Pat brought a greater understanding of the OH emission spectra to my thesis work.

As I leave here, I pass my duties as an employee of "Ian's Answering Service" to Devin Della-Rose. I'm sure he will maintain the high standards of service which are our benchmark, and take his responsibilities seriously.

The computer graphics program used to plot the winds and intensities presented in this thesis is due to the hard work of Ian Monson. Many thanks to Ian for putting up with the many failures which eventually lead to this success.

A very special thanks goes to my husband, Scott, who supported me throughout this "adventure." His patience and understanding made our separation much more bearable. Your absence truly did make my heart grow fonder. Ohio here I come....

Carolyn Marie Vadnais

CONTENTS

ACKNOWLEDGMENTS	ii
LIST OF TABLES	vii
LIST OF FIGURES	viii
LIST OF SYMBOLS	xiii
ABSTRACT.....	xv
Chapter	
1. INTRODUCTION AND BACKGROUND	1
2. THE MESOPAUSE REGION.....	4
2.1 Temperature Structure	4
2.2 The Mesopause	5
2.3 Mean Wind Structure.....	6
2.4 Waves Observed in the Mesopause Region	8
2.4.1 Acoustic Gravity Waves.....	10
2.4.2 Atmospheric Tides	15
2.4.3 Planetary Waves.....	36
2.5 Airglow vs. Auroral Activity	43
2.6 Altitude of OH Airglow Emissions	44
2.7 Mechanisms for OH Airglow	44
3. EMISSION SPECTRA.....	48
3.1 Emissions Observed in the Mesopause Region.....	51
3.2 Emission Line Profiles.....	52
3.2.1 Doppler Broadening.....	53
3.2.2 Pressure Broadening.....	55
3.3 The Observed OH Profile.....	55
4. FABRY-PEROT IMAGES AND INTERFEROMETRY.....	58
4.1 The Interference Intensity Pattern	58
4.1.1 Transmission Through an Ideal Etalon	58

	v
4.1.2 Reflectance.....	63
4.1.3 Instrument Finesse	64
4.1.4 Order of Interference.....	65
4.2 Reducing the Two-Dimensional Images.....	67
4.2.1 Center Coordinates of the Image	68
4.3 Free Spectral Range	68
4.4 Spectral Resolution	71
4.5 Effective Finesse Calculation from the Data.....	71
5. HARDWARE.....	73
5.1 The Fabry-Perot Interferometer.....	73
5.1.1. The Scanning Mirror System.....	73
5.1.2 The Etalon.....	78
5.1.3 The Lens System.....	80
5.1.4 The Imaging Photon Detector.....	82
5.1.5 The Calibration Sources	88
5.1.6 Interference Filters and Filter Wheel System.....	88
5.1.7 The He-Ne Laser.....	91
5.1.8 Temperature Control and Instrument Stability	93
5.1.9 The Computer and Software.....	93
5.2 List of Instrument Parameters	95
6. THE QUEST FOR WIND VELOCITIES	97
6.1 Data Processing	97
6.1.1 Fourier Analysis.....	97
6.1.2 Peak Positions	104
6.1.3 Peak Height.....	107
6.2 Wind Determination.....	107
6.2.1 Determining the Zero Doppler Shift—Position/Baseline	108
6.2.2 Wind Velocities from Doppler Shifts	112
6.2.3 Total Error in the Calculated Wind Speed	113
6.3 Presentation of Wind Data	114
7. ANALYSIS.....	116

	vi
7.1 Observations of 8430 Å OH Near The Mesopause	116
7.1.1 Interpretation of Clouds.....	135
7.1.2 UARS	137
7.2 Observations in the F-Region.....	138
7.2.1 6300 Å O(1D) Intensities and Winds.....	138
7.3 Instrumental Drift	149
7.4 Zenith Winds	150
8. OH INTENSITY ANALYSIS.....	151
8.1 Background Intensity	151
8.2 Relative Intensities.....	152
8.3 Intensity Comparisons.....	154
8.3.1 The All-Sky Imager	154
8.3.2 The Bomen Michelson Interferometer	156
9. MESOSPHERIC TEMPERATURES	164
9.1 Recovering the Emission Line.....	164
9.1.1 Find the Instrument Profile.....	165
9.1.2 Create the Analytic Function (Gaussian)	165
9.1.3 Convolve the Laser Profile and the Double Gaussian	165
9.1.4 Comparison of Fabry-Perot and Michelson Temperatures	166
9.2 Current Progress	166
10. POTENTIAL FOR FUTURE RESEARCH.....	168
REFERENCES	171
APPENDICES	176

LIST OF TABLES

Table		Page
1	Average Zonal Winds at 85 km by Month at Garchy, France ($\sim 44^\circ\text{N}$).	7
2a	Gravity Wave Results	16
2b	Observation Parameters for Gravity Waves.....	16
3	Diurnal and Semidiurnal Tidal Mode Parameters.....	27
4	Semidiurnal Tidal Wind Components at 42° Latitude	29
5	Diurnal Tidal Wind Components at 42° Latitude	29
6a	Diurnal Tide Results	31
6b	Semidiurnal Tide Results	33
6c	Terdiurnal Tide Results.....	34
7	Observation Parameters	35
8	Planetary Waves	43
9	Filter Center Wavelength and Full-Width at Half-Maximum Power.....	90
10	Number of Frequency Components Used.....	104
11	Kp Indices for 6300 Å Data Analysis.....	138
12	A Indices for 6300 Å Data Analysis.....	138

LIST OF FIGURES

Figure		Page
1	Schematic latitude-height section of zonal mean temperatures ($^{\circ}\text{C}$) for solstice condition. Dashed lines indicate tropopause, stratopause, and mesopause levels [Andrews et al., 1987].	4
2	Schematic latitude-height section of zonal mean zonal wind (m/s) for solstice conditions; W and E designate centers of westerly (from the west) and easterly (from the east) winds, respectively [Andrews et al., 1987].	7
3	Near Infrared OH nightglow wave structure observed from Sacramento Peak, NM, June 1983. The image was obtained in 0.5 seconds using a low-light TV system fitted with a 30° by 20° field of view lens.	9
4	Symmetric Hough functions for the migrating solar diurnal thermal tide. Also shown is $\sin\theta\cos\theta$, the most important odd mode [After Lindzen, 1971].	22
5	Vertical wavelength of each tidal mode (s,n). (a) diurnal, (b) semidiurnal [Kato, 1980].	24
6a	Hough decomposition of diurnal heating rates vs. height during equinox (left) and December solstice (right) due to insolation absorption by H_2O (lower scales) and O_3 (upper scales) in units of W/kg multiplied by $\exp(-x/2)$, where $x=\ln(p/p_0)$ [Forbes, 1982]	26
6b	Hough decomposition of semidiurnal heating rates vs. height. Otherwise as in figure 6a [Forbes, 1982].	26
7	(a) Amplitudes of the southward components (or eastward component for the steady wind) at 45° latitude from Richmond's research. (b) Phases of southward components at 45° latitude [Richmond et al., 1976].	30
8	50-mb height field (solid contours in 100's of feet) and temperature field (dashed contours in $^{\circ}\text{C}$) in (a) January and (b) February [Holton, 1979].	38

9	The amplitude Ψ in units of $10^3 \text{ m}^2\text{s}^{-1}$ for a stationary planetary wave on the mid-latitude beta-plane as a function of mean zonal wind speed and wavelength, for $f_0=10^{-4}\text{s}^{-1}$, $\beta=1.6 \times 10^{-11}\text{m}^{-1}\text{s}^{-1}$, $H=7 \times 10^3\text{m}$, $N=.02 \text{ s}^{-1}$ and $h_t = 1.25 \text{ km}$. [After Hirota, 1971].....	41
10	Rotational Band Structure for the Meinel (6-2) OH band [Figure courtesy of Pat Espy].	50
11	Hyperfine doublet of the 8430 Å OH emission [Figure courtesy of Pat Espy and Mark Hammond].....	51
12	Doppler and Lorentz line shapes for approximately equal half-widths and intensities with the corresponding Voigt profile [Andrews et al., 1987].	55
13	Fabry-Perot circular fringe pattern of the OH emission at 8430 Å.	59
14	Reflection and transmission between two parallel plates.....	60
15	Airy Disk [After Hecht, 1987].	62
16	Intensity variation with reflectance for three values of R; 0.3, 0.6, 0.9. [After Tolansky, 1955].	64
17	One-dimensional fringe profile.....	67
18	Bear Lake Observatory and the location of the Imaging Fabry-Perot interferometer.	74
19	The Imaging Fabry-Perot interferometer and components.	75
20	Transmittance curve for the etalon plate coating.....	79
21	The Fabry-Perot lens system and focal lengths.	81
22	Spectral response curve for the Bear Lake Observatory detector.....	83
23	(a): Thermionic emission calibration, (b): Flat Field calibration at 8430 Å, (c): Uncorrected one-dimensional OH spectrum, and (d): Corrected spectrum.	87
24	Calibration lamp and OH 8430 Å fringe.....	89
25	Manufacturer's transmittance curve for the 8432 Å filter for normal incidence.	92

26	Raw fringe profiles. (a) 8430 Å (b) 6300 Å.....	98
27	Fourier smoothing of the raw data. (a) 8430 Å, (b) 6300 Å.	100
28	Power Spectral Density for 8430 Å OH. The zero frequency component was omitted to allow a better scale.	102
29	The range of stability for the calculated peak position as a function of cutoff frequency. The numbers along the bottom axis of these plots are the total number of frequency components, real and imaginary.	103
30	Three estimates of the zero velocity position.	112
31	Relative background (top) and OH (bottom) intensities observed near 87 km from Bear Lake Observatory on 9 Jan 92.	117
32	Zonal (top) and meridional (bottom) neutral wind components observed near 87 km from Bear Lake Observatory on 9 Jan 92.	118
33	Relative background (top) and OH (bottom) intensities observed near 87 km from Bear Lake Observatory on 10 Jan 92.	120
34	Zonal (top) and meridional (bottom) neutral wind components observed near 87 km from Bear Lake Observatory on 10 Jan 92.	121
35	Relative background (top) and OH (bottom) intensities observed near 87 km from Bear Lake Observatory on 12 Jan 92.	123
36	Zonal (top) and meridional (bottom) neutral wind components observed near 87 km from Bear Lake Observatory on 12 Jan 92.	124
37	Relative background (top) and OH (bottom) intensities observed near 87 km from Bear Lake Observatory on 30 Jan 92.	125
38	Zonal (top) and meridional (bottom) neutral wind components observed near 87 km from Bear Lake Observatory on 30 Jan 92.	126
39	Relative background (top) and OH (bottom) intensities observed near 87 km from Bear Lake Observatory on 5 Feb 92.	127
40	Zonal (top) and meridional (bottom) neutral wind components observed near 87 km from Bear Lake Observatory on 5 Feb 92.....	129

41	Relative background (top) and OH (bottom) intensities observed near 87 km from Bear Lake Observatory on 27 Dec 91.	130
42	Zonal (top) and meridional (bottom) neutral wind components observed near 87 km from Bear Lake Observatory on 27 Dec 91.	131
43	Relative background (top) and OH (bottom) intensities observed near 87 km from Bear Lake Observatory on 28 Dec 91.	132
44	Zonal (top) and meridional (bottom) neutral wind components observed near 87 km from Bear Lake Observatory on 28 Dec 91.	133
45	Relative background (top) and OH (bottom) intensities observed near 87 km from Bear Lake Observatory on 30 Dec 91.	134
46	Zonal (top) and meridional (bottom) neutral wind components observed near 87 km from Bear Lake Observatory on 30 Dec 91.	136
47	Relative background (top) and O(1D) (bottom) intensities observed near 250 km from Bear Lake Observatory on 28 Feb 92.	140
48	Zonal (top) and meridional (bottom) neutral wind components observed near 250 km from Bear Lake Observatory on 28 Feb 92.	141
49	Relative background (top) and O(1D) (bottom) intensities observed near 250 km from Bear Lake Observatory on 29 Feb 92.	142
50	Zonal (top) and meridional (bottom) neutral wind components observed near 250 km from Bear Lake Observatory on 29 Feb 92.	143
51	Relative background (top) and O(1D) (bottom) intensities observed near 250 km from Bear Lake Observatory on 1 Mar 92.	145
52	Zonal (top) and meridional (bottom) neutral wind components observed near 250 km from Bear Lake Observatory on 1 Mar 92.	146
53	Relative background (top) and O(1D) (bottom) intensities observed near 250 km from Bear Lake Observatory on 27 Jan 92.	147
54	Zonal (top) and meridional (bottom) neutral wind components observed near 250 km from Bear Lake Observatory on 27 Jan 92.	148
55	The background intensity at 8430 Å.	151
56	Intensity and background variations for 5 Feb 92.	153

57	Image taken by an All-sky imager at the Bear Lake Observatory on 5 Feb 92 [Photo compliments of Mike Taylor].	155
58	a and b Relative intensity comparison between the All-Sky Imager (solid curve) and the Fabry-Perot interferometer (dashed curve), 5 Feb 92.	157
	c and d Relative intensity comparison between the All-Sky Imager (solid curve) and the Fabry-Perot interferometer (dashed curve), 5 Feb 92.	158
	e and f Relative intensity comparison between the All-Sky Imager (solid curve) and the Fabry-Perot interferometer (dashed curve), 5 Feb 92.	159
	g and h Relative intensity comparison between the All-Sky Imager (solid curve) and the Fabry-Perot interferometer (dashed curve), 6 Feb 92.	160
	i and j Relative intensity comparison between the All-Sky Imager (solid curve) and the Fabry-Perot interferometer (dashed curve), 6 Feb 92.	161
	k and l Relative intensity comparison between the All-Sky Imager (solid curve) and the Fabry-Perot interferometer (dashed curve), 6 Feb 92.	162
59	Relative intensity comparison between the Bomem Michelson interferometer (solid curve) and the Fabry-Perot interferometer (dashed curve), 5 Feb 92 (top) and 6 Feb 92 (bottom).	163

LIST OF SYMBOLS

A	absorbance
c	local acoustic speed (Chapter 2)
c	speed of light (Chapter 4)
D	diameter of the collecting aperture
d	path difference between successive transmitted beams
F	coefficient of finesse
FOV	field of view
FSR	free spectral range
\mathcal{F}	finesse
f	focal length (except Chapter 2)
f	Coriolis parameter (Chapter 2)
f_l	local Coriolis frequency
g	gravitational acceleration
H	scale height
HWHH	half-width at half-height
h	equivalent depth
h	Planck's constant
h_n	equivalent depth for a particular tidal mode
IPD	imaging photon detector
ITT	company that produced the photomultiplier tube
IFPI	imaging Fabry-Perot interferometer
I_t	transmitted intensity
I_i	incident intensity
k	horizontal wave number
k	Boltzmann constant (Chapter 3 where indicated)
L	effective focal length
l	meridional wave number
M	molecular mass
m	vertical wave number
N	Brunt-Vaisala frequency, buoyancy frequency
n	meridional wave number (Chapter 2)
n	order of interference (Chapter 4)
n_0	central order of interference
p	pressure
p_0	reference pressure
t	etalon plate separation
\mathcal{R}	resolving power
R	reflectance
r_n	radius to fringe at order of interference n
s	zonal wave number
T	transmittance (Chapter 5)
T	absolute temperature (Chapter 3)

\bar{u}	mean wind velocity
UCL	University College London
U_c	Rossby critical velocity
z	geopotential height
β	first derivative of the Coriolis parameter with respect to longitude
δ	phase difference between successive transmitted beams
γ	specific heat ratio (Chapter 2)
γ	half-width of the transmitted fringe intensity (except Chapter 2)
λ_0	wavelength of the incident radiation
λ_z	vertical wavelength
μ	index of refraction between the etalon plates
ν	frequency
Ω	angular frequency
Ω_E	angular frequency of earth's rotation
π	constant=3.1415926
ρ	particle density
τ	mean time between collisions
Θ	Hough function
θ	angle of incidence
ω	angular frequency
Ψ	amplitude of wave perturbation

ABSTRACT

Mesopause Winds and OH Intensities at Mid-Latitudes--
Fabry-Perot Interferometer Observations of the OH Emission
at 8430 Å From Bear Lake Observatory

by

Carolyn M. Vадnais, Master of Science
Utah State University, 1993

Major Professor: Dr. Vincent B. Wickwar
Department: Physics

Observations were made from Bear Lake Observatory (41.935° N, 111.422° W) of the OH 8430 Å emission from 87 km and the O(¹D) 6300 Å emission from 250 km using an Imaging Fabry-Perot Interferometer. Neutral winds were derived from the Doppler shift of the emission line, and relative intensity was also analyzed. Results presented are from the period between December 1991 and March 1992.

The 8430 Å OH data showed remarkable day-to-day variability in the wind pattern. Diurnal, semidiurnal, and terdiurnal tidal components all appeared at some point during the observing period with no consistent regularity. The OH intensities showed the presence of gravity wave activity with discernible periods down to approximately 3 hours.

The 6300 Å O(¹D) wind and intensity observations showed a high degree of magnetic activity which correlated positively with K_p and A_p indices. We noted a definite presence of auroral and SAR-arc activity almost nightly on nights when the 6300 Å O(¹D) emission was observed.

(200 pages)

CHAPTER 1

INTRODUCTION AND BACKGROUND

The wind and temperature structure of the upper mesosphere and the lower thermosphere is very complex and shows great variability [von Zahn and Kurzawa; 1989; Geller, 1983]. The primary source of this variability is related to the propagation, coupling, and dissipation of waves in the region. Waves observed in this region include tides, gravity waves, and planetary waves. The interaction of these waves with each other produces variations in the winds and temperature structure. Their interaction with the mean background wind flow results in exchange of energy and momentum and subsequently affects the energy balance of the region. These processes are also thought to play a large role in the coupling between the middle atmosphere and the lower thermosphere.

Like the thermosphere, this region can be studied optically with Fabry-Perot interferometers for winds, intensities, and temperatures. The O(¹S) emission at 5577 Å has been observed extensively with a Fabry-Perot interferometer for the study of temperature near 97 km [e.g., Hernandez, 1976]. The possibility of measuring winds with Fabry-Perot observations of the OH Meinel emission bands from near 87 km [Baker and Stair, 1988] was demonstrated by Hernandez and Smith [1984]. However, they required 2-hour integration times. Recent advances in detector technology now make it possible to make these observations in 4 minutes. These developments also include the development of the Gallium-Arsenide (GaAs) photocathode, which is the first to sustain a high sensitivity well into the near infrared [McWhirter et al., 1982], to about 850 nm. This photocathode has been combined with an imaging detector, an Imaging Photon Detector (IPD) by ITT, to observe a whole free spectral range simultaneously [Rees et

al., 1990]. This combination enables the $P_1(3)$ line in the (6-2) band at 8430 Å to be observed with 4-minute time resolution [Rees *et al.*, 1990].

The instrument described above is located at the Bear Lake Observatory (BLO) 38 km from Utah State University (USU) at 41.935° N, 111.422° W, and 1990 meters altitude. It is operated as a collaborative project of USU (Vincent B. Wickwar) and University College of London (David Rees). Observations began on the USU campus in August 1988. However, they were of the 6300 Å thermospheric emission from atomic oxygen. When the first new GaAs detector became available the following year, the Imaging Fabry-Perot Interferometer (IFPI) was moved to BLO and OH observations began in September 1989. Initial wind results were presented at the American Geophysical Union meeting in December 1989 and, as mentioned, published in 1990 [Rees *et al.*, 1990].

Initially, the intent of this project was to implement the UCL data-reduction programs for winds at USU and then to extend the measurement technique and analysis to determine temperatures. However, because the task of implementing the data-reduction programs and optimizing them for mid-latitude mesopause observations (instead of high-latitude thermospheric observations) turned out to be such an enormous task, the temperature analysis has not been completed. One of the major difficulties encountered was converting the wind analysis programs from VMS format to one suitable for running on a PC. This required extensive modification, but the analysis system is now operational at USU for OH winds and intensities from the mesopause region and $O(^1D)$ winds and intensities from the thermosphere. New data have been reduced and examined, comparisons have been made with other instruments, and the groundwork has been laid for a future temperature capability.

Chapter 2 will review mesopause dynamics and OH airglow emission. It provides background for the observations and interpretation as well as motivation for

studying the middle atmosphere. Chapter 3 provides more specific information about 8430 Å OH emission. Chapter 4 gives a detailed description of the Fabry-Perot interferometer. Chapter 5 describes the subsystems of the IFPI. Chapters 6 through 8 give detailed descriptions of the analysis techniques for intensities and winds, and results of both OH and O(¹D) observations. Chapter 9 introduces the topic of temperature analysis. Chapter 10 discusses potential future research topics.

CHAPTER 2

THE MESOPAUSE REGION

2.1 Temperature Structure

The term "mesopause region" is used here to mean the region between the uppermost mesosphere and lowermost thermosphere, where the lowest temperatures in the atmosphere exist. In the mid-latitudes, this minimum varies from about 180° K in the summer hemisphere to near 240° K in the winter hemisphere. The largest annual variations in mesospheric temperatures are found at high latitudes with smaller differences toward the equator. However, the pattern of winter maximums and summer minimums holds true at all latitudes [Meriwether, 1984]. The temperature structure for the atmosphere below 100 km is shown in Figure 1.

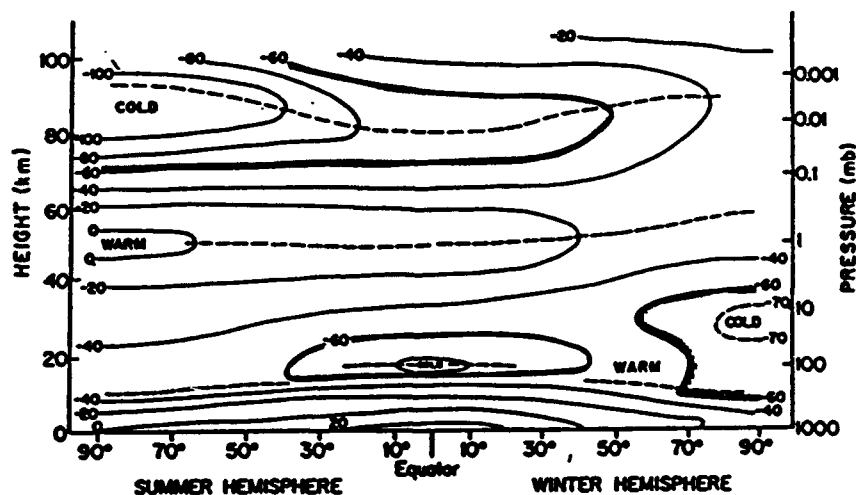


Fig. 1. Schematic latitude-height section of zonal mean temperatures ($^{\circ}$ C) for solstice condition. Dashed lines indicate tropopause, stratopause, and mesopause levels [Andrews et al., 1987].

The general temperature structure of the middle atmosphere can be approximately explained in terms of absorption and emission. Net heating depends almost exclusively on the imbalance between local absorption of solar ultraviolet (UV) and infrared (IR) radiative loss. In the middle atmosphere, ozone and O_2 are the dominant absorbers and carbon dioxide is the dominant emitter [Andrews *et al.*, 1987]. The maximum temperature, which defines the stratopause, is due primarily to the absorption of solar UV radiation by ozone which has maximum concentrations between 25 and 40 km. The great drop in temperature above this layer occurs because of the sharp decrease in ozone concentration with height, and the lack of any other compensating absorbing constituent.

The temperature minimum that defines the mesopause is vertically well-defined in the summer, but exists as a broad minimum during the winter [e.g., CIRA, 1972]. The presence of a sharp temperature gradient in the atmosphere can affect the propagation of waves, resulting in their reflection under certain conditions and absorption in others. Wave activity is known to greatly affect the energy balance between 80 and 120 km [Geller, 1983].

2.2 The Mesopause

von Zahn and Kurzawa [1989] found the average height of the mesopause to be between 90 and 95 km. The exact height of the mesopause is, of course, not constant and varies strongly with the season. To date, little data have been collected in this region due to the difficulties involved in making measurements there.

The in situ data which have been collected in this region were obtained using a variety of rocket techniques. These include the use of falling spheres, grenades, pressure gauges, pitot tubes, and chemical releases [CIRA, 1972]. In addition to being expensive, these methods involve somewhat complex data reduction and do not provide the continuous sampling required for time resolution of many phenomena important to the region such as gravity waves and atmospheric tides. To get this resolution it is necessary

to use remote sensing techniques. One of the earliest ground-based techniques which was used successfully was the meteor-radar method. This involves reflecting radio waves off of meteor ionization trails to obtain a Doppler shift, which can then be converted to a wind velocity. These meteor trails occur naturally between 80 and 100 km, and hence the region is sometimes referred to as the meteor region. Their presence has added greatly to the understanding of this region.

Modern optical instruments take advantage of the many natural atomic and molecular emissions that occur in the mesopause region. These include the OH Meinel band systems, the O₂ Atmospheric band systems, the O(¹S) emission at 5577 Å, and various metallic emissions [Meriwether, 1989]. These emissions provide a built-in avenue for the region to be observed and studied using optical instruments such as the Fabry-Perot interferometer, the Michelson interferometer, and a variety of cameras. In addition to ground-based remote sensing, instruments can also be placed on satellites. These measure emissions by doing limb scans through the emission altitude. Currently a Michelson interferometer on board the UARS satellite (WINDII) is being used to measure airglow emissions, including the OH (8,3) emission band.

2.3 Mean Wind Structure

The waves and tides observed in the mesopause region are superimposed on a mean background wind of some magnitude. One way to estimate the mean zonal winds at a particular latitude is to look at the long-term average. This is shown in Figure 2 for solstice conditions.

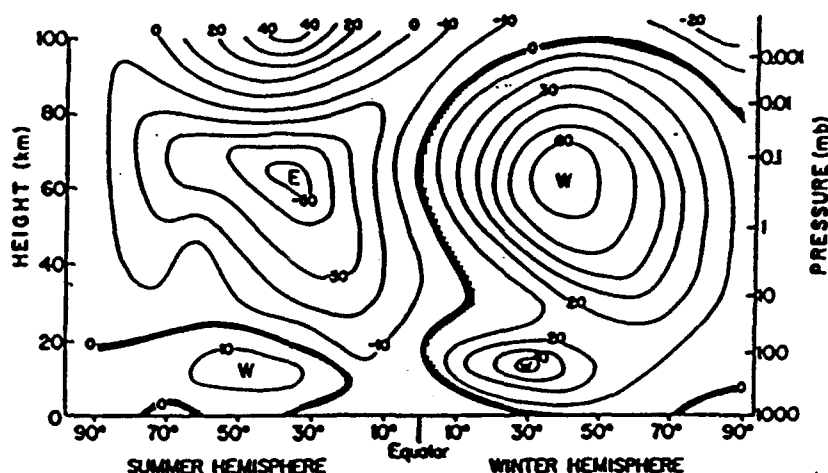


Fig. 2. Schematic latitude-height section of zonal mean zonal wind (m/s) for solstice conditions; W and E designate centers of westerly (from the west) and easterly (from the east) winds, respectively [Andrews *et al.*, 1987].

To get an idea of what the magnitude of the average zonal winds might be over Utah ($\sim 42^\circ$ N) it is reasonable to look at the winds measured at a similar latitude by month. Table 1 shows mean zonal winds over Garchy, France ($\sim 44^\circ$ N) at 85 km, where positive speeds represent flow to the east, and negative speeds represent flow to the west.

TABLE 1. Average Zonal Winds at 85 km by Month at Garchy, France ($\sim 44^\circ$ N).

Month	J	F	M	A	*	M	J	J	*	A	S	O	N	D
mean zonal wind (m/s)	30	25	20	10	0	-10	-10	-5	0	12	22	30	30	30

Note: Taken from Forbes and Vial [1989]

A dominant feature of the winds in the mesopause region is the seasonal wind reversal, which occurs near equinox periods and gives summer easterlies (winds from the east) and winter westerlies (winds from the west). This suggests that during equinoctial conditions the zonal winds should be very weak in both hemispheres.

The wind reversal for spring occurred between April and May and in the fall between July and August at Garchy. These numbers are presented as an indication of the expected prevailing wind over the Bear Lake Observatory. There may be longitudinal differences between the two sites, however, which are not accounted for here. Also it should be realized that there are differences in what would be obtained by averaging for 24 hours, whereas the IFPI winds can only be averaged for 12 hours.

Vertical velocities near the mid-latitude mesopause have been investigated by *Franke et al.* [1990]. Using simultaneous measurements by a sodium lidar and an MF Doppler radar, they found that in the region between 76 and 100 km vertical velocities were typically 30 to 50 cm/s with maximum velocities of ~ 2 m/s. These velocities were assumed to be associated with wave structure.

2.4 Waves Observed in the Mesopause Region

The existence of wave activity at mesopause heights is well documented [*Forbes and Vial*, 1989; *Manson et al.*, 1989; *Gardner et al.*, 1988; *Taylor et al.*, 1987; *Geller*, 1983; *Hauchecorne and Chanin*, 1983; *Hooke*, 1977]. Observations in this region have shown a distinct wave-like structure that exhibits the presence of many waves of different scale sizes [*Taylor et al.*, 1987; *Taylor and Hapgood*, 1990]. Figure 3 was taken over Sacramento Peak, NM in June, 1983. It shows wave structure apparent in the OH nightglow near 87 km.

Three primary types of waves are observed superimposed on the zonal flow in the mid-latitude mesopause region. These are gravity waves with periods of 4 minutes to 6 hours, tides with periods of 6-24 hours, and planetary waves with periods greater than 1.5 days.

In general, waves occur because the atmosphere is stably stratified. When there is a displacement from equilibrium, gravity acts to restore the equilibrium state, causing oscillations to occur and be sustained if the frequency of the perturbation is less than a

particular maximum frequency, called the Brunt-Vaisala frequency. Waves in this category will propagate in the absence of dissipation. They will be briefly covered in this section.



Fig. 3. Near Infrared OH nightglow wave structure observed from Sacramento Peak, NM, June 1983. The image was obtained in 0.5 seconds using a low-light TV system fitted with a 30° by 20° field of view lens. The horizontal wavelength of the nightglow pattern was 23 ± 1 km and the display moved with a uniform velocity of 28 ± 2 m/s, indicating an apparent wave period of 13.7 ± 1.2 min [Taylor et al., 1991].

General equations of motions along with appropriate boundary and initial conditions can describe the wave motions observed at the mesopause. The necessary equations come from the general equations for conservation of momentum, energy and matter, and an equation of state. Because the equations of motion depend in different ways on spatial and temporal derivatives of the pressure, density, temperature, and velocity fields, different terms in the equations are important to different types of phenomena, depending on their scale size and time variation. This is the principal reason that planetary waves, tides, and gravity waves all show a distinct character. Simplifications to the general equations of motion are obtained through scale analysis and can be found in any basic text on wave phenomena.

Waves can be generated at any altitude, but all else being equal, waves generated below the height of observation will tend to dominate because the energy density of the wave ($1/2\rho u^2$) remains constant with height. Since density decreases as $\rho e^{(-h/H)}$, the amplitude of the wave must increase to conserve energy. This is only true when a wave propagates vertically in the absence of dissipative forces. The increase in amplitude eventually leads to "breaking" of the wave into smaller scale sizes and an exchange of energy and momentum to the surrounding medium [Lindzen, 1990]. Breaking occurs either when wave speeds approach the local speed of sound, or when their speed becomes the same as that of the background flow [Holton, 1979]. These processes are important and are the focus of much current research. Waves with upward energy transport tend to dominate the observations of every level in the upper atmosphere [Hooke, 1977].

2.4.1 Acoustic Gravity Waves

2.4.1.1 Production of Gravity Waves

Gravity waves occur at all heights in the atmosphere and are the smallest-scale feature that can be resolved by Fabry-Perot measurements. Common phenomena which are thought to generate gravity waves include thunderstorms, frontal systems, jet stream

instabilities and turbulence, wind blowing over mountains and land masses (topographical forcing), auroral activity, and volcanic and nuclear explosions.

Probably the single most important source mechanism for gravity wave motions is shearing instability of large-scale flow, i.e., the breakdown of large-scale features into smaller scale sizes. This serves to limit the intensification of vertically propagating waves.

2.4.1.2 Simplifying Assumptions and Equations of Motion

Gravity waves occur on scales much smaller than the earth's radius, with periods much less than a day. As a result, the earth's curvature and rotation play a minor role in their description, and the Coriolis force as well as the spherical geometry can be neglected. The actual criterion for neglecting the Coriolis force is that the period of the wave being considered must be less than the local inertial period at the latitude of interest. The local inertial period is found from $T_i = 2\pi/f_i$, where $f_i = 2\Omega \sin\theta$ is the Coriolis frequency, Ω is the rotation rate of the earth, and θ is latitude. At 42° N the local inertial period is approximately 18 hours, and so neglecting the Coriolis force should be a reasonable approximation for gravity waves.

In the derivation, the atmosphere is considered locally isothermal, meaning the scale height H is assumed constant. The motion of gravity waves is neither geostrophic nor hydrostatic because they occur on short time scales and vertical accelerations cannot be neglected. To simplify the mathematics the basic state is assumed to be at rest. This is reasonable since the horizontal speeds of gravity waves will be much greater than the mean wind speed at 87 km.

These assumptions produce the following set of equations as given by Beer [1974].

$$\frac{\partial \bar{u}}{\partial t} = g - \frac{1}{\rho} \nabla p$$

$$\frac{\partial \rho}{\partial t} + \nabla \cdot (\rho \bar{u}) = 0$$

$$\frac{\partial p}{\partial t} + \bar{u} \cdot \nabla p = c^2 \left(\frac{\partial \rho}{\partial t} + \bar{u} \cdot \nabla \rho \right) \quad (2.1)$$

This form of the adiabatic energy equation includes the term c^2 , which has been substituted for $\gamma p/\rho$ and is the local acoustic speed. The coordinate system is oriented with u eastward, v northward, and w upward. Combining these and extracting the first order equations gives

$$\frac{\partial}{\partial t^2} \left(\frac{\partial^2 \psi}{\partial x^2} + \frac{\partial^2 \psi}{\partial z^2} \right) + N^2 \frac{\partial^2 \psi}{\partial x^2} = 0 \quad (2.2)$$

where ψ is used to represent any perturbed quantity such as pressure or density. This is the wave equation for gravity waves.

2.4.1.3 The Buoyancy Frequency, N

Above, the parameter N has been substituted for $g^2(\gamma-1)/c^2$ in deriving the wave equation, where γ is the ratio of specific heats. This term is the buoyancy frequency, also called the Brunt-Vaisala frequency. The buoyancy frequency is defined for a stably stratified fluid, as the natural frequency an element will oscillate at if displaced from equilibrium. This results in a simple harmonic motion [Lindzen, 1990]. The Brunt-Vaisala frequency is used because it is a convenient measure of stability in studying atmospheric dynamics. For an isothermal atmosphere N can also be expressed as:

$$N^2 = \frac{g(1 - \frac{1}{\gamma})}{H} \quad (2.3)$$

At 85 km altitude, assuming a specific heat ratio of 1.4 and a mean scale height of 6 km, the buoyancy frequency at 85 km will be approximately 0.02 s^{-1} . Just as the local inertial frequency defined the lower frequency limit, N defines the upper frequency limit for internal gravity waves.

The buoyancy frequency depends only on the thermal structure of the medium. If an element is displaced vertically, and the restoring forces are allowed to act, the parcel

will oscillate at the buoyancy frequency, and the motion will be purely vertical. In this case, the perturbation frequency ω is equal to N and the parcel will oscillate about the position from which it was initially displaced. There will be no vertical phase variation and no vertical propagation of the wave.

When the frequency of the oscillation is larger than the buoyancy frequency $\omega > N$, the buoyancy force is inadequate to sustain the oscillation and the perturbation decays with height [Lindzen, 1990].

For a fluid excited at a frequency ω , where $\omega < N$, pressure forces constrain the fluid to move at an angle θ with respect to the vertical such that only a projection of the buoyancy force in the vertical constitutes the restoring force. The angle is found from $\theta = \cos^{-1}(\omega/N)$. The angle of fluid motion depends only on the frequency of the excitation. When $\omega < N$, phase will change with height and the wave will have a vertical structure. These waves that occur when $\omega < N$ are internal gravity waves.

Where θ is large ($\omega \ll N$), phase changes rapidly with height which corresponds to short vertical wavelengths and rapid vertical energy propagation. Where θ is small ($\omega \sim N$), there are large vertical wavelengths, and most of the energy is transported horizontally.

An observer viewing the propagation of an internal gravity wave would see that even though energy transport is upward, the apparent phase propagation is downward.

2.4.1.4 Determining the Solution and Dispersion Relation

To solve the wave equation, a solution of the form $\psi = \psi_0 \exp[i(\omega t - kx - mz)]$ is assumed, where ψ is the wave (perturbation) amplitude, k is the horizontal wave number, m is the vertical wave number, and ω is assumed positive traveling eastward. This solution represents a two-dimensional plane wave which varies in the vertical direction and in one horizontal direction only. The solution gives the dispersion relation for gravity waves

$$\omega = \pm \frac{Nk}{(k^2 + m^2)^{1/2}} \quad (2.4)$$

The dispersion relation gives the permissible relationships between the frequency of the wave and its horizontal and vertical wavelength components. For propagating waves, the phase will vary with height and the wave will have a finite vertical wavelength, defined as that distance over which the phase changes by 360° . In a stably stratified atmosphere, where dissipation is not dominant, any excitation with frequency components between N and f_1 will excite internal gravity waves.

For gravity waves, the dispersion relation will always have complex coefficients and there will be no solutions with purely real wave numbers. The vertical wave number m is complex with the form $(m + i/2H)$ and m is real. This is an internal wave and its amplitude will increase upward with height as $\exp(h/2H)$ due to the positive imaginary part of m .

The final solution is

$$\Psi = \Psi_0 e^{\frac{z}{2H}} e^{[i(\omega t - kx - mz)]} \quad (2.5)$$

For an isothermal atmosphere, the amplification will mean that the z dependence is no longer purely sinusoidal and the actual dispersion relation will be

$$m^2 = k^2 \left(\frac{N^2}{\omega^2} - 1 \right) - \frac{1}{4H^2} \quad (2.6)$$

2.4.1.5 Gravity Wave Observations in the Mid-Latitude Mesopause Region

Gravity waves with periods of ~ 5 minutes to ~ 18 hours have been observed in the mesopause region worldwide. Winter usually exhibits more activity than summer, but their occurrence is seen continually. Gravity waves are observed frequently during the winter in OH images over Bear Lake [Swenson, private communication, 1992]. It is not yet clear whether the frequency is enhanced by orographic forcing due to the mountainous location. Seasonal dependence of gravity wave activity is quite dramatic as

was shown by *Hauchecorne and Chanin* [1983] using the variability of lidar measurements, with the winter showing much heavier gravity wave activity.

Table 2a summarizes the gravity wave parameters from seven separate sets of observations, and Table 2b gives collection site information by source.

The data in Table 2a give a good indication of how wide the observed range of scale sizes is for gravity waves. In general the observations show that the longer the period of the observed wave, the smaller the horizontal phase velocity and the smaller the vertical wavelength. A small horizontal phase velocity corresponds to a large component of the phase velocity being in the vertical direction, which gives a considerable vertical energy transport. Similarly, a high horizontal phase velocity is indicative of small vertical energy transport, because of the small component of phase velocity in the vertical direction. Velocity perturbations due to gravity waves in general are 1 to 30 m/s with the largest perturbations corresponding to the waves with the highest phase velocities (shortest periods). The longer period waves result in smaller velocity perturbations.

Westward propagating waves will be most evident during late fall, winter, and early spring when the mean zonal winds are from the west. Based on theory, these waves should have relatively low phase velocities (<30 m/s), whereas the eastward propagating waves will be fewer, but have higher phase velocities (>40 m/s) [*Meek et al.*, 1985]. During the summer months, when the mean zonal winds are from the east, westward propagating waves are not easily observed, and those which are observed are generally traveling to the east, into the wind.

2.4.2 Atmospheric Tides

Tides are the most complex of the wave phenomena because they vary so greatly with latitude, longitude, height, and local time, which is evidenced by the fact that there are still great differences between theory and observation.

TABLE 2a. Gravity Wave Results

Source	Horizontal Wavelength	Vertical Wavelength	Period	Horizontal Phase Velocity	Vertical Velocity	Comments
A	70 km			70 m/s		
B	68 km 119 km	30 km 6 km	10 min 100 min	93 m/s 20 m/s	1 -2 m/s	westward propagation dominant in winter
"		3-40 km avg 10-12 km		10-100 m/s		propagation angles 83° - 95°
C	360 km		2-8 hours	25 m/s		propagation S-SE, wind vector rotates clockwise with height
D	1100 km	3-15 km avg 9.5 km	8-11 hours avg 8.6	35.3 m/s	Phase: -.31 m/s Group: .28 m/s	
E				200 m/s		
F	26 km	14.5 km	11.4 min	38 m/s		phase propagation angle 61°, OH emission data
G	70-2000 km	2-11.5 km	100-1000 min		0.8-.10 m/s	measurements well below the mesopause region

TABLE 2b. Observation Parameters for Gravity Waves

Source	Observers	Location	Instrument	Height Range
A	Vincent and Reid, 1983		HF Doppler Radar	80-94 km
B	Meek et al., 1985	52° N, 107° W Saskatoon, Canada	Dual Bistatic MF Radar	68-119 km
C	Yamamoto et al., 1986	35° N, 136° E Shigaraki, Japan	MU Radar	90-100 km
D	Tsuda et al., 1990	35° N, 136° E Shigaraki, Japan	MU Radar	60-90 km
E	Rees et al., 1990	42° N, 111.4° W Bear Lake Observatory	Fabry Perot Interferometer	86 km
F	Taylor et al., 1987	46° N, 7.8° E Gornergrat, Switzerland	Camera, Photography	80-100 km
G	Gardner et al., 1988	40° N, 88° W Urbana, IL	LIDAR	60 km

Tides are generally defined as oscillations with well-defined basic periods of one day and an infinite number of harmonics. If the period is based on the solar period, solar tides result, and if the period is based on the lunar period, lunar tides result. These oscillations are directly tied to the subsolar and sublunar points and thus have an apparent westward migration, which follows the motion of the sun and the moon. Because the atmosphere acts as a resonant wave guide and has a finite depth, only particular harmonics appear. The atmosphere amplifies the harmonics that match its own resonance, and suppresses others, which will be discussed further.

2.4.2.1 Production of Tidal Waves

Atmospheric tides are excited directly or indirectly by solar thermal and lunar gravitational forcing. Annual and semiannual variations of the weather that we experience on the earth due to the seasonal variation of solar thermal radiation will therefore also affect atmospheric tidal waves. The longest significant period associated with atmospheric tides is one year, however tidal variations can be associated with even longer periods related to the solar cycle, and such things as the global long-term rainfall rates in the tropics [Kato, 1980]. Because tides respond to seasonal changes in solar radiation, they show strong seasonal and annual variation.

The daily cycle of heating and cooling in the atmosphere below the thermosphere is controlled mostly by the absorption of solar radiation by water vapor and ozone, which would produce a single tide with a period of 24 hours. The possibility of tidal periods less than 24 hours comes about because the daily heating cycle is more a square wave than a purely sinusoidal wave and is therefore rich in harmonics. For gravitational tides, the principal period is semidiurnal due primarily to the pull of the moon just as it is for oceanic tides. The gravitational forcing of the moon is large compared to that of the sun, but both are small in contrast to diurnal thermal forcing, so this discussion is limited to thermally driven tides.

2.4.2.2 Tide Fundamentals

A main characteristic of tides is that they have well-defined periods. This fundamental property differentiates them from gravity waves. The higher tidal harmonics (shorter period waves) have the same general periods as gravity waves. This makes it necessary to observe several cycles of a wave to determine whether it is regular and tidal, or just a gravity wave that happens to have a usual tidal period.

The diurnal tide has a wavelength of one global circumference and is assigned a zonal wave number, $s=1$. The semidiurnal and terdiurnal tides correspond to $s=2$ and $s=3$, respectively. The period of the diurnal tide will be 24 hours. The others can be calculated by simply dividing 24 by the corresponding zonal wave number.

For any given pair of s and ω which describe the zonal structure, there are an infinite number of mathematically possible meridional wave structures. These will be specified by the meridional wave number, n . A negative meridional wave number indicates a nonpropagating (trapped) tidal mode and only occurs for diurnal tides with frequencies less than the local Coriolis frequency. A complete set of s , ω , and n completely determines a wave structure and is called a "mode." Some modes are symmetric about the equator and others are not. The diurnal (1,1) and (1,-2) modes are symmetric, while the (1,2) and (1,-1) modes are not. The same is true for the semidiurnal tidal modes.

The one dimension not discussed yet is the depth of the layer of atmospheric fluid, h , in which a particular mode exists. In wave theory this is called the equivalent depth and each single wave mode has a specific equivalent depth. This equivalent depth is an indication of the vertical structure of the wave. We will see that with an assumed solution of the form $e^{i(\omega t + s\phi)}$ (where ϕ is longitude) each specified ω and s gives an infinite number of north-south modes each of which has its own vertical structure. This implies that if the vertical structure (vertical wavelength) of a tide can be measured, the mode being observed can also be determined.

2.4.2.3 Simplifying Assumptions and Equations of Motion

Tides are global in dimension and may be treated similar to gravity waves with a few more restrictions. For tides, the inertial terms will be comparable to the Coriolis term so there is not a simple geostrophic balance. Vertical accelerations can be considered small because tides produce primarily horizontal motions and thus the motion is approximately hydrostatic. Viscous and drag forces are again ignored and the mean winds are assumed to be zero. This approximation is not valid for tides in the ionosphere, or in the lower troposphere where large drag forces affect the motion, but should be reasonable at 87 km. The classical theory also assumes the absence of a meridional temperature gradient.

The basic equation describing tidal motion is Laplace's tidal equation, which is separable in terms of height and latitude dependence. Laplace's tidal equation is given by Equation 2.7.

$$F[\theta_n] + \frac{4a^2\Omega^2}{gh_n}\theta_n = 0 \quad (2.7)$$

Laplace's tidal equation is a differential equation which describes motion in a medium of depth h . The result of this equation is a set of eigenfunctions called Hough functions (θ_n) where the eigenvalue solutions are the equivalent depths, h_n . This equation has an infinite number of solutions, each of which corresponds to a specific tidal mode and a specific equivalent depth.

The equivalent depth, h_n , contains all of the information about geometry and rotation for a tidal mode, and provides the link between the horizontal and vertical structure of the mode. The equivalent depth indicates the allowed divergence of the horizontal wind in a layer of thickness h_n . Thus it relates horizontal wind motions to the vertical response. As the meridional wave number (n) increases, the equivalent depth decreases, indicating that the higher harmonics will be shallower in vertical extent. A reasonable way to think of this is to consider two bodies of water, one deep and the other

very shallow. If the water is shallow, waves necessarily have small vertical extent, and therefore are weak and quickly damped by the medium before much propagation or energy transport can occur. A deep body of water can support waves with large vertical extent and lots of energy can be conveyed. So the equivalent depth basically indicates how deep the medium appears for a given wave mode.

When h is negative (which occurs for waves with long periods), no vertical energy transport is possible because the waves will have no phase variation with height (infinite vertical wavelength) and the wave cannot propagate vertically. Physically a negative h means that at long periods ($\omega < f$) geostrophic balances are established faster than the oscillatory cross-isobaric response and wave motions cannot be set up and sustained [Lindzen, 1990]. The diurnal (1,-2) mode is in this category. Equivalent depths are typically a few kilometers.

2.4.2.4 Vertical Structure

The equation for the vertical structure of a tidal mode is given in terms of the vertical wave number m as

$$m^2 \equiv \frac{1}{Hh_n} \left(\frac{1}{H} \frac{dH}{dz} + k \right) - \frac{1}{4H^2} \quad (2.8)$$

If an approximately isothermal atmosphere is assumed, this can be simplified to

$$m^2 = \frac{k}{Hh_n} - \frac{1}{4H^2} \quad (2.9)$$

The solutions to the tidal equation will have the form

$$\Psi^{\omega,s} = \sum_n \Theta_n^{\omega,s}(\theta) \exp^{i(\omega t + s\phi - n\alpha)} \exp^{z/2H} \quad (2.10)$$

which shows that the actual solution will be a summation over the various modes (n) for a given ω and s .

2.4.2.5 Dispersion Relation

A complete form of the dispersion relation for tides is given by Hooke [1977] as

$$\left[\frac{1}{\sin \theta} \frac{\partial}{\partial \theta} \left(\frac{\sin \theta}{f^2 - \cos^2 \theta} \right) - \frac{1}{f^2 - \cos^2 \theta} \left(\frac{s}{f} \frac{f^2 + \cos^2 \theta}{f^2 - \cos^2 \theta} + \frac{s^2}{\sin^2 \theta} \right) \right] \Theta_s = \frac{4a^2 \Omega_E^2}{gh_s} \Theta_s \quad (2.11)$$

where f is the Coriolis parameter, and the vertical wave number is given by

$$m = \pm \left[\frac{N^2}{gh_s} - \frac{1}{4H^2} \right]^{1/2} \quad (2.12)$$

The vertical wavelength can be found by: $\lambda_z = 2\pi/m$ or

$$\lambda_z = 2\pi \left[\frac{N^2}{gh_s} - \frac{1}{4H^2} \right]^{-1/2} \quad (2.13)$$

To solve for a particular mode, select s and ω and find h from Laplace's equation. Then using h in the vertical structure equation, solve for m . This allows the vertical wavelength to be calculated which determines the mode.

The vertical wave number can also be complex for tides just as it could for gravity waves. For the semidiurnal (2,2) mode, m can become imaginary at the temperature decline near the mesopause if dH/dh becomes sufficiently negative. This means that the equivalent depth will also be negative, and implies reflection of the wave.

Again, tidal theory is only a crude approximation to observations because tides are not adequately understood at this time.

2.4.2.6 Propagation Characteristics

Forcing occurs in layers of the atmosphere, some of which are away from the surface (such as the ozone layer). This means that forcing can be in all directions and tidal propagation is three dimensional.

For the diurnal tide, you will see a phase quadrature where the winds will change quadrants every six hours in a clockwise direction beginning with winds from the east at sunrise. For the semidiurnal tide the winds will complete 2 cycles of wind rotation

during 24 hours instead of the one, and every 3 hours the winds are expected to change quadrants.

Figure 4 from Lindzen [1990] shows the diurnal tidal modes and helps to explain why negative equivalent depths and trapped tidal modes occur only away from the equator, and only for the diurnal tide.

Notice that some modes are confined mostly to a region within $\pm 30^\circ$ latitude and others exist mainly away from that region. We know that equivalent depth is latitude dependent as:

$$gh_n = \frac{\omega^2 - f^2}{k^2 + l_n^2} \quad (2.14)$$

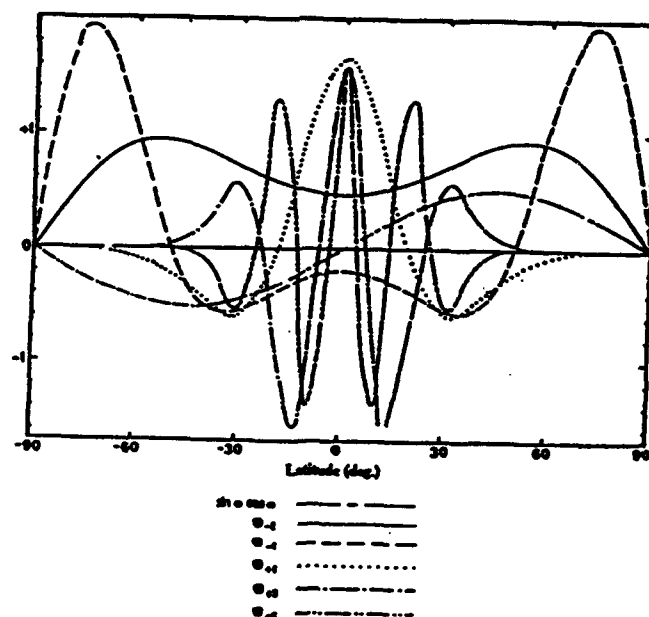


Fig. 4. Symmetric Hough functions for the migrating solar diurnal thermal tide. Also shown is $\sin \theta \cos \theta$, the most important odd mode [After Lindzen, 1971].

Vertical propagation requires h_n to be positive, which in turn requires $f^2 < \omega^2 < N^2$. When $\omega < f$, negative equivalent depths associated with nonpropagating (evanescent) waves appear.

To find where h_n becomes zero, which will determine where the transition from positive to negative equivalent depths occurs, we set $\omega = f$. For the diurnal modes, ω also equals Ω , so that $f = \Omega$, and we find that this occurs when $\sin\theta = 1/2$ or when $\theta = 30^\circ$. Because ω is a constant, and Coriolis increases poleward, negative equivalent depths and hence nonpropagating modes must be excited primarily at latitudes higher than 30° . A propagating diurnal tide would be confined to within approximately 30° of the equator. Thus, internal waves are not well excited when their frequency is less than the Coriolis frequency, which occurs above 30° latitude [Lindzen, 1990]. As a result, the diurnal tide tends to be smaller than the semidiurnal tide at higher latitudes. Since semidiurnal tidal frequencies are always greater than the Coriolis frequency, only propagating modes occur. For these reasons I would expect the semidiurnal tide to be dominate at $42^\circ N$ latitude.

Which modes are salient at a particular point in the earth's atmosphere depends on several other factors. Although an infinite number of modes are possible, only a few of the lowest order are important. The first factor is the meridional structure of the mode itself. Given that solar input is greatest near the equator you would expect modes which are symmetric about the equator to be preferentially excited by thermal forcing than modes that are antisymmetric. This should be so because the forcing mechanism acts at the apex of the symmetric mode, while the antisymmetric modes have a node at the equator which doesn't allow it to be excited as readily. This conceptually would indicate that during solstice periods when the forcing moves away from the equator, the antisymmetric and higher harmonic modes might be excited more readily.

The other factor that determines what can be seen depends on altitude. The diurnal tide is dominant at all altitudes equatorward of 30° latitude for reasons related to the frequency of the wave as discussed earlier, but also because the depth of the atmosphere over which most of the heating occurs must be considered. Tide generation occurs in finite layers of the atmosphere. If the vertical wavelength of a mode is comparable to or smaller than the depth of forcing, the wave will suffer self-interference and as a result will be weak. In Figure 5, the vertical wavelength drops off quickly after the first few harmonics and thus one would expect only the first few to be significant. At the equator a large layer of the atmosphere is thermally excited, and the diurnal (1,-2) mode has a large equivalent depth which allows it to be more efficiently excited than other modes. Very shallow waves are destroyed quickly away from source regions.

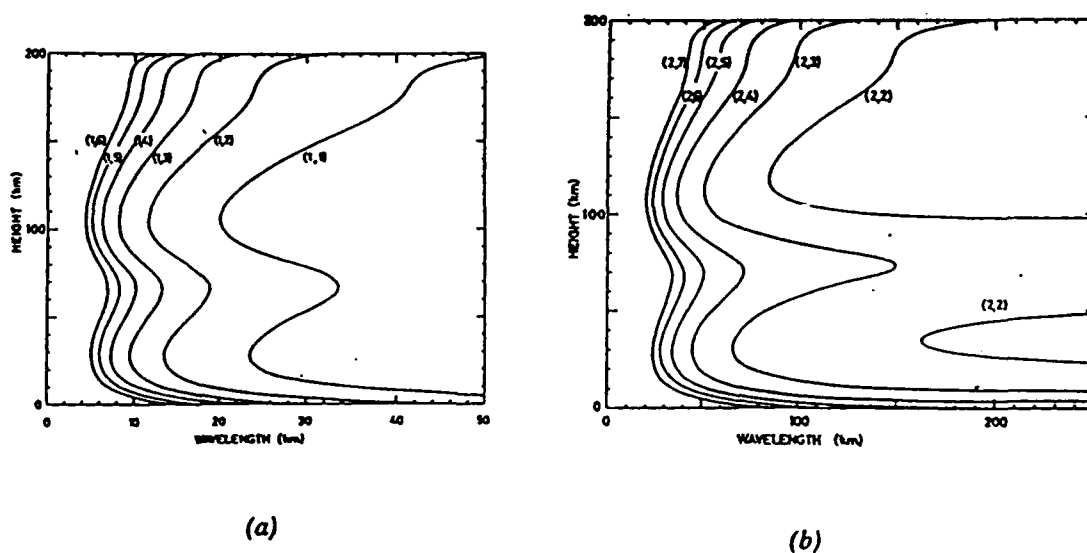


Fig. 5. Vertical wavelength of each tidal mode (s,n). (a) diurnal, (b) semidiurnal [Kato, 1980]. Reprinted by permission of Kluwer Academic Publishers.

In the mid-latitude stratosphere and mesosphere, the propagating diurnal tide has small vertical wavelengths and therefore will not be dominant. In these regions the semidiurnal solar tide dominates up to about 110 km. Above this, the diurnal tide is again dominant and drives the ionospheric tidal dynamo.

In the lower atmosphere there are two main regions of radiation absorption. Water vapor absorption is dominant in the region below 20 km and ozone absorbs a large amount of radiation in the region between 20 and 60 km. Overall, ozone supplies the most total energy. *Forbes* [1982] further breaks down the energy absorption by mode for both the diurnal and semidiurnal tides.

Figure 6a shows clearly how most of the energy goes into the non-propagating diurnal (1,-2) mode. Notice the presence of additional harmonics during the solstice period that are not visible during equinox. The same is true for the semidiurnal tides in Figure 6b where antisymmetric modes appear during the solstice that are not present at equinox. Notice also for the semidiurnal tide the dominance during all seasons of the (2,2) mode. This mode is dominant primarily because of its comparatively large vertical wavelength and also because its equivalent depth matches that of the free oscillations in the atmosphere as was mentioned earlier.

A third consideration has to do with the atmosphere itself. The atmosphere has a natural frequency of oscillation based on its depth, called the resonant frequency, which corresponds to a period of $12/\sin\theta$ hours. Since this resonant frequency varies with latitude, we would expect to find different tidal components amplified at different latitudes. Above 30° this is the semidiurnal tide, and below 30° it is the diurnal tide.

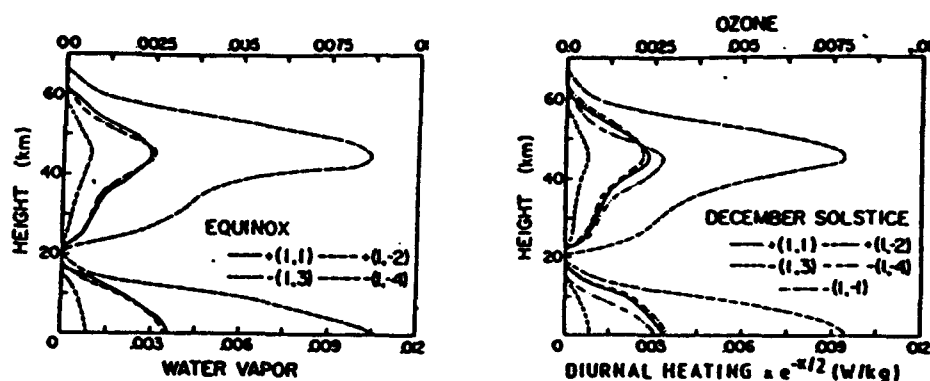


Fig. 6a. Hough decomposition of diurnal heating rates vs. height during equinox (left) and December solstice (right) due to insolation absorption by H_2O (lower scales) and O_3 (upper scales) in units of W/kg multiplied by $\exp(-x/2)$, where $x = \ln(p/p_0)$ [Forbes, 1982].

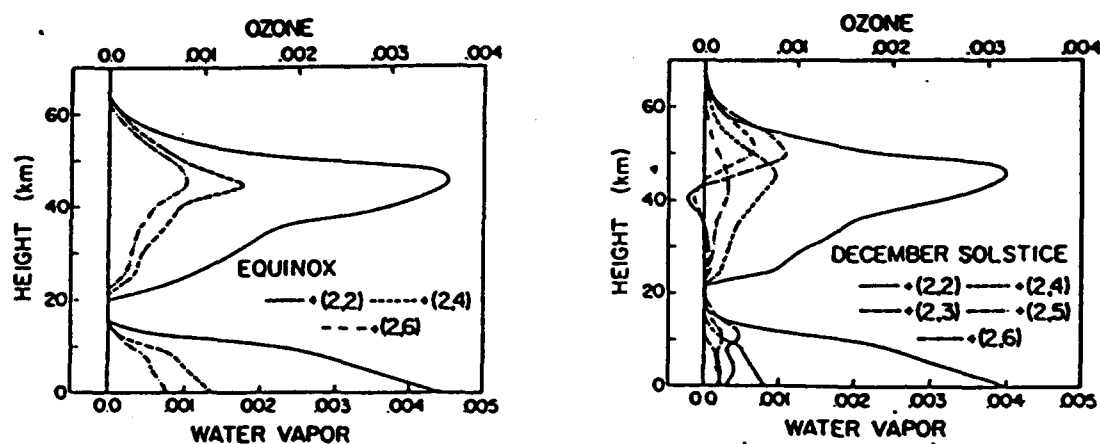


Fig. 6b. Hough decomposition of semidiurnal heating rates vs. height. Otherwise as in figure 6a [Forbes, 1982].

2.4.2.7 Previous Results

The modes which are prominent between 80 and 110 km in the mid-latitudes are

Diurnal: (1,1), (1,-2), and (1,-1)

Semidiurnal (2,2), (2,3) (2,4), and (2,6)

with the semidiurnal (2,4) mode most likely to be dominant at the mesopause.

Table 3 gives the basic calculated characteristics for each mode at 42°N latitude.

TABLE 3. Diurnal and Semidiurnal Tidal Mode Parameters

Tide	Zonal Wavelength	Mode (s,n)	Equivalent Depth, h (km)	Vertical Wavelength (85 km)
Diurnal	~40,000 km	1,1	0.69	26 km
		1,-2	-12.27	∞
Semidiurnal	~20,000 km	2,2	7.85	>100 km
		2,3	3.67	100 km
		2,4	2.11	50 km
		2,6	0.96	30 km

The first thing that is obvious in looking at this table is how quickly the equivalent depth drops off with increasing n. This shows how only a few of the lowest order modes are important, the rest being too shallow, and too quickly attenuated by the atmosphere to contribute significantly.

The vertical velocity increases with height as $\rho^{-1/2}$ to a maximum value of about 20 cm/s at about 90 km. Larger values lead to instability of the tide which occurs at about 110 km [Volland, 1988].

2.4.2.7.1 Characteristics of Tides at the Mid-latitude Mesopause

Teitelbaum et al. [1989] observed typical horizontal winds of 10's of m/s at the mesopause. They also observed that the tides showed a downward phase progression and hence, upward energy transport, which is consistent with theory. In Tables 4 and 5 one can see that the predicted winds of 10-20 m/s are reasonable, and that the dominance of the semidiurnal tide over the diurnal tide also seems to be correct. The results in Tables 4 and 5 are very sensitive to the presence of higher harmonics as evidenced by the high normalization constants for the higher harmonics.

Teitelbaum et al. [1989] (Wallops Island (38°N)) measured typical vertical wavelengths that were about 20 km. He observed the growth of the tidal component with height up to 105 km and the subsequent decay at higher altitudes. *Lindzen* [1990] predicted a diurnal tide with typical vertical wavelengths of 25 km, which is close to earlier research.

Figure 7 [*Richmond et al.*, 1976] shows that the dominant tidal mode at 85 km will be the semidiurnal (2,4) mode. Wind amplitudes are in good agreement with theoretical predictions with about 10 m/s at 86 km. The prediction for the time of local maximum is at 0230 UT.

Although the diurnal tide is not going to be the major component of the tides at 42°N , it should still be observable. The presence of both should be observable over Bear Lake.

2.4.2.8 Results of Current Research

The tidal results section is divided into the diurnal, semidiurnal, and terdiurnal components since these appear to be the primary players for current tidal research. The behavior of the tides is shown to be made up of primarily two characteristic states which dominate the summer and winter solstice periods, and transitional periods between these states, corresponding to equinox periods.

TABLE 4. Semidiurnal Tidal Wind Components at 42° Latitude

Mode	2,2	2,4	2,6	Totals
Northerly Wind Component	0.95	0.75	0.05	
Normalization Factor	3	9	16	
Total Contribution (m/s)	2.85	6.75	0.8	10.4 m/s northerly
Westerly Wind Component	0.9	0.75	0.2	
Normalization Factor	3	9	16	
Total Contribution (m/s)	2.7	6.75	3.2	12.65 m/s westerly

TABLE 5. Diurnal Tidal Wind Components at 42° Latitude

Mode	1,-2	1,-4	1,1	1,3	1,5	Totals
Northerly Wind Component	-0.45	0.3	0.28	-0.13	.03	
Normalization Factor	10	40	40	100	200	
Total Contribution (m/s)	-4.5	12	11.2	-13	6	11.7 m/s northerly
Westerly Wind Component	-0.2	0.38	0.41	-0.16	0.05	
Normalization Factor	10	40	30	100	150	
Total Contribution (m/s)	-2	15.2	12.3	-16	7.5	17 m/s westerly

I have included in this summary only the seasonal averages for the solstice periods which each seemed to have a distinct character, rather than doing a monthly breakdown because there was so much variability in the published data that only broad conclusions are reasonable. Information about each source is listed in Table 7.

2.4.2.8.1 The Diurnal Tide

Overall, the diurnal tide shows some seasonal variation. Maximum amplitudes and infinite vertical wavelengths, showing a strong dominance of the trapped modes, were characteristic of the summer months and/or equinox periods. Winter solstice periods were generally characterized by weaker amplitudes and shorter vertical wavelengths which implies the presence of higher harmonics and a dominance of the propagating modes.

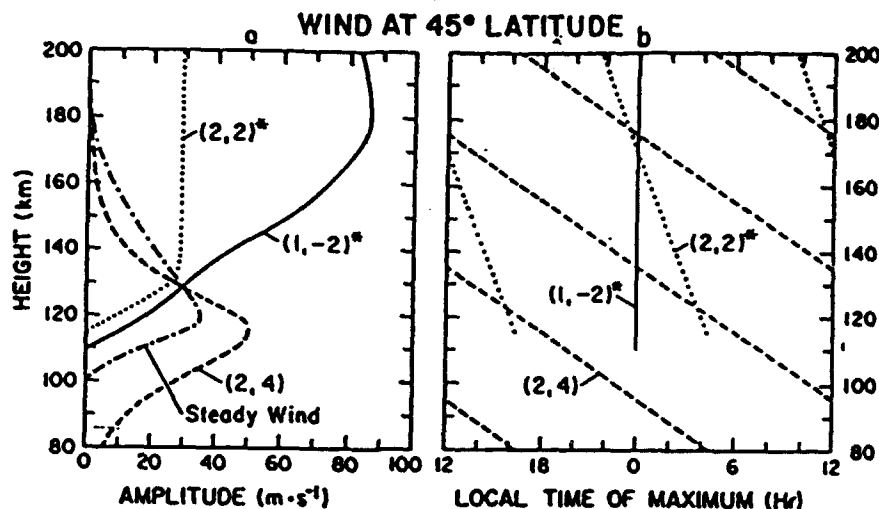


Fig. 7. (a) Amplitudes of the southward components (or eastward component for the steady wind) at 45° latitude from Richmond's research. (b) Phases of southward components at 45° latitude [Richmond et al., 1976].

In trying to summarize the information on diurnal tides in Table 6a, I refer back to Figure 5. (Observation parameters, etc. are given in Table 7.) The comparison shows that the vertical wavelengths of about 20 km correspond to the diurnal (1,2) mode, and wavelengths of 30-40 km correspond to the diurnal (1,1) mode, which are both propagating modes. These then appear to be the dominant modes of the winter mesopause region at mid-latitudes, [Vincent et al., 1989]. During the summer and equinox periods, observations of longer wavelengths (>100 km) and evanescent waves with infinite vertical wavelengths characterize the diurnal tide, and this indicates the dominance of the (1,-2) mode.

TABLE 6a: Diurnal Tide Results

Source	Season	Average Amplitude	Vertical Wavelength	Season	Average Amplitude	Vertical Wavelength
A			20 km			
B	Winter	5-10 m/s	35 km irregular	Summer	10-15 m/s	N-S ∞ E-W irreg
C	Winter	5 m/s	30 km	Summer	5 m/s	35 km irregular
D	Winter	<15 m/s	20-60 km	Summer	<20 m/s	40->100 km
E	Winter	10 m/s	20-30 km irregular	Summer	10 m/s	25- ∞ irregular
F	Winter	10-15 m/s	20- ∞ irregular	Summer	5-10 m/s	100- ∞ irregular
G	Winter	5 m/s	50-100 km	Summer	10 m/s	∞ irregular
H	Average	5-10 m/s				
I	Winter	10 m/s zonal 10 m/s merid	30 km	Summer	35 m/s zonal 32 m/s merid	∞
N	Winter	25 m/s zonal	30-40 km	Summer	15 m/s zonal	∞
O [♥]	Winter	5 m/s	∞	Summer	11 m/s zonal	∞
P	Winter			Summer	12 m/s zonal 7 m/s merid	100 km

♥ At Kyoto, the only time that the waves were not evanescent was during equinox and when vertical wavelengths of ~40 km were seen.

Manson et al. [1989] observed that the tides were all circular below 90 km, which indicates propagating modes only, but *Kazimirovsky and Zhovty* [1989] examined how the tides in the mid-latitudes are complicated by the interference between the propagating and evanescent modes, with the evanescent mode becoming dominant in the summer, and the propagating modes prevalent in the winter. This seems more in line with actual observations and indicates the complexity of tides in the mid-latitudes. Their research also indicated that the diurnal tide was always increasing in amplitude with height between 80 and 100 km, which implies that breaking occurred somewhere above 100 km and that dissipation was not dominant at the mesopause.

Phase transitions occurred in general near the time of seasonal mesospheric wind reversal for all observation points with the spring transition occurring from late March to early May, and the autumn transition in September or October.

2.4.2.8.2 The Semidiurnal Tide

A comparison of the data in Table 6b again to Figure 5 from *Kato* [1980] shows the presence of all the following modes by vertical wavelength:

100-∞ km→(2,2),

100 km→(2,3),

60 km→(2,4),

40-50 km→(2,5)

30 km→(2,6).

The semidiurnal tide shows a larger seasonal variation than the diurnal tide. In general, amplitudes are much larger in the winter than in the summer with some exceptions where the actual maximums occur at equinox. Winter periods exhibit shorter vertical wavelengths, which indicate the presence of harmonics out to the (2,6), which corresponds to the smallest observed vertical wavelength of 30 km. Summer is characterized by large vertical wavelengths and fairly constant amplitudes, indicating the dominance of the (2,2) mode. This is opposite from the diurnal tides in which maximum amplitudes tended to correspond to the larger vertical wavelengths.

Local time of maximum amplitude also changed seasonally, with maximum reached 4-6 hours earlier in the winter than the summer [*Vincent et al.*, 1989]. This result may help explain the difference in observed time of maximum at Bear Lake from *Rees et al.* [1980], and the predicted time of maximum from *Richmond et al.* [1976] which differed by 8.5 hours. This might be attributed to these seasonal variations and the onset of the fall wind reversal at Bear Lake.

TABLE 6b. Semidiurnal Tide Results

Source	Season	Average Amplitude	Vertical Wavelength	Season	Average Amplitude	Vertical Wavelength
A	Fall	40 m/s	>30 km			
B	Winter	35 m/s max	30-40 km	Summer	10 m/s min	200-∞ km
C	Winter	30 m/s max	60 km	Summer	10 m/s min	>100-∞ km
D	Winter	20 m/s	50->100 km	Summer	20 m/s	100-∞ km
E	Winter	30 m/s max	40-60 km	Summer	10 m/s min	250-∞ km
F	Winter	20 m/s max	65-200 km	Summer	10 m/s min	150-∞ km
L	Winter	10 m/s max	70-100 km	Summer	5 m/s min	>>100 km
M	Winter	35 m/s max	45 km	Summer	5 m/s min	∞ km-June 50 km-Jul/Aug
I	Winter	15 m/s zonal 12 m/s merid		Summer	35 m/s zonal 32 m/s merid	
H		20 m/s				
N	Winter	10-15 m/s	50-80 km	Summer	5-10 m/s	∞
O [♠]	Winter	3-5 m/s	50-80 km	Summer	5-10 m/s	∞
P*	Winter		80-100 km	Summer	22 m/s zonal 25 m/s merid	80-100 km

♠ Maximum winds occurred during equinox at Kyoto

* Two maximums occurred, corresponding to the equinox periods

Again for the semidiurnal tides, equinox transitions are tied to the seasonal reversal of winds. Phase transitions occurred in the spring between mid-March and late April, and in the fall between September and October. The results from Bear Lake (Source A) indicated a phase variability from night to night of 1-3 hours and wind velocities with magnitudes greater than theory predicts but in line with data from other stations. This may indicate a problem with analysis of the data, or suggest that the mean zonal winds have not effectively been averaged out.

Clark and Salah [1991] found that independent of season, the semidiurnal tide grows in amplitude between 80 and 120 km before damping occurs, which corroborates predicted results.

2.4.2.8.3 The Terdiurnal Tide

For completeness, I have included this brief summary of research done into the effects of the terdiurnal tides near the mid-latitude mesopause.

The terdiurnal (8 hour) tide is generally stronger in the winter than in the summer, with the larger wavelengths corresponding to the maximum amplitudes as it was for the diurnal tides. *Teitelbaum et al.* [1989] showed that the terdiurnal tide amplitude reaches its maximum in the mid-latitudes, and can become comparable to that of the diurnal tide in the winter months. Table 6c summarizes their results.

TABLE 6c. Terdiurnal Tide Results

Source	Season	Average Amplitude	Vertical Wavelength	Season	Average Amplitude	Wavelength
K	Winter	6 m/s	long wavelengths	Summer	3 m/s	shorter wavelengths

Note: Taken from *Teitelbaum et al.* [1989]

This may be an important result. The terdiurnal tide is thought to be generated by the nonlinear interaction of the diurnal and semidiurnal tides as well as being a solar-driven tide. This tide is a permanent feature of the mesosphere and lower thermosphere [*Teitelbaum et al.*, 1989].

2.4.2.8.4 Summary

Overall, wind amplitudes associated with the semidiurnal tide components are up to three times larger than the diurnal components. Both are generally larger than the terdiurnal winds, but *Teitelbaum et al.* [1989] made a good argument for looking for the terdiurnal component of the winds during the winter when it may be comparable to the diurnal winds.

TABLE 7. Observation Parameters

Source	Observers	Location	Instrument	Height Range
A	Rees et al., 1990	42° N, 111° W Bear Lake, Utah	Fabry-Perot Interferometer	86 km
B	Manson et al., 1989	52° N 107° W Saskatoon	MF Radar	60-110 km
C	Manson et al., 1989	44° N 1° E Monpazier	MF Radar	60-110 km
D	Manson et al., 1989	44° S 173° E Christchurch	MF Radar	60-110 km
E	Manson et al., 1989	47° N 3° E Garchy	Meteor Radar	60-110 km
F	Manson et al., 1989	43° N 71° W Durham	Meteor Radar	60-110 km
G	Forbes and Hagen, 1988	50° N general case	Model	60-110 km
H	Bernard, 1974	53° N, 0° W Jodrell Bank	Meteor Trail Method	80-110 km
I	Kazimirovsky and Zhovty, 1989	52° N 102° E Badary, Siberia	LF Radar	85-95 km
K	Teitelbaum et al., 1989	47° N, 3° E Garchy	Radar	80-110 km
L	Manson et al., 1989	52° N, 15° E Collm	Radar	80-100 km
M	Forbes and Vial, 1989	50° N	Model	80-100 km
N	Vincent et al., 1989	35° S, 138° E Adelaide	Partial Reflection Radar	78-98 km
O	Vincent et al., 1989	35° N, 136° E Kyoto	Meteor Wind Radar	82-104 km
P	Clark and Salah, 1991	43° N, 71° W Millstone Hill	Meteor Wind Radar and Incoherent Scatter Radar	80-135 km

2.4.2.8.5 Seasonal Effects

For the mid-latitudes, equinox periods should show the strongest diurnal tidal components since the solar input will be directly over the equator. During solstice periods higher harmonics and antisymmetric modes will appear more readily. It is hard to say how the two solstice periods should differ. Perhaps summer solstice will more closely resemble equinox conditions than winter solstice because of the more massive

input of solar energy and the more stable thermal structure of the atmosphere during the summer, but that may be a crude generalization.

Major tidal modes at the mesopause have been examined, and the dominance (particularly in the winter) of the semidiurnal (2,4) mode has been shown. The presence of the diurnal tide noted to be weaker than the semidiurnal tide, and is confined to the summer hemisphere. Average amplitudes of the diurnal, semidiurnal, and terdiurnal tides were found to be 5-15 m/s, 10-40 m/s, and 3-6 m/s, respectively.

2.4.3 Planetary Waves

Planetary waves can be seen as large-scale asymmetries in the middle atmosphere circulation resulting from the sphericity and rotation of the earth, or, more generally, from the northward potential vorticity gradient [Andrews *et al.*, 1987]. These waves conserve absolute vorticity which acts as the restoring force, and they exist due to the variation of the Coriolis force with latitude. These waves differ from gravity waves and tides in that the restoring force is not gravity and because they exist primarily as a perturbation in the horizontal rather than in the vertical so that the requirement that $\omega > f$ for vertical propagation does not apply.

Planetary waves are a major source of momentum and heat transfer at middle atmospheric heights [Holton, 1979]. Because their speeds are generally comparable to the mean zonal wind speed, and breaking occurs when speeds are comparable, a lot of planetary wave energy is continually given up to the mean flow. Planetary waves are almost entirely trapped in the lower atmosphere by the strong mesospheric winds. They are primarily a sinusoidal wave in the horizontal plane traveling zonally with a meridional displacement.

The effects of planetary waves are most easily seen by the strong cooling and heating rates they produce, but are also evident as long-period wind fluctuations (for the patient scientist!). Long-term averaging of the winds obtained using the Fabry-Perot

may yield evidence of planetary waves; however, observation of temperature variations at 86 km will probably give the strongest, most immediate evidence. Heating and cooling by planetary waves is so significant that the phenomenon of major stratospheric warming during winter periods in the northern hemisphere and the corresponding mesospheric cooling is thought to be due to planetary wave motion and is the focus of current research [*Hauchcorne and Chanin, 1982*].

2.4.3.1 Forced vs. Unforced Planetary Waves

There are two types of planetary waves, free and forced, classified by how they are produced. Only the forced waves are of interest to this study for the following reasons. Free traveling planetary waves correspond to resonant normal modes of the atmosphere and are excited by weak, random forcing. These waves have no continuous forcing mechanism, no phase tilt with height, and they decay exponentially with altitude. Therefore, they have no means of propagating to great heights [*Andrews et al., 1987*]. Also, because free waves tend to be generated towards the high frequency end of the planetary wave spectrum, they are more likely to be filtered out by the mesospheric winds, which will be discussed further in the following sections. For these reasons, free oscillations are thought to be unimportant to the dynamics of the upper and middle atmosphere.

Forced oscillations, on the other hand, are responses to energy sources of specific frequency and spatial distribution, generally tending toward the longer wavelengths. These waves are known to propagate to great heights without being destroyed by the mesospheric winds [*Holton, 1979*]. Figure 8 shows planetary waves in the stratosphere of the northern hemisphere [*Holton, 1979*].

2.4.3.2 Production of Planetary Waves

All planetary waves observed in the stratosphere and mesosphere appear to propagate upward from forcing regions in the troposphere [*Holton, 1979*]. In general,

the major source mechanisms for forced planetary waves are related to instabilities and irregular thermal or mechanical forcing, although results of research in this area are limited [Andrews *et al.*, 1987]. The size of the wave observed from each of these mechanisms differs. Instabilities such as barotropic or baroclinic instabilities result in waves with fairly short wavelengths of several thousand kilometers, whereas topographical forcing and large-scale differential heating result in wavelengths on the order of one half the global circumference at 45° latitude, or about 20,000 km [Hooke, 1977].

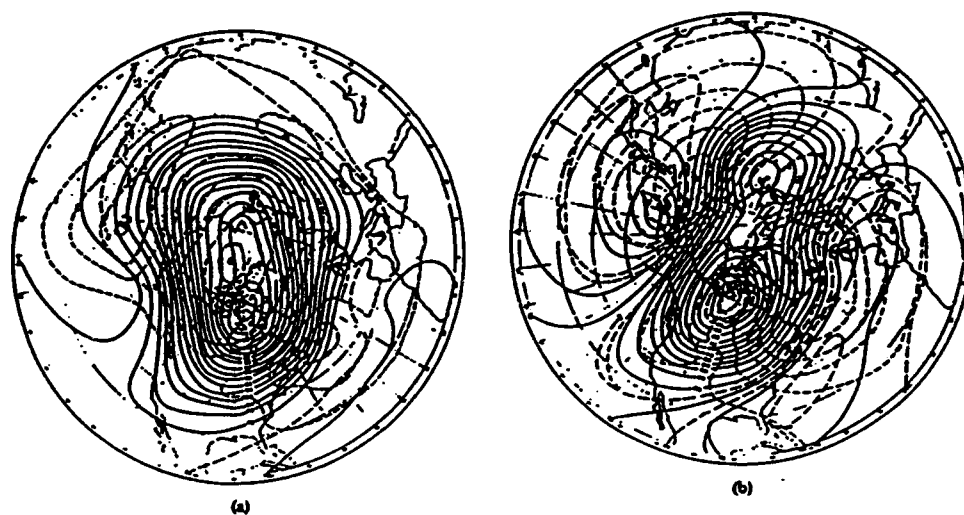


Fig. 8. 50-mb height field (solid contours in 100's of feet) and temperature field (dashed contours in $^\circ\text{C}$) in (a) January and (b) February [Holton, 1979].

2.4.3.3 Simplifying Assumptions and Equations of Motion

Planetary waves have very long periods, exceeding the period of the earth's rotation and, therefore, one wavelength might take several days to pass a point. Because

of this, planetary waves are affected by the curvature and rotation of the earth, making the Coriolis force a significant factor. For this reason the inertial term in the equation of motion will tend to be small compared to the Coriolis term, and thus the horizontal flow is an approximate geostrophic balance between the Coriolis force and the pressure gradient force. At the same time, vertical accelerations are small in the sense that there is nearly a complete balance between the vertical pressure gradient and the gravity term. This means that the wind components will be almost entirely horizontal, and the motion can be approximated as hydrostatic. To simplify this development, the mean horizontal wind (u) will be considered constant (but non-zero), as well as the buoyancy frequency, N . The following is presented by *Holton* [1979].

2.4.3.4 Dispersion Relation for Planetary Waves

The dispersion relation for planetary waves is

$$\omega = ck = ku - \beta k \left[k^2 + l^2 + \frac{f_o^2}{N^2} (m^2 + 1) \right]^{-1/2}$$

The $e^{(z/2H)}$ term is included to simplify the equation for the vertical dependence.

The solution for the vertical dependence Ψ must satisfy

$$\frac{d^2 \Psi^2}{dz^2} + m^2 \Psi = 0 \quad (2.15)$$

where
$$m^2 = \frac{N^2}{f_o^2} \left[\frac{\beta}{\bar{u} - c} - (k^2 + l^2) \right] - \frac{1}{4H^2}$$

and k and l are the zonal and meridional wave numbers, respectively, and f is the Coriolis parameter and includes the latitudinal dependence of the equation.

Solutions to this equation will have the form $\Psi(z) = Ae^{imz}$, where A is a constant amplitude. This equation gives the vertical propagation characteristics. Notice that this is the same vertical structure equation as for tides except we substitute for gh

$$gh = \frac{f_e^2}{\frac{\beta}{\bar{u} - c} - (k^2 + l^2)} \quad (2.16)$$

Vertical propagation requires that $m^2 > 0$. For forced stationary waves, $c=0$ and vertically propagating modes occur only when the following condition is met

$$0 < \bar{u} < \beta \left[(k^2 + l^2) + \frac{f_0^2}{(4N^2 H^2)} \right]^{-1} \equiv U_c. \quad (2.17)$$

U_c is called the Rossby critical velocity. This is an interesting result because vertical propagation requires a background wind with a value greater than zero but less than some critical velocity, which is determined only by the horizontal scale of the stationary wave. The direction of the mean wind also has to be positive (from the west) for vertical propagation to occur. At 85 km, the mean winds are predominately from the west; however, the region does experience a seasonal wind reversal. During the months where the mean winds are from the east, planetary waves which are generated will not propagate upwards ($m^2 < 0$).

In the winter hemisphere mesopause the winds are westerly (from the west) and weak which should allow planetary wave propagation. However, since the waves are propagating upward from the troposphere, they have to pass through the strong band of mesospheric westerlies at about 65 km. This should effectively filter out all but the very longest wavelengths. From this a general theory can be formulated that the only planetary waves that might be visible at the mesopause will have extremely long wavelengths and occur during the winter. This is in broad agreement with observations which show that stationary waves tend to be composed only of the ultralong ($s=1,2,3$) modes in the winter westerlies.

Figure 9 shows mean zonal wind velocity vs. wavelength for a quasi-stationary wave in the mid-latitudes. To have an internal (vertically propagating) wave the velocity of the mean zonal winds has to be such that it falls below the curve labeled C-D critical.

Salby and Roper [1980] concluded from their research that only during short periods in autumn and spring when the mean winds are weak and westerly should substantial vertical energy propagation occur due to planetary waves.

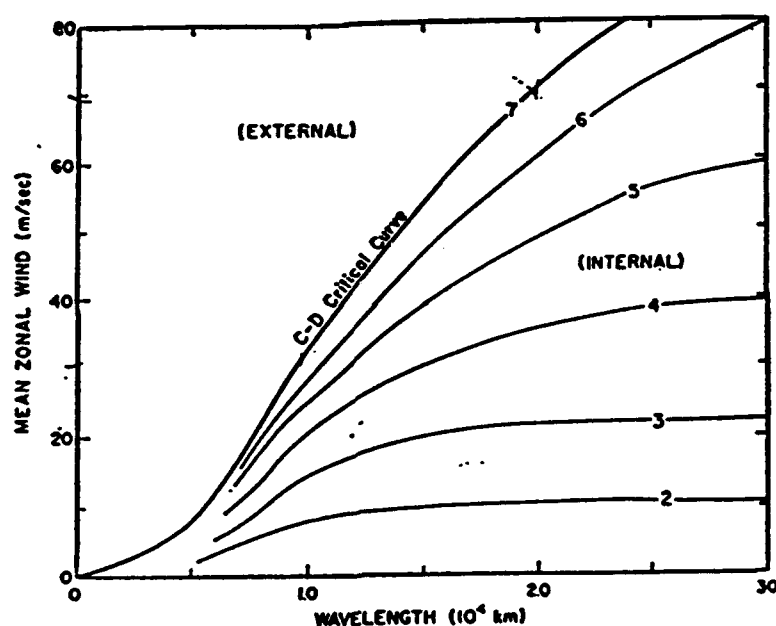


Fig. 9. The amplitude $|\Psi|$ in units of $10^3 \text{ m}^2 \text{ s}^{-1}$ for a stationary planetary wave on the mid-latitude beta-plane as a function of mean zonal wind speed and wavelength, for $f_0 = 10^{-4} \text{ s}^{-1}$, $\beta = 1.6 \times 10^{-11} \text{ m}^{-1} \text{ s}^{-1}$, $H = 7 \times 10^3 \text{ m}$, $N = 0.02 \text{ s}^{-1}$ and $h_t = 1.25 \text{ km}$. [After Hirota, 1971].

Planetary waves are known to be very weak in the summer middle atmosphere [Geller, 1983]. At the mesopause, the chance to observe planetary waves will probably

be limited to August through April due to the limiting seasonal winds, and there may also be a void of activity during the period of maximum mesospheric winds at winter solstice.

2.4.3.5 Characteristics of Planetary Waves at the Mid-latitude Mesopause

Because the atmosphere acts as a wave guide, certain wavelengths appear and are amplified while other wavelengths are damped. In the mid-latitudes, planetary waves are restricted primarily to zonal wave numbers 1 and 2, and the periods which seem to be amplified are associated with 2, 5, 16, 28, and 40 day periods. It is important to recognize that these designations of "5-day wave" or "16-day wave" etc. should not be taken literally. These just give an indication of the approximate frequency spectrum since there is more than just a single mode present at any one time. The various waves interact and give a frequency band centered approximately around these periods.

Results from observations around 50 km for zonal wave number $s=1$ indicate dominant periods of 5 and 16 days. These two westward propagating waves have structures which are similar to the symmetric modes (1,2) and (1,4), respectively. The 5-day wave is generally larger in the summer, while the 16-day is larger in the winter. There is also a 10-day antisymmetric mode which is similar to the (1,3) mode, but it is much weaker than the other two.

For $s=2$, periods near 3-7 days (the 4-day wave) and 10-18 days have been observed. The 4-day wave has a structure similar to (2,3).

Wave oscillation with periods near 2.1 days occur within the mesosphere (a "2-day wave") [Salby and Roper, 1980; Clark and Salah, 1991]. The zonal wave number appears to be $s=3$ and the wave resembles the antisymmetric normal mode (3,3). This is seen mostly at low latitudes and is also a westward-migrating wave.

For the 40-day wave, periods range from 30 to 60 days. It is mostly observed in the tropics with a zonal wave number 1, but was measured at 44°N latitude by Hauchecorne and Chanin [1983]. This wave is unusual because it migrates eastward

with amplitudes of a few m/s. Amplitudes decrease toward the poles, and theoretically it should not be prominent at 42°N latitude.

Planetary waves are observed with very small vertical phase tilt, and the disturbances grow with height through the mesosphere [Volland, 1988]. A westward phase tilt is evident in the stratosphere for all planetary wave modes, which indicates upward energy transport. Horizontal wave speeds are on the order of 10 m/s, comparable to the mean zonal wind and thus planetary waves are sensitive to interaction with the zonal flow [Hooke, 1977].

The parameters for the most commonly observed planetary wave periods are given in Table 8. Note that for large zonal wave number (high harmonics), or long periods, the waves become shallower (smaller equivalent depth), and thus are not prominent. For instance, one would expect the $s=1$, 5-day wave to be much more prominent than the $s=1$, 40-day wave or the $s=3$, 2-day wave. The exact effects of course depend on latitude and altitude, but this gives a general idea.

TABLE 8. Planetary Waves

Zonal Wave Number	Period	Equivalent Depth, h	Vertical Wavelength
$s=1$	5-day	10 km	100- ∞ km
$s=1$	10-day	2 km	50 km
$s=1$	16-day	0.8 km	30 km
$s=1^*$	40-day	0.1-1 km	< 30 km
$s=2^*$	3-7 day	3-10 km	50- ∞ km
$s=2^*$	10-18 day	0.3-0.8 km	15-30 km
$s=3^*$	2-day	100- ∞	∞

* These are estimates

2.5 Airglow vs. Auroral Activity

Auroral activity is due primarily to the influx of charged particles from the magnetosphere. These particles strike neutral particles in the earth's atmosphere, causing a transfer of kinetic energy which ionizes and excites the neutral particles, depending on

the amount of energy acquired by the absorbing particle. There are a variety of processes which lead to the energy loss and emission of light for these excited atoms and molecules, but a full discussion of these processes are beyond the scope of this thesis.

By comparison, the processes which lead to airglow result directly from the photochemistry and chemical processes specific to a particular region of the atmosphere. Solar photons are absorbed in the mesosphere primarily at UV wavelengths ($0.1 - 0.4 \mu\text{m}$) and to a lesser extent at visible ($0.4 - 0.7 \mu\text{m}$) and near infrared ($0.7 - 4 \mu\text{m}$) and x-ray wavelengths [Andrews *et al.*, 1987]. The absorbed energy produces electronic, vibrational, and rotational excitation; molecular dissociation; and ionization. Ionization of OH requires 1027 \AA ($0.1027 \mu\text{m}$).

2.6 Altitude of OH Airglow Emissions

Several intensive studies have been done to pinpoint the emission altitude of the OH Meinel emissions. These include Baker and Stair [1988] who used the composite results from many rocket observations to ascertain the height of the OH Meinel emissions. Their results found this layer to be at $87 \pm 2 \text{ km}$ with a full width at half-intensity of 6 km . This gives the approximate altitude resolution we will have when measuring the 8430 \AA OH emission.

von Zahn *et al.* [1989], comparing OH and sodium (Na) lidar temperatures, determined the emission altitude to be $86 \pm 4 \text{ km}$. The UARS satellite is currently mapping the height of the OH emission layer and should document any seasonal and latitudinal differences; however, research to this point supports the conclusion that the layer is at a nearly constant altitude.

2.7 Mechanisms for OH Airglow

The mesosphere, because it is within the homosphere, tends to remain fairly well mixed due to fluid motions and turbulence. This results in uniform mixing ratios with no

significant stratification of constituents according to their molecular weight. However, many minor constituents such as ozone and hydroxyl develop significant concentrations in particular regions of the atmosphere due to photoionization, chemical production or transport. The altitude of layer formation for the minor constituent is dependent on the processes specific to the region and the constituent.

Several parameters affect the formation of OH*, including the availability of neutral atomic hydrogen, atomic oxygen, and ozone. Their availability, in turn, is affected by the amount of incoming solar radiation and transport mechanisms, which additionally depend on the time of day and the season. Presently, there is no way to fully or accurately predict OH* intensities because all of the parameters important to its formation are not known.

Le Texier et al. [1987] explained the dependence of OH* densities on neutral species densities, noting that the excitation mechanisms may be different for different vibrational bands and roughly depend on the amount of neutrals present to sustain a particular reaction. However, the primary mechanism for OH* formation is generally agreed to be through the ozone-hydrogen reaction:



This reaction has just enough energy to excite vibrational levels up to $v' = 9$ (3.23 eV in the ground state) but not $v' = 10$, which requires 3.49 eV. It is generally assumed that the lower vibrational levels are excited principally by the cascading of energy from the higher vibrational levels and collisional quenching from the level immediately above [*Chamberlain*, 1961; *Le Texier et al.*, 1987].

The emission layer created solely by this reaction is calculated to peak around 85-90 km, depending on the distribution of neutral species assumed [*Le Texier et al.*, 1987]. This altitude is in good agreement with rocket measurements; however, this single reaction does not fully explain the intensities seen in all of the rotational levels.

The three basic constituents which directly affect OH* formation are ozone, atomic hydrogen, and atomic oxygen [Espy, private communication, 1992]. The participation of ozone and atomic hydrogen in the creation of OH* is through the ozone-hydrogen reaction above. The dependence of OH* formation on the availability of atomic oxygen is due to its direct role in the formation of ozone through the reaction in Equation 2.19.



The distribution and concentration of these three constituents change from day to night and thus the character of the OH emission layer also changes from day to night. During the day, ozone is destroyed rapidly by photodissociation making it less available for the ozone-hydrogen reaction.



Ozone is also depleted during the day by the minor reaction



which also counts as a loss mechanism for atomic oxygen. Both atomic oxygen and atomic hydrogen are produced at lower altitudes in the daytime. Hydrogen is produced by the photodissociation of water vapor



while atomic oxygen is produced by the photodissociation of O₂



Because of the increased vertical extent of production of atomic hydrogen and atomic oxygen during the day along with a reduction in the amount of ozone, the resulting OH* layer tends to be weaker and more diffuse with a somewhat flat vertical profile.

At night OH* formation is primarily limited by the availability of atomic oxygen rather than ozone [Espy, private communication, 1992]. Since atomic oxygen density

increases with height and it is not produced by photodissociation in the lower atmosphere at night, the lower boundary for its availability is much higher at night.

All of these processes act to produce a vertically sharp emission layer at night.

CHAPTER 3

EMISSION SPECTRA

Radiation of energy occurs when an atom or molecule makes a transition between a higher and a lower energy state. In atoms, these transitions produce a spectrum that consists of emission lines corresponding to electrons jumping from one electronic level to another. The energy emitted in such a transition is discrete and quantized according to Bohr's postulate that only finite energy levels exist within the atomic structure and therefore only particular energies can be emitted in a transition from one level to another.

By contrast, the emission spectra of molecules have a great number of emission lines, extending out toward the red much farther than the atomic spectra. These additional lines exist because molecules can store energy in a variety of ways which single atoms cannot. Not only do molecules have the energy of their electronic state, they also have rotational and vibrational energy states. Rotational energy states exist because the atoms of the molecule can rotate about an axis through the center of gravity of the molecule itself. Additionally, because the atoms of the molecule are bound together by forces such that the individual atoms can vibrate about their equilibrium positions relative to one another, they also have vibrational energy states [Liou, 1980]. Combinations of the above three types of energy states are responsible for the complex structure seen in molecular spectra. However, just as it was for the atoms, molecules can only emit energy in discrete packets, and thus molecules also produce a predictable, though much more complex, spectrum.

By far the most energetic transitions are the electronic transitions which involve energies of a few electron volts. These generally give rise to ultraviolet or visible emissions. At the other end of the spectrum (literally!) are the extremely low energy emissions associated with the purely rotational transitions. These correspond to

emissions in the far infrared and microwave regions. Intermediate to electronic and rotational energy changes are the vibrational energy transitions. These transitions occur with energies so much larger than the minimum required for a rotational energy change that vibrational transitions never occur alone, but with many simultaneous rotational changes, resulting in the emission of a group of lines, constituting a vibration-rotation band. These generally occur in the near to intermediate infrared.

Molecular spectra are therefore characterized by *band systems* which consist of all the rotational transitions occurring within one vibrational transition. Each molecular band system has three branches, P, Q and R, which stem from the selection rules for rotational transitions. They are assigned the values $J' - J'' = -1, 0$, and 1 , respectively, where $J' - J''$ is related to the total angular momentum involved in the transition. Each of these primary branches has two sub-branches subscripted 1 and 2 corresponding to the $\pi_{3/2}$ and $\pi_{1/2}$ ground states, respectively. The Meinel (6,2) $P_1(3)$ 8430 Å OH emission belongs to the P_1 branch of the 6-2 ($v' = 6$ to $v'' = 2$) vibrational transition within the $\pi_{3/2}$ ground state of the hydroxyl molecule. The (3) indicates which particular line in the P_1 branch is being considered (in this case the 8430 Å line). Figure 10 shows the rotational band structure for the (6,2) Meinel OH band.

Finally, beyond the rotation-vibration band structure, certain molecular gases observed under high resolution appear to be composed of an even larger number of individual and characteristic spectral lines [Liou, 1980]. This is called hyperfine structure. Hyperfine structure occurs in molecules where unlike atoms make up the molecule (OH for example). Since these molecules are not symmetric, the molecule itself will have an angular moment which interacts with the magnetic fields of the individual atomic electrons. As a result there are many more possible finite energy levels and this is seen in the spectrum as a splitting of the ordinary rotational levels into complex rotational levels [Liou, 1980].

Although not visible in Figure 10, the OH 8430 Å emission is actually composed of two closely spaced lines. This hyperfine structure doublet is shown in Figure 11. The separation between these two lines is approximately 0.19 Å.

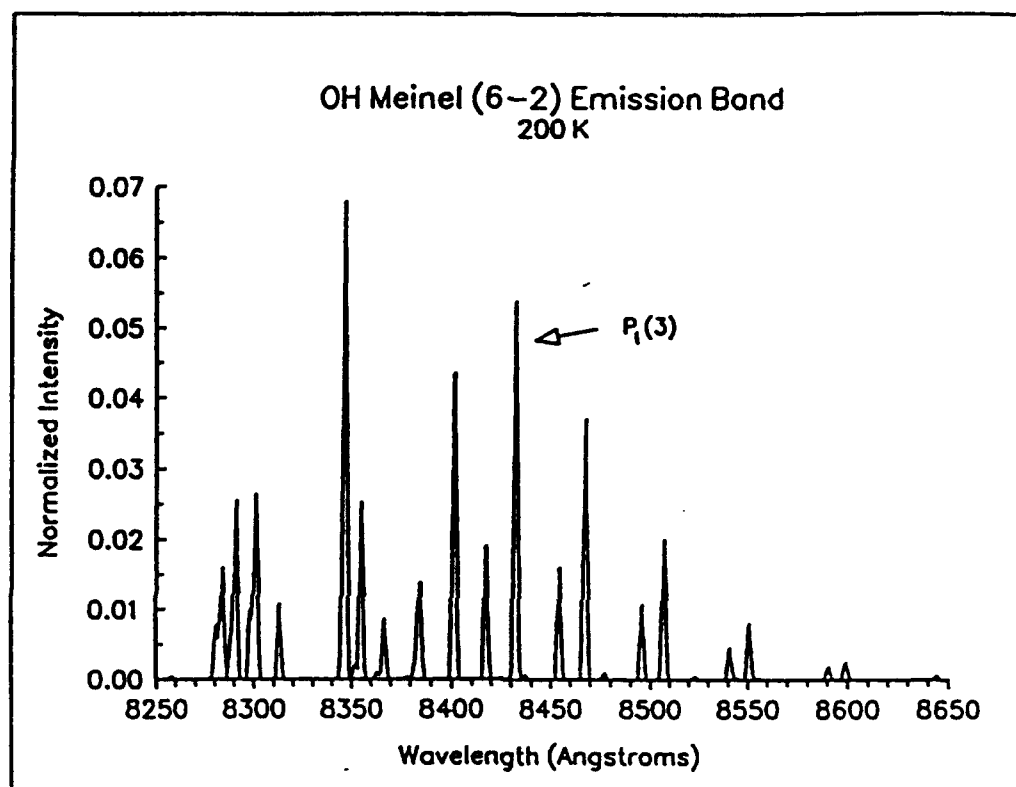


Fig. 10. Rotational Band Structure for the Meinel (6-2) OH band [Figure courtesy of *Pat Espy*].

The effect of the presence of hyperfine structure to observation of a particular emission line depends on the resolution of the instrument used. If the two lines can be separately resolved, the effect is minimal. However, if, under observation the lines appear as a single line, then their combined effect is to artificially broaden the observed emission profile. This problem can theoretically be minimized by selecting the spacing between the parallel plates of the interferometer such that the two emission lines will be superimposed. This will not only effectively eliminate the second line which might

interfere with the observation, but it will also double the apparent intensity in the line which is observed.

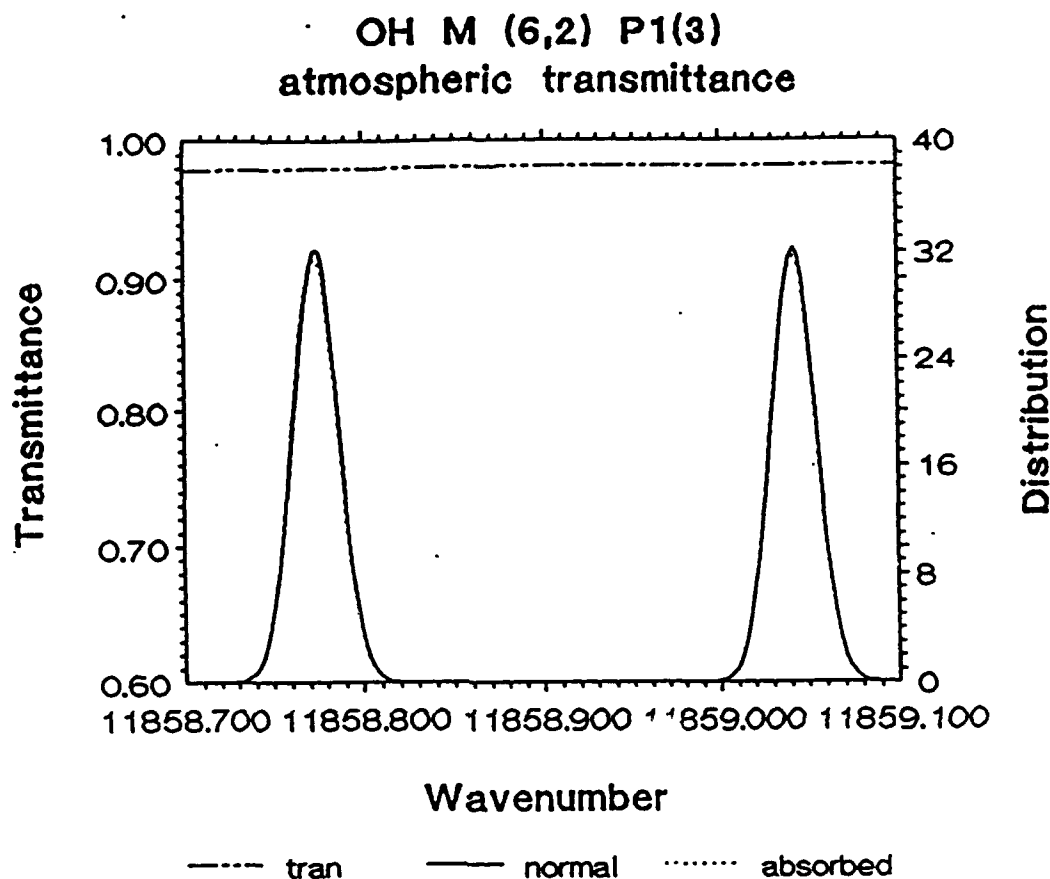


Fig. 11. Hyperfine doublet of the 8430 Å OH emission [Figure courtesy of Pat Espy and Mark Hammond].

3.1 Emissions Observed in the Mesopause Region

The primary emissions observed at mesopause heights tend to be those of the forbidden transitions of neutral and ionized species, although some important emissions do result from permitted transitions in the region [Chamberlain, 1961]. The transitions are termed "forbidden" because they violate the selection rules for electric dipole radiation and have transition probabilities that are orders of magnitude smaller than those of the allowed transitions [Vallance Jones, 1991].

Because the long lifetime of the upper state allows the atom or molecule to reach statistical equilibrium with the surrounding medium before radiating their energy, the Doppler profile of the emitted radiation reflects both the kinetic temperature of the region where the emission occurred (the Doppler width), and the bulk motion of the wind at the level (the Doppler shift).

The lifetime of the OH 8430 Å emission is computed by *Ware* [1980] to be approximately 0.81 seconds, consistent with its classification as a forbidden transition¹. Collisions have a large effect on the effective lifetime of the upper state of a particular transition. This can be seen by considering the forbidden transition of OI at 5577 Å. This emission occurs near the mesopause at 97 km, and in the F region ionosphere, near 250 km. The radiative lifetime of the upper state associated with this transition is ~0.75 seconds [*Vallance Jones*, 1991]. At 97 km, the density of the atmosphere allows the excited oxygen atoms to collide with many other atoms and molecules in the surrounding medium before radiation. In this situation a measurement of the motion and kinetic temperature of the emitting atoms will be representative of the motion and temperature of the ambient atmosphere at that level. At F-region altitudes where the density of neutral particles is much lower, far fewer collisions will occur in the 0.75 seconds before emission, and no conclusions can be drawn about the neutral atmospheric winds and temperatures based on the OI 5577 Å measurements.

3.2 Emission Line Profiles

An emission line profile reveals the distribution of intensity with wavelength for a particular transition. Because each emission results from a specific quantized energy loss

¹The radiative lifetime of OH was calculated by *Ware* [1980] from Einstein coefficients which were thermally averaged for 200 K taking full account of both spin-uncoupling and vibrational-rotational coupling effects.

from the molecule, we would anticipate the light radiated during emission to be monochromatic, corresponding to that specific energy loss. This would imply an emission profile resembling a simple Delta function at that wavelength. However, purely monochromatic emission is practically never observed. Energy emitted during transitions is normally changed slightly due to both external influences on the emitting atoms and molecules (collisions), and due to the effects of the finite lifetime of the upper state (natural broadening) [Tolansky, 1955]. These factors serve to modify the shape of the emission line profile, giving spectral lines of finite widths.

Natural broadening is found to be significant only in transitions where the mean lifetime of the upper state is very small. This is true in permitted transitions such as for the Schumann-Runge O₂ bands where the mean lifetime is $\sim 10^{-8}$ seconds. For transitions where the typical lifetime of the upper state is on the order of one second or more, such as for the vibration-rotation transitions in the infrared, natural broadening is completely negligible [Andrews *et al.*, 1987]. For this reason, natural broadening should not affect the OH 8430 Å or the OI 6300 Å emission profiles examined in this thesis.

Measured spectral lines resulting from forbidden transitions of OH and OI have shapes which are instead primarily determined by the temperature of the emitting region and collisions. The temperature at the emission level leads to Doppler broadening, and collisions with other particles result in pressure broadening.

3.2.1 Doppler Broadening

Even though the mesopause region is not in thermal equilibrium, it is a region characterized by statistical equilibrium. Statistical equilibrium requires that the population of particles in a particular energy level remains constant, or rather that the number of atoms or molecules entering a particular state is equal to the number leaving the same state in the same time interval, which is true where the lifetimes of the excited levels are short compared with the duration of the excitation. This allows the assumed

distribution of energies, and hence velocities among the particles, to follow a Boltzmann distribution [Chamberlain, 1961]. This can be written:

$$f(v)dv = 4\pi\left\{\frac{M}{2\pi kT}\right\}^{\frac{3}{2}}v^2e^{\frac{-Mv^2}{2kT}}dv \quad (3.1)$$

In this equation, T is the absolute temperature, M is the molecular mass, and k is the Boltzmann constant. Equation 3.1 basically says that if molecular mass is constant, the distribution of velocities in a volume will depend solely on the temperature of the medium.

The use of Equation 3.1 implies that the molecules in the volume being considered all have the same temperature, or rather that they have achieved thermalization. The degree of thermalization reached by the emitting molecules depends on the number of collisions undergone before radiation. Ware [1980] provided the following information in regard to the degree of thermalization achieved by the hydroxyl molecule near 87 km.

The mean time between collisions of neutral atmospheric molecules is approximated by Baker [1978] as

$$\tau = 4.4 \times 10^{-12} \exp(0.19 h)$$

where h is the altitude in km. At 87 km, this gives a value of 6.6×10^{-5} seconds between collisions or about 15 collisions per millisecond. Nicholls [1971] has estimated that 72 collisions were required for thermalization to within 1% of an ambient temperature of 500 K and that 48 collisions were required for a temperature of 165 K.

Ware [1980] suggested that 10 collisions would be adequate to obtain a Boltzmann distribution. This would require a mean radiative lifetime of from about 0.6 to 3 milliseconds for rotational thermalization to a Boltzmann distribution. As noted earlier, the lifetime of the excited OH molecule is ~0.81 seconds, thus easily achieving a Boltzmann distribution.

Because the molecules have an initial spread of velocities which follow a Boltzmann distribution, the resulting Doppler-shifted spread of velocities will have this

same distribution. This distribution, also called a Gaussian or Doppler distribution, is shown by the dashed line in Figure 12.

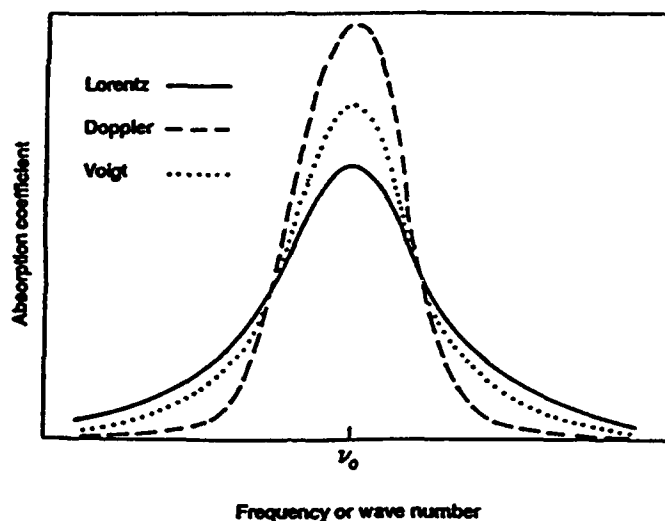


Fig. 12. Doppler and Lorentz line shapes for approximately equal half-widths and intensities with the corresponding Voigt profile [Andrews *et al.*, 1987].

3.2.2 Pressure Broadening

Pressure broadening, also called collisional broadening, is due to collisions of the emitting molecule with other emitting molecules and neutral particles. The profile which results from collisional broadening is related to the damping of the particle motion due to collisions which tend to smooth the distribution of velocities and hence the process tends to widen the original profile. Broadening due to collisions is a complex process but the general shape of the profile due purely to collisions is Lorentzian [Andrews *et al.*, 1987]. This is shown by the solid line in Figure 12.

3.3 The Observed OH Profile

It is necessary to consider both Doppler and collisional broadening when the two processes are of about the same importance. The combined profile may be obtained by

taking the Doppler broadened Gaussian profile and convolving it with the Lorentzian profile due to collisional broadening. This combined profile is called a Voigt profile (Figure 12). *Clough et al.* [1981] calculated the altitude at which an emission profile becomes purely Gaussian based on the wavelength of emission. For a wavelength of 8430 Å, this occurs at approximately 40 km. Therefore, the observed OH intensity distribution at 87 km should be purely Gaussian.

In addition to the signal from the broadened emission line, the signal entering the instrument will also contain photons from the underlying airglow continuum, the stellar background, and from any nearby emission lines that fall within the filter bandpass. Background emissions have the effect of simultaneously increasing the photon count at all wavelengths, effectively boosting the entire intensity spectrum by some constant amount. Contamination from emission lines at other wavelengths will cause additional emission peaks to occur in the collected image. If the two emission lines partially overlap, the spectral line of interest will no longer be isolated, and it will become much more difficult to determine the half-width to be used in the temperature calculations. Extraneous emission lines can be removed by choosing an appropriately narrow filter.

The previous discussion considers only how the emission profile is affected by its atmospheric environment. Additionally, one must consider what happens to the emission profile as it passes through the instrument to be recorded. Because the instrument has a finite aperture and has imperfections on the surfaces of the parallel plates and the optics, the instrument distorts the shape of the emission line such that some instrumental function is convolved with the source profile as the light passes through the instrument. This instrument profile is very difficult to obtain mathematically because it is hard to accurately characterize all of the factors which affect this profile. *Hernandez* [1986] is an excellent source for the complete procedure for attempting these calculations.

By far a simpler way to find this profile is to determine it experimentally. A source with a very narrow (nearly monochromatic) spectral emission profile, such as a single-mode laser, is passed through the instrument and recorded. This will result in a profile widened solely by instrumental broadening and should represent the effect of the instrument on the recorded emission spectrum. Knowing the instrument profile, we can in principle remove (deconvolve) it from the total measured 8430 Å emission profile.

CHAPTER 4

FABRY-PEROT IMAGES AND INTERFEROMETRY

The images recorded by the Fabry-Perot are two-dimensional circular fringes like the one shown in Figure 13. This image was recorded at the Bear Lake Observatory.

4.1 The Interference Intensity Pattern

To explain the circular image produced by the Fabry-Perot, it is necessary to briefly outline some fundamental principles of optics and interferometry. For a fuller development the reader is referred to *Hecht* [1987], *Tolansky* [1955] or any standard optics text.

4.1.1 Transmission Through an Ideal Etalon

Consider a broad diffuse source of approximately monochromatic light incident at arbitrary angles to the two semi-transparent flat surfaces separated by a constant distance. If the inside of each surface is coated with a highly reflective material, light impinging on the top plate will be multiply reflected within the gap before finally being transmitted out the other side. At each point of reflection within the gap, partial transmission will occur and result in a set of transmitted waves which consecutively diminish in amplitude and have a phase which varies from the preceding component by

$$\delta = \frac{4\pi\mu t \cos \theta}{\lambda_0} \quad (4.1)$$

where δ is the phase difference between the two successive waves, μ is the index of refraction between the plates, t is the distance between the plates, θ is the angle of incidence, and λ_0 is the wavelength of the incident radiation.

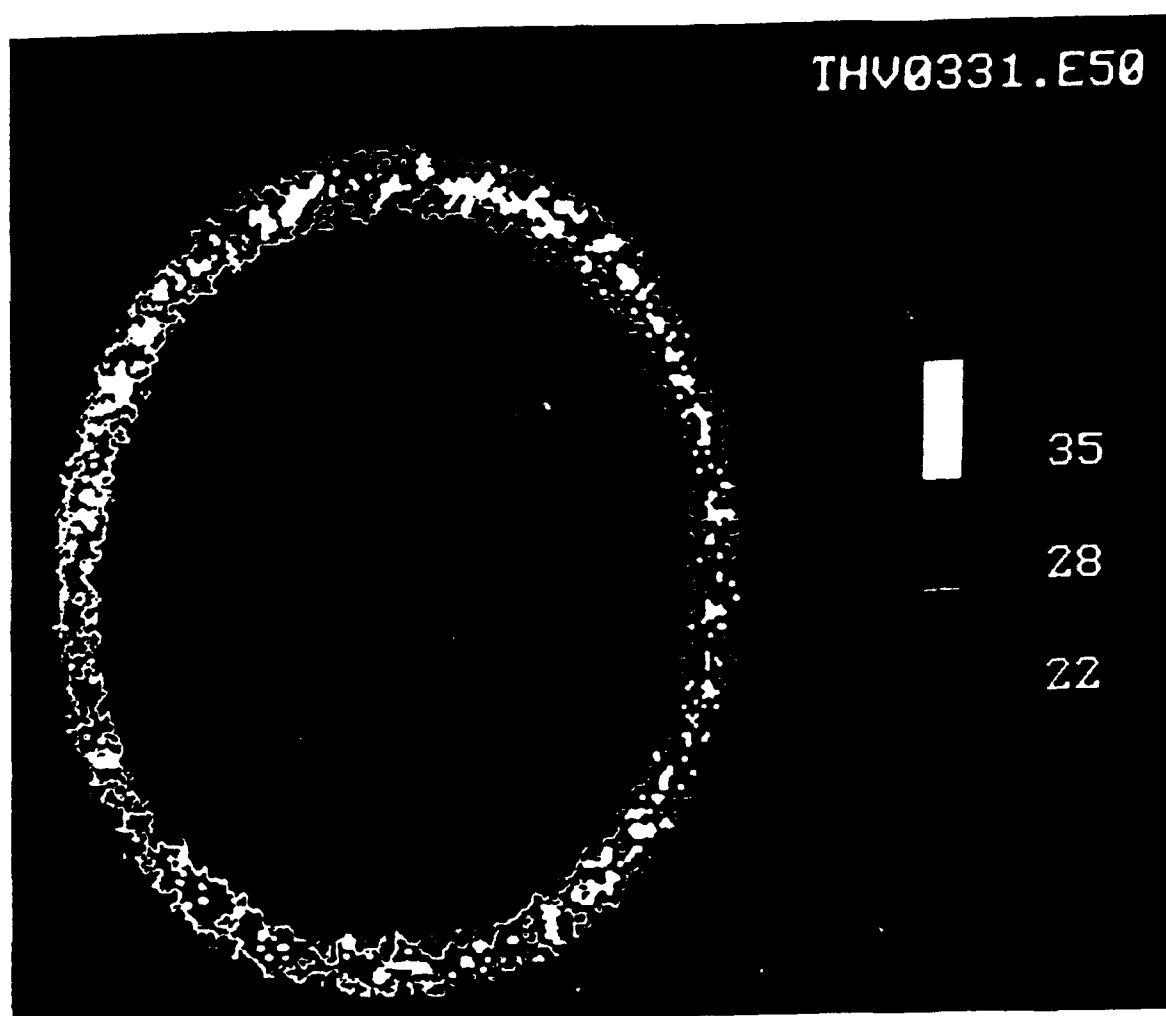


Fig. 13. Fabry-Perot circular fringe pattern of the OH emission at 8430 Å.

The path difference between two successive transmitted waves will be

$$d = 2\mu t \cos \theta \quad (4.2)$$

Figure 14 shows this reflection/transmission phenomenon.

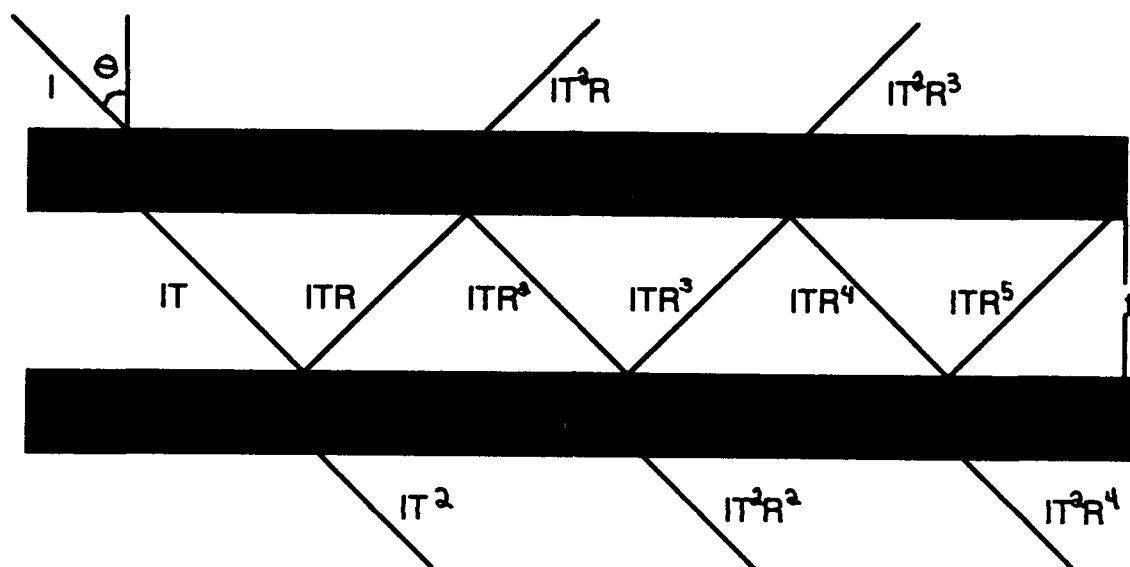


Fig. 14. Reflection and transmission between two parallel plates.

The light rays which eventually emerge from the plates after being multiply reflected are parallel to one another. If a positive lens is placed just beyond the plates, these individual beams will be brought together at the focal point of the lens, causing them to interfere. When the peaks of the recombining waves occur at the same place, constructive interference will occur and the resulting amplitude will be large. When the peak of one wave and the minimum of another come together, destructive interference will occur and the resulting wave amplitude will be very small or zero.

Constructive interference occurs for waves that are incident on the flat plates at the same angle (θ), where θ is a particular angle at which a whole number of wavelengths exactly fit the optical path difference, d . This results in waves which are related in phase when they emerge from the plates and subsequently when they interfere. For an instrument with circular symmetry, such as the Fabry-Perot, all of the rays incident at a given angle will result in a single circular fringe. Returning to Equations 4.1 and 4.2, since μ , t , and λ_0 are constants, one can see that the phase and path difference depend only on the angle of incidence.

Because airglow occurs as a broad source, light will be incident on the instrument at a range of angles resulting in the appearance of a number of concentric rings rather than just a single ring. Each ring will represent a different order of interference. The transmitted intensity pattern is a set of light rings on a dark background. Fringes which occur due to light incident at equal inclination are often called Haidinger fringes after W. Haidinger who first observed this phenomenon.

The Airy function is the mathematical ideal for the intensity distribution resulting from an extended source incident upon two parallel surfaces in the absence of absorption. The equation for the transmitted intensity distribution of the Airy function is given by

$$\frac{I_t}{I_i} = \frac{1}{1 + \left\{ \frac{4R}{(1-R)^2} \right\} \sin^2 \frac{\delta}{2}} \quad (4.3)$$

where I_t is the transmitted intensity, I_i is the incident intensity, R is the reflectance, and δ is the phase.

The Airy function has a maximum intensity of unity when $\sin^2 (\delta / 2) = 0$. This means that for an ideal instrument where absorption is zero, the transmitted fringe maximum has an intensity equal to that of the incident light, regardless of what the reflectance of the plates may be [Tolansky, 1955].

The Airy disk resulting from this equation is shown in Figure 15.

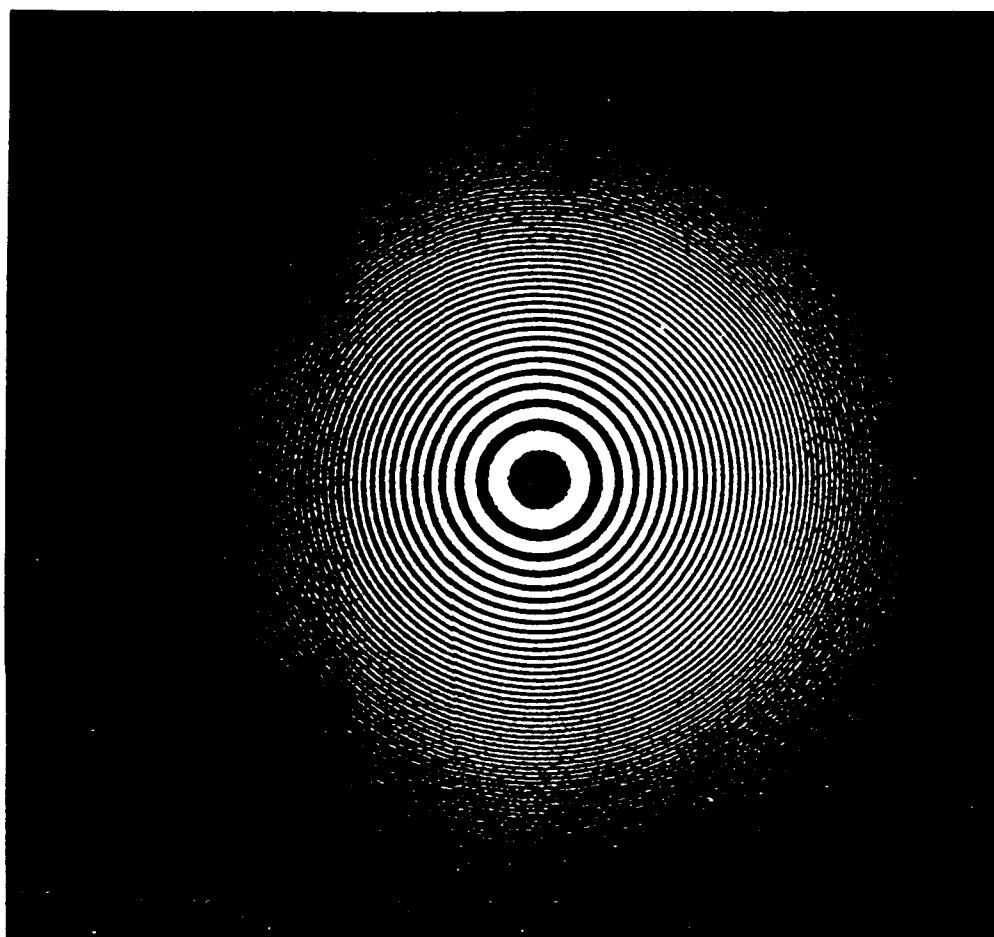


Fig. 15. Airy Disk [*Hernandez, 1986*].

Notice that the concentric rings get closer together with increasing radius. This is because the position of the fringe is a function of the cosine of the angle of incidence, rather than a first order function (coming up in Equation 4.8).

4.1.2 Reflectance

For a real system where absorption plays a role, the value of reflectance of the plate surfaces becomes very important. The modified equation for the transmitted intensity allowing for absorption becomes

$$\frac{I_t}{I_i} = \left[1 - \frac{A}{(1-R)} \right]^2 \frac{1}{1 + F \sin^2 \frac{\delta}{2}} \quad (4.4)$$

where A is absorptance and F , called the coefficient of finesse, has been substituted as

$F = \frac{4R}{(1-R)^2}$. This gives a peak transmission every 2π radians with a magnitude

$$\frac{I_t}{I_i} = \left[1 - \frac{A}{(1-R)} \right]^2 \quad (4.5)$$

As absorptance is increased, the transmitted intensity decreases dramatically.

The width of the resulting fringes depends solely on the value of reflectance. Equation 4.6 gives the full-width at half maximum of the fringe as a function of reflectance.

$$\gamma = \frac{4}{\sqrt{F}} = 2 \left[\frac{R}{(1-R)^2} \right]^{-1/2} \quad (4.6)$$

To get distinct fringes, R must be very close to unity. Figure 16 shows the transmitted intensity for three different values of reflectance.

Two obvious changes occur as lower values of reflectance are used. First, the width of the fringe changes according to Equation 4.6, with higher values giving narrower fringes, and lower values resulting in broader fringes. The second effect is that the difference between the maximum and minimum intensities changes dramatically as the reflectance is varied. This is because at low values of reflectance, transmission is greater for all θ and the result is that the fringes are very indistinct. When reflectance is

high, not only do the fringes become much more distinct, but the intensity falls off much less quickly with increasing θ .

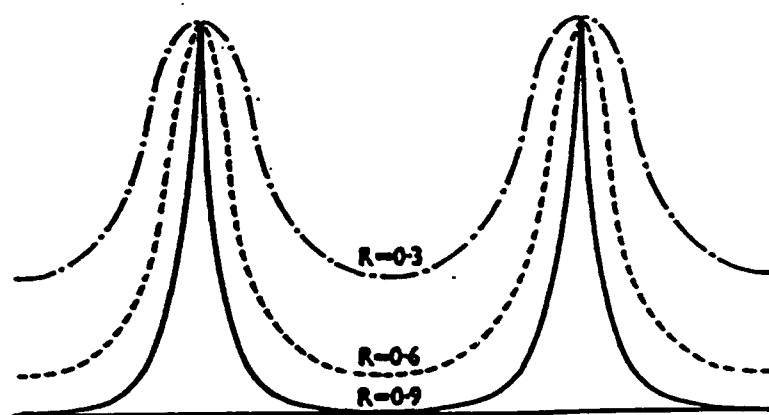


Fig. 16. Intensity variation with reflectance for three values of R ; 0.3, 0.6, 0.9. [After Tolansky, 1955].

4.1.3 Instrument Finesse

Closely tied to the reflectance is a parameter called finesse, which is basically a measure of how good the system is in terms of its ability to resolve closely spaced line. The higher the finesse, the better this ability. The finesse of the instrument is calculated using the ratio of the separation of adjacent maxima, or orders, to the full width at half maximum of the emission line. If the reflectance is known, this can also be found using Equation 4.7 which assumes an ideal instrument with no defects.

$$\mathfrak{F} = \frac{\pi\sqrt{F}}{2} \quad (4.7)$$

An actual system will experience a reduction in its finesse from this ideal due to the effects of a finite aperture and because of defects on the etalon and optics surfaces and non-zero absorption. The upper limit for the value of finesse occurs because as the half-width decreases, so does the peak transmission. At some high value of finesse the fringes disappear altogether.

The finesse of an instrument is temperature dependent because the reflectance of the plate coating material is temperature dependent. However, once an instrument is set up and working, the finesse will generally be a constant of the instrument.

4.1.4 Order of Interference

The Fabry-Perot basically functions as a device to transform wavelength into an angular displacement [Hernandez, 1986]. Equation 4.8 gives the relationship for the angular position (θ) of a fringe image on the photocathode due to light of a particular wavelength (λ). It is clear from this equation that the position of the fringe is strongly affected by the plate spacing (t). The term n is the order of interference, which is the number of whole wavelengths which fit in the path difference for successive reflections between the etalon plates at a given angle, θ .

$$n\lambda = 2\mu t \cos \theta \quad (4.8)$$

When n is a whole number, light fringes will appear in the transmission pattern, and when n is $n+1/2$, dark fringes appear. For the Fabry-Perot at Bear Lake, because μ , t , and λ are constants, the only way to get more than one concentric ring (or more than one order) to appear in the image, is to allow θ to vary. This is done simply by having a finite field of view. Other Fabry-Perot configurations can get more than one order by varying t , the plate spacing or μ the index of refraction. For n , t , and μ constant, we see

that the longest observed wavelength occurs at the center and that we go to shorter wavelengths as we scan away from the center.

If λ and μ are constants, then the spacing of the etalon plates determines the order of interference and the angular displacement of the fringes. Successive fringes will occur for those values of θ which correspond to integer values of n such that $n = n_0 \cos \theta$. Notice that this means that the order of interference is a maximum at the center and decreases from the center outwards.

The maximum order of interference at the center of the image is found by letting $\theta = 0$ in Equation 4.8 (normal incidence). The central order n_0 is then

$$n_0 = \frac{2\mu t}{\lambda} \quad (4.9)$$

Since we only know the plate separation of our instrument to four significant figures (20.49 mm), it is not possible to determine the precise order of interference at the center. An approximate order of interference for normal incidence can be calculated by substituting in 8430 Å for the wavelength and 20.49 mm for the plate separation. This gives $n_0 = 48,612$.

4.1.4.1 Plate Spacing

The spacing between plates has a major impact on the observations. It impacts the field of view, the spectral resolution, and the width of the spectral region observed. A big spectral resolution improves the precision of the wind observations. The width of the spectral region has to be wide enough that the background can be determined on both sides of the emission. Approximately 1 1/2 free spectral ranges (Section 4.3) need to be included so that this parameter can be easily determined. In addition, we want the spacing such that the hyperfine lines (one at order n , the other at order $n-1$) are precisely overlapped.

Because it is important for us to also measure the emission at 6300 Å, the gap selected for the Bear Lake instrument could not be so large as to eliminate the 6300 Å

fringes. The spacing for our instrument is currently set at 20.49 mm, allowing one complete 8430 Å fringe to be imaged and two and a half 6300 Å fringes to be imaged.

As mentioned previously, the other thing that was attempted in setting the gap was to try to get adjacent orders of the hyperfine structure doublet at 8430 Å to overlap such that only a single emission line is observed.

4.2 Reducing the Two-Dimensional Images

To get the two-dimensional images collected by the Fabry-Perot into a usable form, they are reduced using a circular integration to a one-dimensional fringe profile. An example of this reduced profile, called an interferogram, is shown in Figure 17.

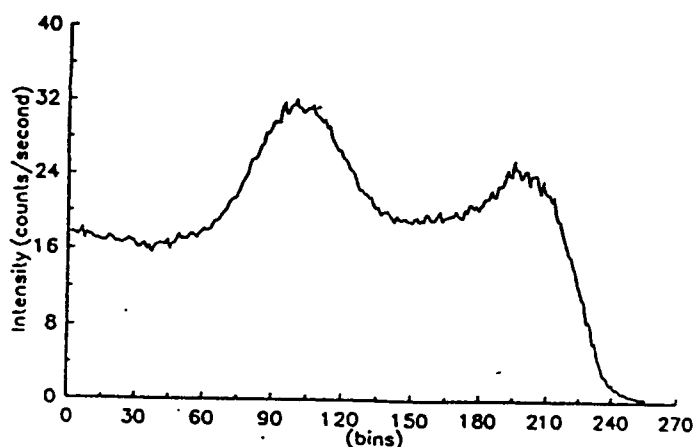


Fig. 17. One-dimensional fringe profile.

A special type of reduction is necessary because the rings imaged on the detector get closer together with increasing radius. If one were to do an ordinary circular integration around the fringe pattern in radius space, one would find that the width and intensity of the peaks would decrease rapidly with increasing radius. The resulting profile would be difficult to fit and interpret since the horizontal axis would not represent

equal increments in wavelength. To eliminate this problem, the data reduction procedure incorporates a sample-weighted algorithm by *Lloyd* [1985], which reduces the data to radius-squared space in the following manner.

The two-dimensional image is divided into 256 equal-area annular rings starting at the center. The photons are then summed around each ring and the count is placed in a numbered "bin" corresponding to the position of the ring in the image. This results in peaks which are evenly spaced with equal width at half height, and each increment along the horizontal axis, hereafter referred to as a "bin," represents an equal decrease in wavelength.

4.2.1 Center Coordinates of the Image

The center of the circular image about which the data are reduced is determined visually. It is important to find the center of the ring pattern carefully when first setting up the instrument, as all subsequent data rely on the accuracy of the center when it is reduced to radius-squared form. An error in the center position will cause the integrated fringe pattern to be widened and possibly skewed. As a result, the peak location and Doppler will be less precise. Temperature measurements derived from such profiles will be inaccurate.

To reduce the potential for this, the center is meticulously tweaked before data are collected such that the narrowest possible integrated profile is obtained. Fortunately, once the center is found, it is quite stable and a new center must be found only when the instrument is jarred or an adjustment is made to the hardware.

4.3 Free Spectral Range

The distance between two consecutive maxima, or orders, for a monochromatic source is called the free spectral range (FSR). Knowing the free spectral range accurately is important because it is used directly in calculating the factor which converts the Doppler shift in bin position on the interferogram to the equivalent wind speed during

the data processing. Thus an error in the value of the free spectral range would introduce a systematic error into the wind results.

The free spectral range can be measured directly from the interferograms simply by finding the positions of two consecutive peaks and determining the distance between them. Ideally this is done over many successive images to obtain a very precise value.

An obvious problem occurs when trying to determine the free spectral range for the 8430 Å emission from the data if only one peak appears on the interferogram, as was the case for some of our data. This makes it necessary to find the free spectral range in a different way, applying the free spectral range of a different emission which does give two clear peaks. We can use our measurement of the 6300 Å emission for this purpose.

This is accomplished by relating the wavelength (λ) of the emission directly to the radius (r) of the peak position. The final expression is derived from the relation $n\lambda = 2\mu t \cos \theta$ by first replacing the expression for $\cos \theta$ with

$$\frac{L}{(L^2 + r_n^2)^{1/2}} \quad (4.10)$$

where L is the effective focal length and r_n is the radius to the fringe for a particular order of interference. This can be rewritten as

$$\frac{1}{\left(1 + \frac{r_n^2}{L^2}\right)^{1/2}} \quad (4.11)$$

Since $r_n^2 \ll L^2$ a Taylor series expansion can be performed on the expression to obtain

$$1 - \frac{r_n^2}{2L^2} \quad (4.12)$$

Substituting this for $\cos \theta$ and assuming that the index of refraction is unity at both wavelengths, we obtain

$$n\lambda = 2t \left(1 - \frac{r_s^2}{2L^2} \right) \quad (4.13)$$

The free spectral range is defined as the distance between the peaks of successive orders, n and $n-1$, so that $FSR = (r_n^2 - r_{n-1}^2)$. Equation 4.13 can be applied at two different wavelengths, λ_1 and λ_2 , to give

$$\frac{\lambda_1}{\lambda_2} = \frac{t_1/L_1^2}{t_2/L_2^2} \frac{FSR_1}{FSR_2} \quad (4.14)$$

From this it can be seen that if the physical constants of the instrument are not changed (t/L^2 is constant), the free spectral range may be determined from a simple comparison of ratios.

$$\frac{\lambda_1}{\lambda_2} = \frac{FSR_1}{FSR_2} \quad (4.15)$$

Thus we can use the free spectral range found from the 6300 Å data and then easily scale it to a free spectral range for 8430 Å. It is important in applying this procedure to use data (at both wavelengths) in which the center coordinates used to reduce the data are not too different. If the centers are very different, this would imply that some type of adjustment was made to the system and that the ratio (t/L^2) is no longer the same for the two wavelengths.

Another useful technique for finding the FSR of an emission is by using the autocorrelation function. The correlation of two functions will be large at some value of the first function if the first function is a close copy of the second, and the second only "lags" the first by some time or distance. Because the data in the reduced profile are a repeating function, we can find the distance between the peaks using this method.

Since the FSR depends exclusively on the instrument configuration parameters, it is only necessary to recalculate the FSR whenever the instrument configuration is changed.

4.4 Spectral Resolution

Doppler shifts associated with winds typical at mesopause heights are very small. A wind of 50 m/s at 85 km for an OH 8430 Å emission would produce a Doppler shift of approximately 1.4 mÅ using the expression

$$v = c \frac{\Delta\lambda}{\lambda} \quad (4.16)$$

The extremely high resolving power of the Fabry-Perot interferometer allows it to detect these tiny shifts that appear as a shift in the position of the peak of the emission profile. Because the fringes have a finite width, the instrument will have a finite resolving power. In other words, it has the ability to distinguish two closely spaced lines down to some minimum value called the Rayleigh criterion [Hernandez, 1986]. This is done using Equation 4.15.

$$\Delta\lambda_o = \lambda_o \frac{4.2}{2\pi n \sqrt{F}} \quad (4.17)$$

By using a central order of interference of 48612 for 8430 Å, the wavelength resolution is $\Delta\lambda_o \approx 5.87$ mÅ. This makes the resolving power $\mathcal{R} = \lambda_o / \Delta\lambda_o \approx 1,400,000$. At 6300 Å using a central order of interference of 65045, the wavelength resolution is ≈ 3.28 mÅ, giving a resolving power of $\approx 1,900,000$.

4.5 Effective Finesse Calculation from the Data

The finesse is calculated by dividing the free spectral range by the FWHH where both values are given in bins.

$$EffectiveFinesse = \frac{FSR(bins)}{FWHH(bins)} \quad (4.18)$$

The average HWHH for the OH 8430 Å data was calculated as 21.75 bins. This gives a finesse of ~3.5. For the OI 6300 Å data the average HWHH was 24.4 bins, giving a finesse of ~2.2. The actual instrumental finesse will be somewhat higher than this due to the fact that the emission profile is still included in the total profile.

CHAPTER 5

HARDWARE

5.1 The Fabry-Perot Interferometer

The observations were carried out with an Imaging Fabry-Perot Interferometer (IFPI). The IFPI is a joint research project between USU and the University College of London (UCL). The instrument is similar to others built by UCL and partially described in *Rees et al.* [1989]. The Fabry-Perot is hung in the center of a small blackened room within the observatory structure and set such that the optical axis is exactly vertical. A hole cut through the roof allows the instrument to view the sky aided by a mirror system, and a Plexiglas dome cover protects the instrument and electronics from the elements. Because the Imaging Photon Detector (IPD) is extremely sensitive to light, the entire instrument is encased with light-tight covers which are solidly black. Additional equipment includes two thermal control systems and two electronic controller units. A computer drives the electronic controller units and manages data acquisition and storage for the instrument.

The observatory structure consists of a mobile home partitioned into instrument bays, and utility areas which have been built onto the basic structure. Figure 18 shows schematically the Fabry-Perot interferometer building and setup.

The following sections describe the individual components of the instrument at Bear Lake and refer to Figure 19.

5.1.1. The Scanning Mirror System

The scanning mirror system consists of two mirrors which are used in combination to deflect light from different regions of the sky. The primary mirror is a

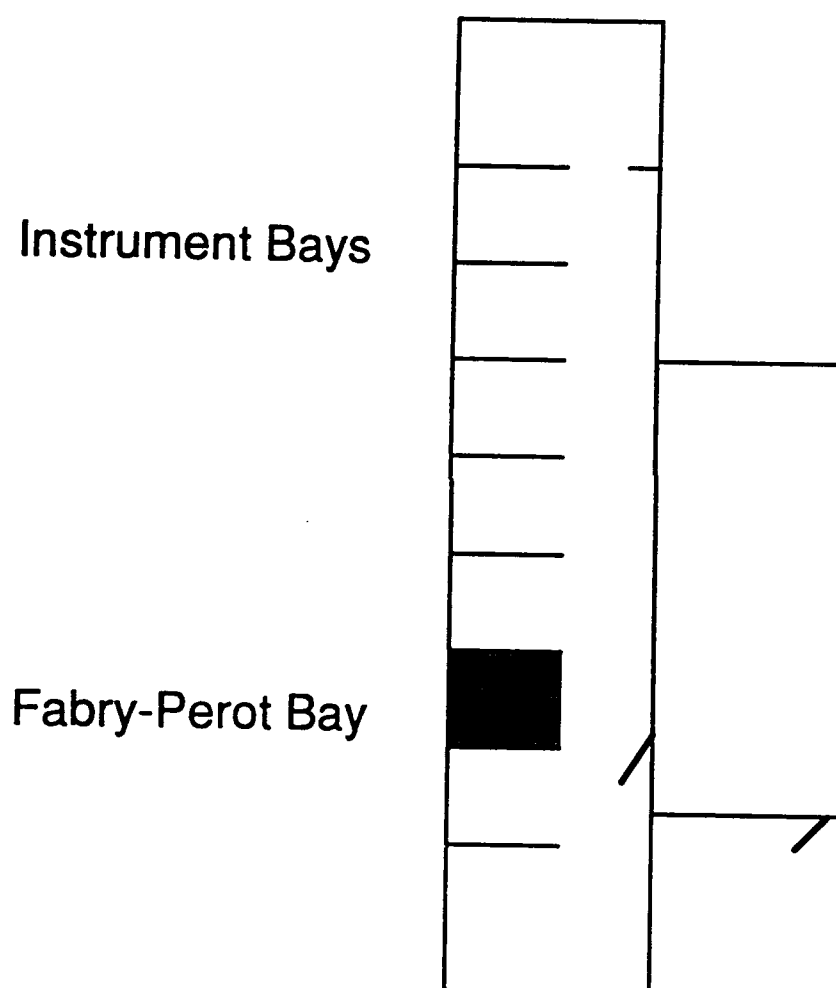


Fig. 18. Bear Lake Observatory and the location of the Imaging Fabry-Perot interferometer.

FABRY-PEROT INTERFEROMETER

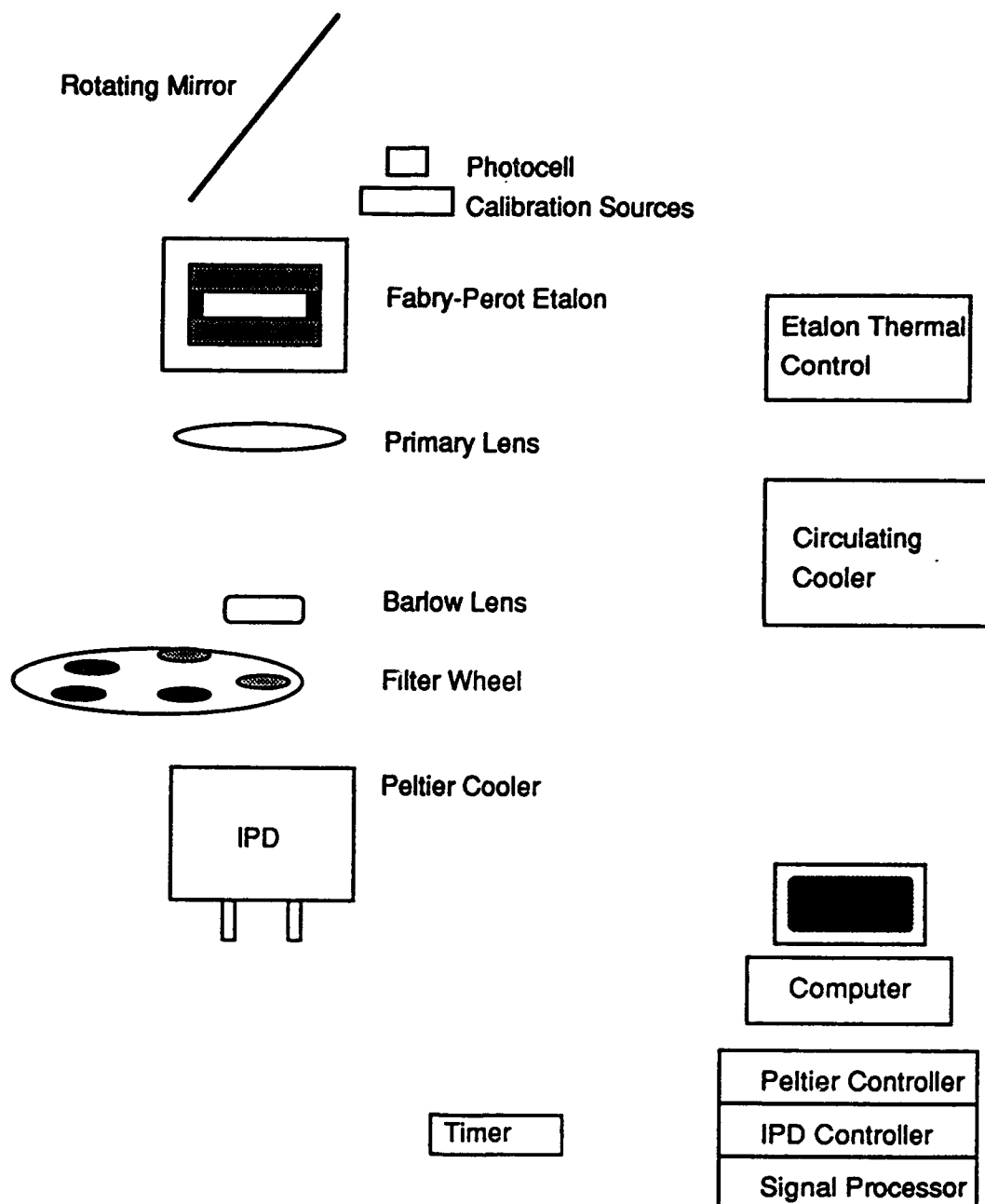


Fig. 19. The Imaging Fabry-Perot interferometer and components.

front-surface mirror mounted directly above the etalon with the majority of the mirror lying above roof level. It is tilted such that the normal to the mirror surface is at a zenith angle of 120° . This allows emissions from an elevation angle of 30° to be directed into the instrument. This mirror can be adjusted manually for different elevation angles as desired.

The second mirror, a rear surface mirror, is set with the normal to the mirror surface pointing 30° off zenith. It is positioned within the Plexiglas dome such that when the primary mirror is moved into parallel with it, vertical measurements can be made. This "zenith" mirror was aligned using a small laboratory laser. The laser beam was pointed vertically downward onto the zenith mirror and the alignment was found by adjusting the mirror until the reflected beam appeared to return to its source (the laser). Using this method, the mirror was visually aligned to a precision of better than one tenth of a degree. At the same time, the alignment of the Fabry-Perot itself was examined and found to be vertical to within one tenth of a degree.

The primary mirror rotates toward positive azimuth, stopping at any selected position to the north, northeast, east, southeast, south, southwest, west, northwest or zenith. The calibration lamp is sampled at a position between the southeast and south positions. A position exists for looking at a laser. The mirror is driven by a motor mounted just below the mirror, and positions are found by an optical sensor which looks for markings on the rim at the top of the instrument.

The mirror can be commanded to stop at any of the positions, in any order, for any length of time. This allows versatility in choosing an integration time which best suits the strength of the emission, with a weaker emission generally requiring a longer integration time to obtain an acceptable uncertainty. (Integration time is the amount of time that the detector is allowed to collect photons to create a single image.) Statistically, whenever a measurement involves the counting of a particular quantity, the

uncertainty is proportional to the square root of the number of counts. This is true because the distribution about the mean value is a Poisson distribution [Bevington, 1969].

The trade-off for choosing a long integration time is that there is also a need to cycle through all of the selected positions in the mirror sequence within a reasonable amount of time compared to natural variations, e.g., good time resolution. For instance, if a 30-minute integration were done in each of the 10 positions, there would be a very small uncertainty in the measurements, but it would be more than 5 hours before there were two consecutive measurements in the same direction. By the Nyquist sampling theorem, this would mean that one could not expect to resolve any wave phenomena which occurred on a time shorter than 10 hours. The Nyquist theorem states that to accurately reproduce the wave, one needs to sample at twice the highest frequency present in the signal.

The lower limit for time resolution when observing OH is approximately 2 minutes for an uncertainty less than 10-15 m/s. This would mean the shortest period wave for 1 line-of-sight is 4 minutes; for 4 line-of-sights to find a vector and the calibration source it is 20 minutes.

An integration time of 240 seconds (4 minutes) is generally used for collecting 8430 Å OH emissions at the Bear Lake Observatory. By using this, a complete cycle of the positions can be completed in approximately 42 minutes (10 positions which require 4 minutes each, plus a minute or so for the accumulated movement of the mirror between images). Each direction is sampled every 42 minutes, giving us the ability to accurately resolve waves with periods of 1 1/2 hours or longer. This should allow the resolution of the lower order tidal components and gravity waves with periods greater than 1 1/2 hours.

5.1.2 The Etalon

After the light is reflected into the instrument by the scanning mirror system, it enters the etalon. The 15-cm etalon used at Utah State comprises two plane parallel fused silica plates which have highly reflecting inner surfaces, with a reflectance of 0.90. These plates are held a fixed 20.49 mm apart using three zerodur spacers. Zerodur is a polycrystalline ceramic with a very low coefficient of thermal expansion of $0.2\text{-}0.4 \times 10^{-6} / \text{K}$ which keeps this distance very constant over time [Rees *et al.*, 1982; Killeen *et al.*, 1982]. The spacers can be individually adjusted to make the etalon plates as parallel as possible. Once set, the spacers maintain the gap with a high degree of thermal stability [Killeen *et al.*, 1982]. The inside surfaces are adjusted to be exactly parallel while the outside surfaces are slightly wedge-shaped to reduce the possibility of reflections off of these outer surfaces, causing false fringes to appear in the image.

The etalon is sealed in a container that can be evacuated and where temperature is carefully controlled and maintained at 28°C , approximately 5° above the ambient room temperature. This prevents changes in the etalon characteristics due to temperature fluctuations. The etalon chamber is sealed to be pressure tight to keep it free from dirt, and is slightly evacuated so as to adjust the radius of the fringes on the photocathode, as their position is a function of the index of refraction. The insides of the etalon plates are polished flat to a very small fraction of a wavelength ($\lambda/200$) and are coated with a dielectric semireflecting layer [Aruliah, 1992]. Inherent in the high reflectance of these inner surfaces is the assumption that the corresponding transmittance is low. This produces a transmission pattern composed of bright fringes on a dark background. Figure 20 shows the manufacturer's curve for the transmittance of our etalon.

This curve shows that the transmittance and hence the reflectance of the etalon surface are a function of the wavelength of the incident light. It also shows that the etalon coating was carefully chosen based upon the intended application and the

wavelength range to be measured by the instrument. The reflectance at 8430 Å is approximately 90%, only slightly better than the reflectance at 6300 Å.

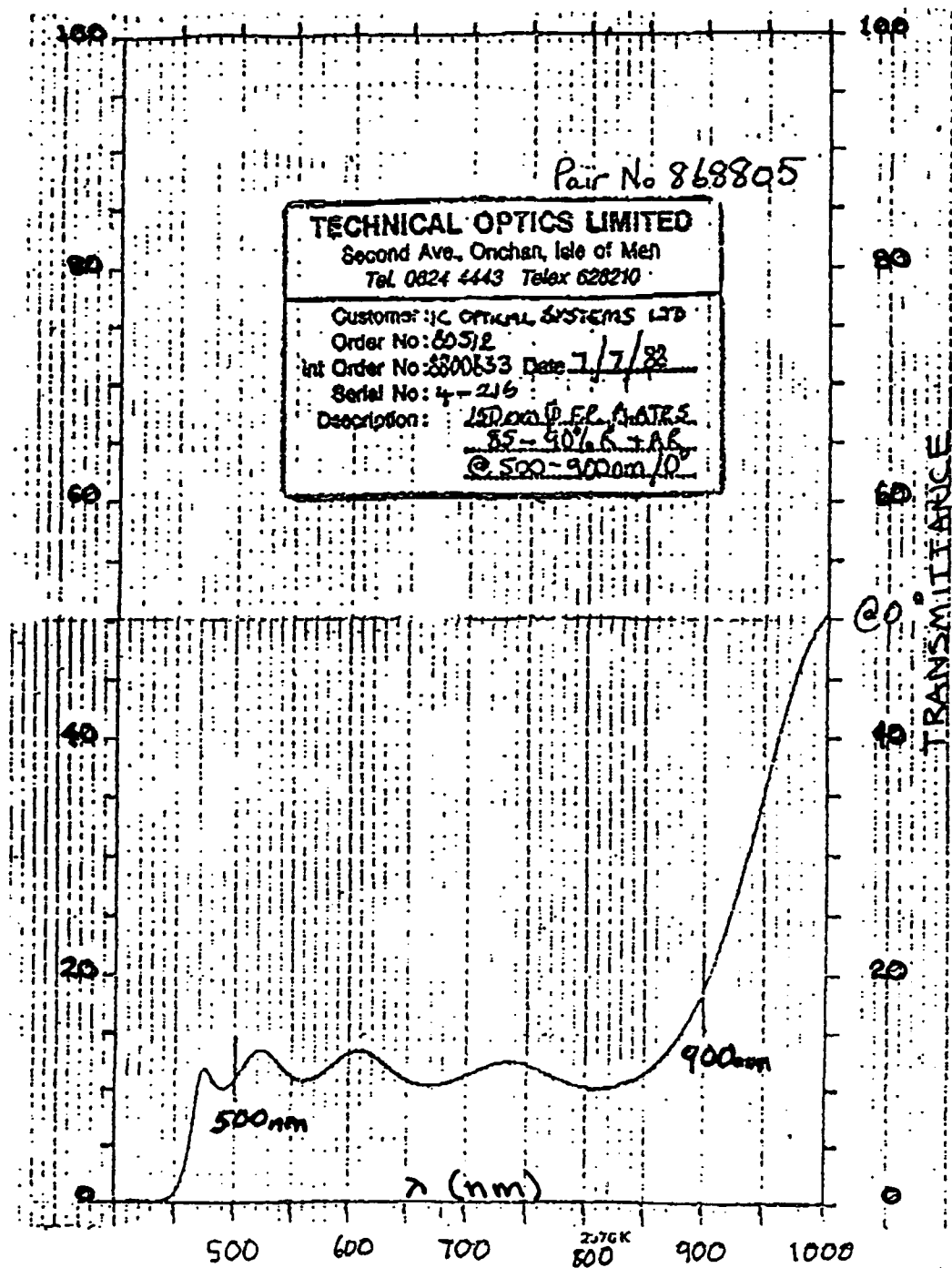


Fig. 20. Transmittance curve for the etalon plate coating.

It is important that the materials used to coat the etalon plates are not highly absorbing as this will reduce the amount of light that is transmitted. This is why dielectric coatings have replaced the metallic coatings which were used prior to the 1950s.

One feature that makes this Fabry-Perot somewhat special is its overall ruggedness. This etalon was originally designed to be used on rockets and satellites and is therefore extremely rigid and stable, resulting in an instrument that is very constant over time [Rees *et al.*, 1982; Killeen *et al.*, 1982]. The use of a 4-rail optical bench to hold the negative lens, filter wheel, and detector continues the rugged design to the rest of the IFPI.

5.1.3 The Lens System

Two separate lenses are used to direct the light emerging from the etalon to the detector (Figure 19). Directly below the etalon is the primary lens. This is a convex lens which brings the individual light beams to a focus, causing them to interfere. The second lens, a negative Barlow lens, is located prior to the interference filter. It has two basic functions. First it spreads out the light going to the detector to make it approximately parallel before it enters the filter (Figure 21). This is important because the shape and location of the passband of the interference filter is dependent on the angle at which light strikes it. To get the maximum possible signal through the filter, light must strike it at nearly normal incidence.

The second function of the Barlow lens is to allow the instrument a longer effective focal length than the physical size of the instrument would suggest. This provides versatility to the instrument. The lens can be adjusted so as to obtain a good focus on the detector and to control the size of the image on the photocathode. The focal lengths of the two lenses are 77.5 cm and -27.5 cm, respectively. The effective focal length of the system is 1.58 meters.

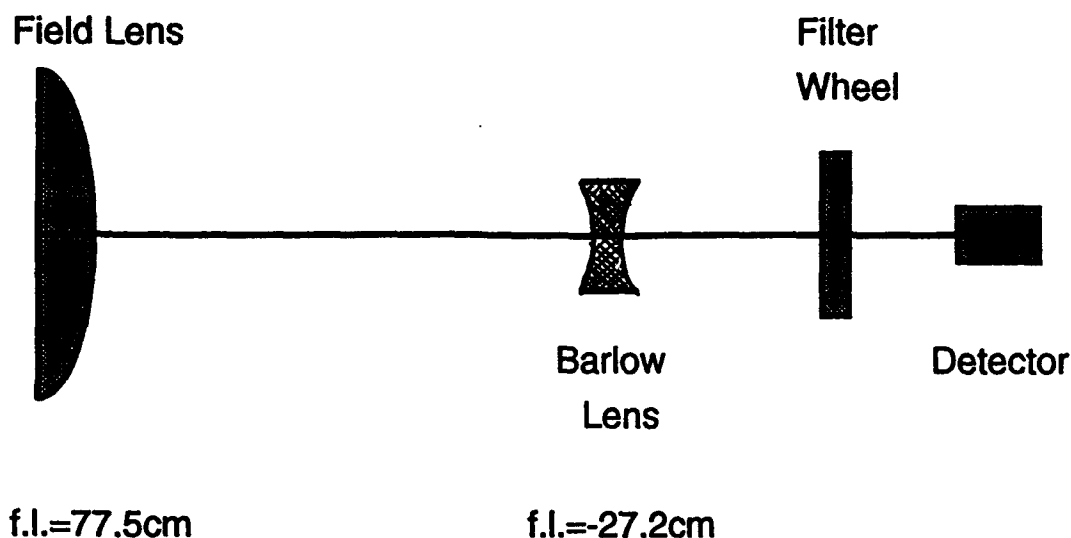


Fig. 21. The Fabry-Perot lens system and focal lengths.

5.1.3.1 Effective Focal Length and f-Number

A major advantage of using a Fabry-Perot interferometer is that its luminosity, or light-gathering ability, is much greater than that of other instruments with similar resolution [Hernandez, 1986]. This is because of its large aperture (15 cm).

The primary and secondary lenses are set within the instrument cavity such that the *effective* focal length of the instrument is approximately 150 cm. A figure of merit used for optical systems is f-number. It is found by Equation 5.1.

$$f\text{-number} = \frac{f}{D} \quad (5.1)$$

In this equation, f is the effective focal length, and D is the diameter of the collecting aperture. This gives an f-number of 10 for our instrument, which is fairly high. A large f-number minimizes the spectral distortion of the light passing through the interference filter.

5.1.3.2 Field of View (FOV)

The FOV of the instrument at Bear Lake can be calculated using simple geometry. The effective focal length of the instrument is approximately 150 cm, and the diameter of the detector is 25 mm. Taking $\tan^{-1}(12.5\text{mm}/150\text{cm})$ to get the half angle, the full FOV angle is $\theta = 0.9549^\circ$, which can be approximated as 1° .

The instrument is set up such that it scans 360° in azimuth at a 30° elevation angle. At an altitude of 86 km where the OH emissions are measured, a 1° FOV will mean that the area from which emissions can enter the FOV will be a circular area less than 2 km in diameter. In contrast, as the instrument makes measurements around the 360° viewing circle at 86 km, the area of the sky that is sampled is an area nearly 300 km in diameter.

5.1.4 The Imaging Photon Detector

The images formed by the lens are collected by an electronic photon counting device called an Imaging Photon Detector (IPD). The IPD is model F4146 from ITT. The IPD used for observing nightglow at the Bear Lake Observatory has a Gallium Arsenide (GaAs) photocathode with a useful sensitivity extending beyond 8500 Å [Rees *et al.*, 1990]. The spectral response curve provided by ITT for our detector is shown in Figure 22.

The quantum efficiency at 8430 Å is approximately 18% and at 6300 Å is approximately 9%. This is extremely good compared to other detectors such as the S-20 and S-25 (extended red response), which typically have quantum efficiencies less than 1% at 8430 Å.

The photocathode is circular with a 25-mm diameter. It is mounted on top of three z-configuration micro-channel plate intensifiers which consecutively multiply (stimulate) the cascade of electrons moving toward the four-terminal resistive anode [Rees *et al.*, 1980]. After amplification and pulse shaping these signals are sent to the signal processing unit where they are combined to determine the x-y position on the

ITT ELECTRO-OPTICAL PRODUCTS DIVISION
 3700 E. Pontiac St., Fort Wayne, Ind. 46803. Telephone (219) 423-4341

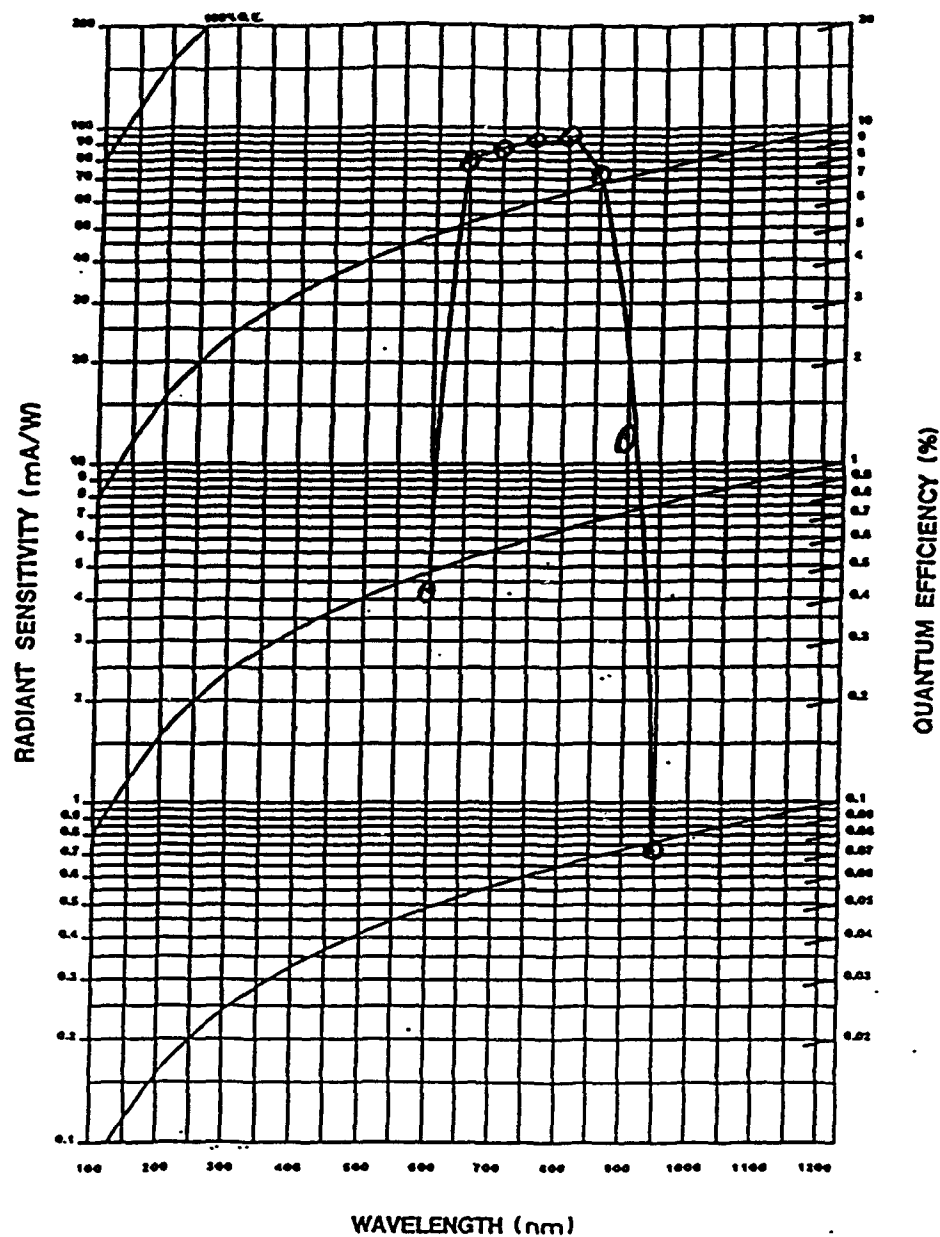


Fig. 22. Spectral response curve for the Bear Lake Observatory detector.

photocathode. The location of incidence of the original photon is equated with the centroid of the final cascade, which can be calculated to within $\pm 13 \mu\text{m}$ [Aruliah, 1992]. The photon position is then digitized and sent to a board in the PC and thence to the computer memory where the complete two-dimensional image is built through the integration period.

The maximum count rate that can be handled by the system, the IPD, and the electronics is 200,000 counts per second. The integration time is limited by the use of 16-bit integers in the software to 32,768 counts per bin.

Although a two-dimensional image of the fringe pattern is accumulated in the computer memory, it is too big—2 bytes per pixel and 65,512 pixels—to be stored for every integration period for a whole night. Instead a circular integration, as described earlier, is performed to make a one-dimensional image consisting of 2 bytes per bin and 256 bins.

The detector is cooled to -30°C with a combination of a Peltier cooler and a constant-temperature water-antifreeze circulator to reduce the thermionic emission from the photocathode. Thermionic emissions, or dark counts, are due to electrons leaving the photocathode. While cooling reduces the rate of emission, it can never be totally eliminated. The effect can be estimated and removed in data processing. The thermionic emission is measured by completely blocking any light coming into the instrument and performing a long integration, such as for an hour. The thermionic emission of the entire device (256 X 256 pixels) at -25°C is approximately 422 counts per second, or 0.006 counts per second per pixel, or 1.7 counts per bin.

Another aspect of the IPD, indeed the whole system, is nonuniform sensitivity of the photocathode to light. It is necessary to make a measurement of how each pixel comparatively responds to a uniform source of illumination. This is called a "flat field"

measurement. (It becomes more important as the IPD deteriorates over years of use and exposure to high light levels).

For this measurement, a weak, diffuse, white light (a flashlight through several layers of frosted glass) is used to uniformly illuminate the IPD.

For both the thermionic emission and flat field measurements we opt to use the longest feasible integration time to reduce the uncertainty in the measurements. Before the data processing, both of these are normalized to a 1 second integration and stored as such.

There is some debate as to exactly when these corrections should be made to the data. Actually there is no controversy about what should be done ideally, but there are practical considerations. Ideally, one would like to use the full two-dimensional image (65,512 individual pixels) and correct each image pixel for its own nonuniformity and dark count before reducing the image to a one-dimensional profile and storing it. But because some of the Fabry-Perot sites, which use the same data collection software as we do, run unattended for many months, a problem in the system would not be detected immediately, and the original data could never be recovered if the "incorrect" corrections were applied prior to integration. The group at UCL studied this problem and determined that the error resulting from applying this correction to the integrated data rather than the two-dimensional image is small. So this is the procedure that is followed. Inherent in this procedure is the necessity to redo the reduction of the two-dimensional flat field and thermionic emission images, or make new measurements whenever the center coordinates are changed for the data image reduction. If this is not done, the correction will not be appropriate for the reduced image and a systematic error will result. It is also important in the data processing to use the most recent flat field and thermionic emission files for the data being analyzed to get the true detector characteristics for the given period.

The airglow observations are stored in terms of counts per second in each bin. The correction for thermionic emission is accomplished by subtraction. The correction for nonuniformity, the flat field correction, is more involved. The thermionic emission count is subtracted from the flat field count for each bin to arrive at the pure flat field count. At the same time, the flat field is normalized to the value of bin 9, according to the following algorithm

for i = 1 to 256 (bins)

$$\text{flat field correction}(i) = \frac{\text{flat field}(9) - \text{thermionic emission}(9)}{\text{flat field}(i) - \text{thermionic emission}(i)}$$

The selection of bin #9 is arbitrary. The most recent thermionic emission and flat field measurements are shown in Figure 23, parts (a) and (b). These were done on 26 January 1992 using a 120 second integration time to obtain the flat field and a 1-hour integration time to obtain the thermionic emission. An uncorrected one-dimensional spectrum is shown in parts(c) and the corrected spectrum in part (d).

One thing to note in looking at Figure 23 is the sharp drop in detector sensitivity near the outside edge of the detector, which is evidenced by the dramatic drop-off in counts beyond about bin 200 in the thermionic emission, flat field, and uncorrected data. This results in a large correction being applied to the data between bins 200 and 256. The corrections give rise to a uniform, or flat, background out to bin 200. Beyond that, the flat field overcorrects. (Apparently the intensity of the flat field light source fell off near the edges because the detector area was not uniformly illuminated.) The resultant false peak has no effect on the subsequent data analysis.

Because the detector sensitivity changes with wavelength, it is necessary to make separate flat field measurements for each wavelength that will be observed. Also, the detector sensitivity and emission will change over time so that both of these measurements need to be redone every few months under normal circumstances for each wavelength. If the operating temperature is changed, a new thermionic emission

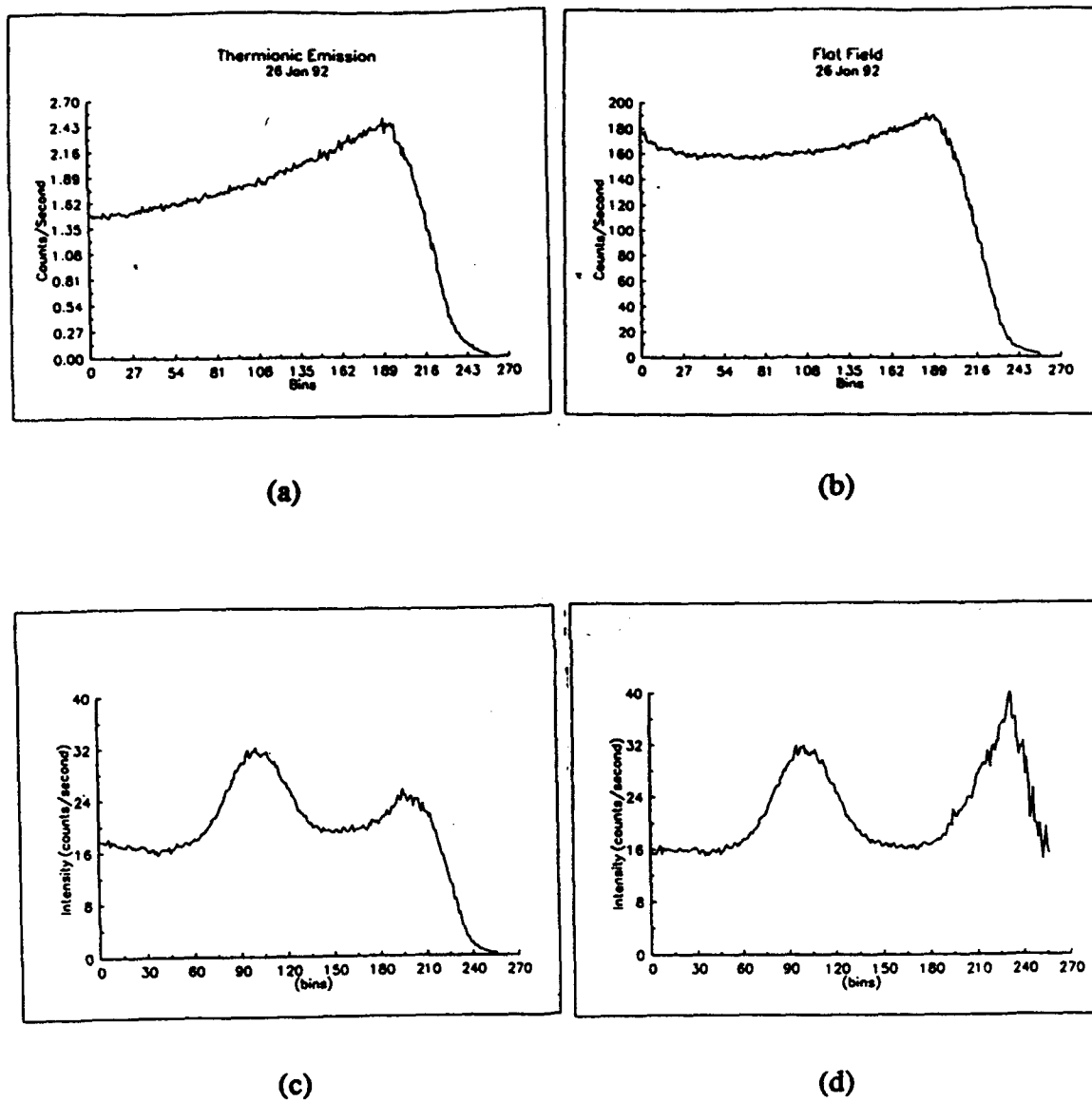


Fig. 23. (a): Thermionic emission calibration, (b): Flat Field calibration at 8430 Å, (c): Uncorrected one-dimensional OH spectrum, and (d): Corrected spectrum.

calibration will also be needed. And, if there are rapid changes in detector sensitivity, these measurements should be made more often.

5.1.5 The Calibration Sources

The calibration sources have two primary purposes. First, because they are sampled regularly during the observing cycle, they serve as an indication of the stability of the instrument and provide a way to remove the effects of instrumental drift from the calculated wind speeds.

Secondly, they serve as an indicator of the overall health of the system. Any change in the appearance of the calibration fringe should be taken as an indication of a physical change in the system and cause some concern. One way to monitor this is simply to record the position of the calibration lamp peaks, as well as their intensity and background, over a long period of time. If a pressure leak develops within the etalon chamber or the etalon heating fails, the peak locations will change. If the IPD cooling fails, the background will increase.

Two RF-excited calibration sources are available for use depending on the wavelength of the emission being collected. The gas in one calibration source is neon, and in the other it is a helium-neon-krypton mixture. These sources rely on cosmic rays to establish the ionization path. Figure 24 shows the calibration lamp fringe overlaid on an 8430 Å OH fringe. The peaks of the two fringe patterns are offset because the calibration lamp is at a slightly different wavelength than the OH emission at 8430 Å. Note that some OH emission is also present in the calibration measurement—the "bump" on the left of the calibration peak.

5.1.6 Interference Filters and Filter Wheel System

Prior to November 1991, a single interference filter was inserted into the instrument and only one emission could be studied at a time. Since then the instrument has been modified to accommodate a filter wheel system that allows up to five different

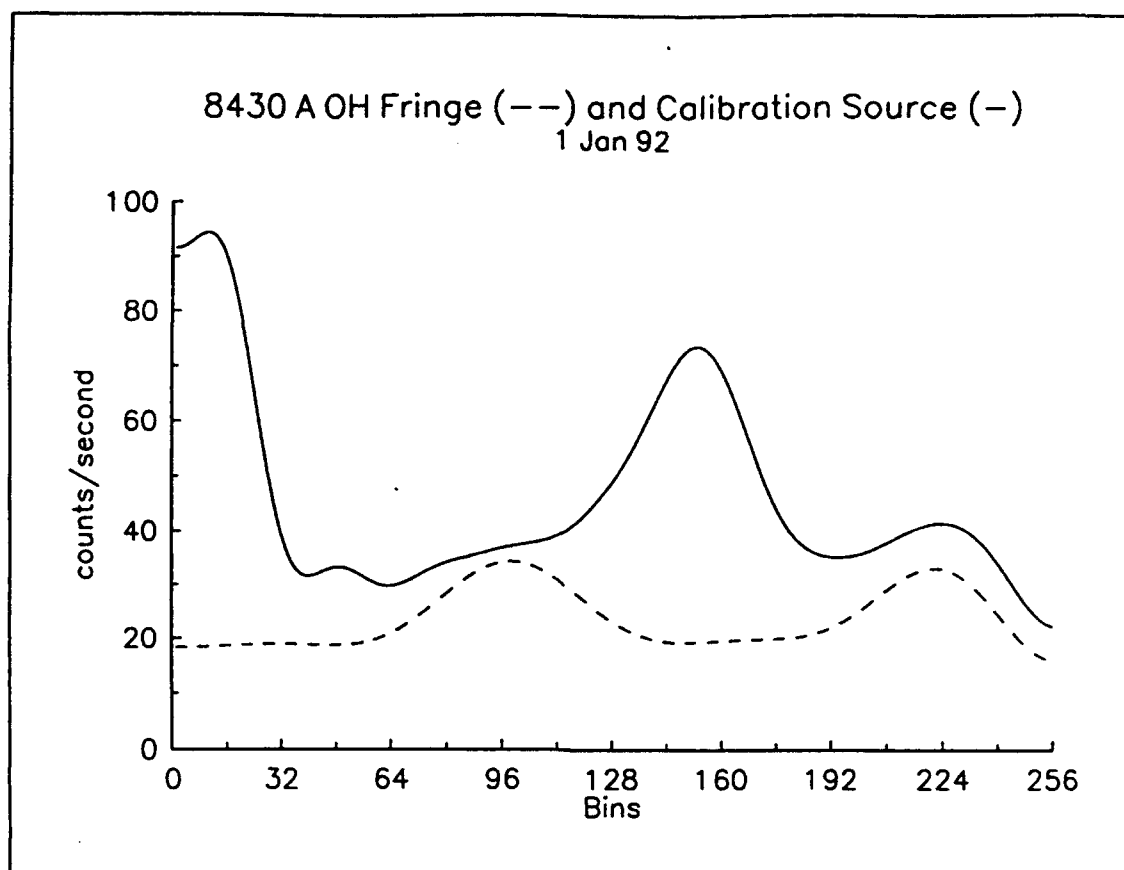


Fig. 24. Calibration lamp and OH 8430 Å fringe.

emissions to be observed during the mirror sequence. This will greatly enhance the variety of comparisons that can be made in future studies. The central wavelength and passbands (full-width half-max power) of the five filters installed at Bear Lake are shown in Table 9.

The use of multilayer coatings allows filters to be built to very precise spectral specifications. Two factors which are important to filter performance are temperature and angle of incidence. The bandpass decreases as the filter is cooled, but this has a negligible effect in our application because the temperature in the Fabry-Perot room is maintained constant to within 2°C.

TABLE 9. Filter Center Wavelength and Full-Width at Half-Maximum Power

Filter Number	Center Wavelength (Å)	Full-Width Half-Max (Å)
1	6302	5
2	8432	10
3	7774	10
4	8669	10
5	6328	30

The dependence of effective bandpass on angle of incidence is given in Equation 5.2.

$$\lambda_1 = \lambda_0 \left(1 - \frac{\sin^2 \theta}{n_{\text{eff}}^2}\right)^{1/2} \quad (5.2)$$

where λ_1 is the resulting central wavelength, λ_0 is the central wavelength at normal incidence, θ is the angle of incidence, and n_{eff} is the effective index of refraction of the filter. The shift varies roughly as the square of the angle of incidence: for 15° angles this would be about 1/4 of the values for 30° . For example, wavelengths would be shorter by 1-2% for 30° angle of incidence.

As mentioned previously, we have attempted to minimize this effect through the use of the negative Barlow lens prior to the filter, which keeps the angles of incidence on the filter nearly normal.

The interference filter is selected to isolate the particular emission of interest from the normal nightglow spectrum. Because there are many individual emission lines in every spectral interval, it is necessary to use a very narrow filter with sharp cutoffs to separate one individual line from the herd. If the passband of the filter is too wide, extraneous emissions will be able to pass through to the detector, contaminating the data. To measure the 8430 Å emission line, a 2" diameter, 5 Å half-width interference filter peaked at 8432 Å for normal incidence is selected to isolate the 8430 Å line. The filter is chosen such that the center wavelength is slightly redder (longer in wavelength) than the

emission of interest so that the center wavelength will be 8430 Å for the cone of light incident on the filter and because the peak of the filter will normally drift toward the shorter wavelengths with age.

Auroral contamination occurred in the Bear Lake data prior to September 1990 when a 25-Å wide filter was used instead of the current 10-Å filter. The contamination significantly distorted and widened the primary fringe, spoiling its usefulness for determining Doppler shift and Doppler width. This secondary emission was identified in the UCL analysis as most probably 8446 Å atomic oxygen emission [Aruliah, 1992], which has been eliminated by the use of the narrower filter.

The transmittance curve for the 8432 Å filter is shown in Figure 25. The amount of incident light transmitted at normal incidence is approximately 50%. At 2.9° angle of incidence (the maximum angle for an f10 system), the transmission drops several percent and the center wavelength is blue-shifted to 8429 Å.

An ideal filter would have perfectly square cutoffs at the upper and lower wavelengths, however the actual response falls off more gradually. This filter uses three cavities to make it as square as possible while maintaining peak transmittance. At shorter wavelengths the transmittance is reduced by five orders of magnitude; at longer wavelengths by four orders of magnitude. Extra blocking on the long wavelength side is not needed because of the fall off in IPD sensitivity.

5.1.7 The He-Ne Laser

The laser selected to measure the instrument profile of the Fabry-Perot is a single-mode stabilized He-Ne laser at 6328 Å. The laser light needs to pass through several layers of frosted glass to obtain a uniform source, as for the flat field calibration. These calibrations are essential when reducing the data for temperatures.

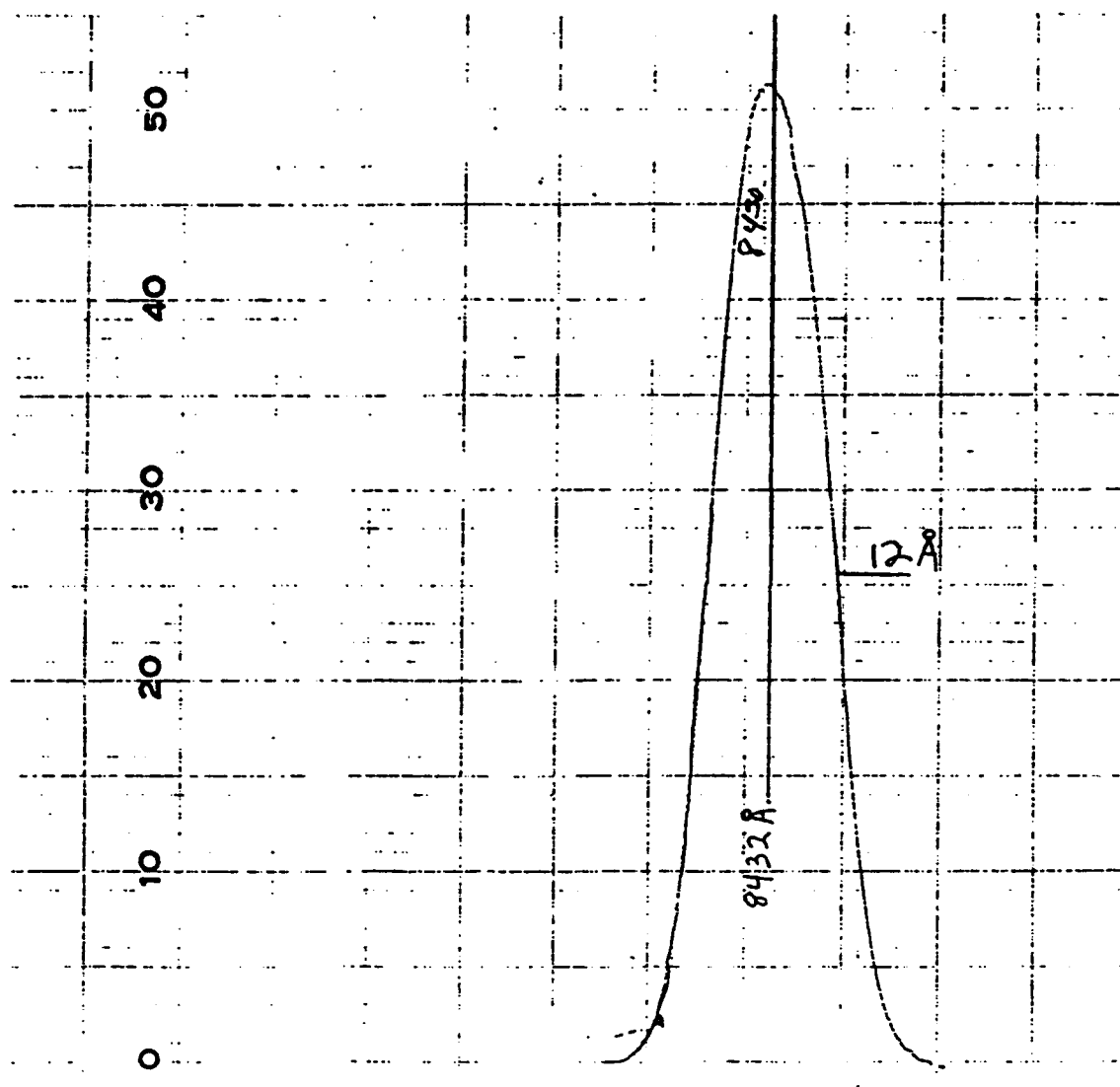


Fig. 25. Manufacturer's transmittance curve for the 8432 Å filter for normal incidence.

5.1.8 Temperature Control and Instrument Stability

Controlling the temperature of particular instrument parts is critical to obtaining consistent measurements. To prevent changes in the etalon characteristics due to changes in room temperature, the etalon is heated to 28°C, approximately 5°C above the ambient room temperature and maintained to within $\pm 0.1^\circ\text{C}$. The temperature setting can be adjusted if necessary to adapt to increases in the ambient air temperature.

The detector requires cooling to minimize the thermionic emission. A temperature of -30°C is chosen to achieve this. A Peltier cooler is incorporated in the IPD housing for the first stage of the cooling. A constant temperature circulating system then pumps a 50/50 water-antifreeze mixture at 0°C through pipes in the IPD housing to cool the Peltier.

Additionally, to keep the Plexiglas dome free of snow, ice, and condensation, and to maintain the temperature of the components within the dome at a steady temperature, a fan system is used to circulate air from the room up into the dome area. A combination of heating and air conditioning is used to keep the ambient temperature stable.

5.1.9 The Computer and Software

Software from UCL called HALO provides the data acquisition, timing, display, processing, and storage capability for the Fabry-Perot using an ordinary PC. The PC and electronics are located outside the blackened room in the adjacent work area (Figure 18). The instrument can be run unattended using preselected sequence files in HALO, or can be operated manually by specifying what is desired for each image individually. A modem connected to the data acquisition computer allows remote computer control and access to data from Utah State University as well as a means to periodically check the health of the system without making a trip to the observatory.

4.1.9.1 Starting, Stopping, and Detector Preservation

The routine job of turning the system on after dark and off again before sunrise is performed by HALO, which consults a built-in almanac to determine the current positions of the sun and the moon. If the sun is found to be at least 8° below the geometric horizon and the moon is not in the present viewing sector, HALO prompts the instrument to collect an image.

Several safety mechanisms are included in the system design to prevent accidental exposure of the sensitive detector to a bright source. The primary measure is a check which is done continuously by HALO whenever the high voltage to the detector is turned on. If HALO detects a photon count rate above 200,000 counts per second, the high voltage to the detector is automatically shut off. HALO tries again three times before shutting off for 20 minutes and performing the check again. This is intended to prevent an unexpected light source, such as a flashlight, from overloading the detector.

There are several other backup safety features which are currently in place. A photocell mounted in the dome detects light above a certain threshold intensity and automatically cuts power to the detector when the intensity exceeds that threshold. This would be invoked if for some reason HALO had failed to shut the system off and it were still running at daybreak and the sun had begun to rise.

Finally, a clock timer with a battery backup is adjusted to automatically shut off power to the detector between sunrise and sunset. This timer must be adjusted manually as the times of sunrise and sunset change with the seasons. Using the combination of these three mechanisms there is little chance of inadvertently damaging the detector.

5.2 List of Instrument Parameters

The following is a list of instrument parameters for the Bear Lake instrument.

1. Instrument Parameters

effective focal length (f) = 150 cm
f-number \approx 10
aperture diameter = 15 cm
effective finesse \approx 3.5 for OH 8430 Å (instrument width not removed)
effective finesse \approx 2.2 for OI 6300 Å (instrument width not removed)
FOV angle \approx 1°

2. The Etalon

plate separation = 20.49 mm
reflectance = 0.90 at 8430 Å; 0.88 at 6300 Å
reflective coating = ZnS and MgF₂ [Aruliah, 1992]

3. Interference Filter

diameter = 2 inches
half width = 5 Å (full width at half maximum = 10 Å)
peak transmission at 0° incidence \approx 50%
peak wavelength = 8432 Å (normal incidence)

4. Photomultiplier

quantum efficiency = 18 % at 8430 Å; 9% at 6300 Å.
dark count = 422 counts/second at -30° C
= 1.7 counts/second/bin
= 0.006 counts/second/pixel
detector size = 25 mm diameter

5. Resolving Power

8430 Å : 1,400,000 Wavelength Resolution \approx 5.87 mÅ
6300 Å : 1,900,000 Wavelength Resolution \approx 3.28 mÅ

6. Free Spectral Range

8430 Å : 148 bins = 173.41 mÅ

6300 Å : 110 bins = 96.85 mÅ

CHAPTER 6

THE QUEST FOR WIND VELOCITIES

Determining winds from the Doppler shift of airglow emissions presents two major challenges. The first involves how accurately the position of the peaks on the spectra can be determined, and the other is related to how well we can establish the zero velocity position of the peak from which to measure the relative Doppler shifts. These questions are addressed in the following sections which discuss the techniques used in the data processing.

6.1 Data Processing

6.1.1 Fourier Analysis

Because HALO automatically reduces and stores the Fabry-Perot images in their one-dimensional form, the analysis begins with these. The one-dimensional fringe profiles exhibit a noise inherent in the signal due to the statistical fluctuations of the emission from the IPD photocathode. This is illustrated in Figure 26, which shows two raw interferograms, one OH 8430 Å and one OI 6300 Å. The integration times were 4 minutes. Although I have referred to these as the "raw" interferograms, the flat field and thermionic emission corrections have already been applied.

Because the photocathode noise appears at a much higher spatial frequency than the emission line profile, it can be removed by low-pass filtering the data to eliminate frequencies which do not directly contribute to the source profile. This is accomplished using a fast Fourier transform (FFT).

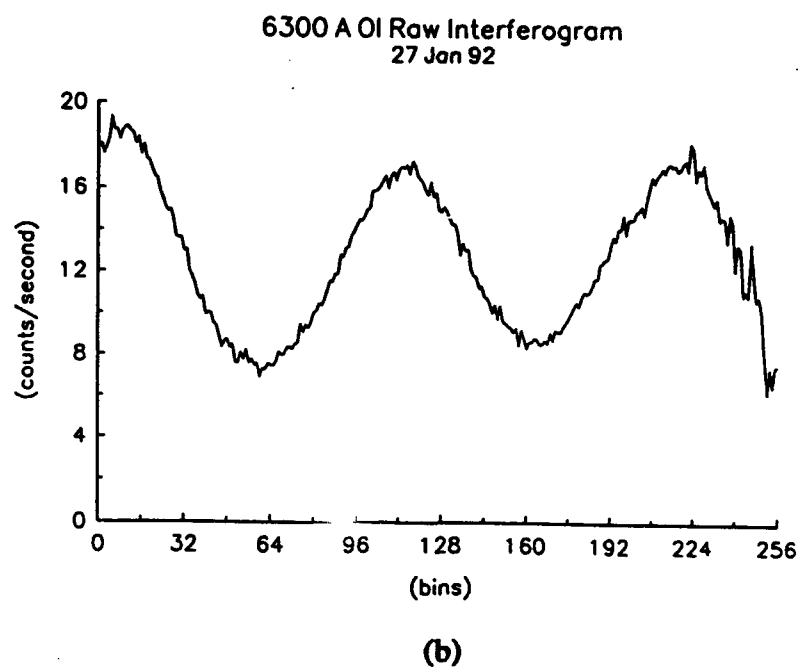
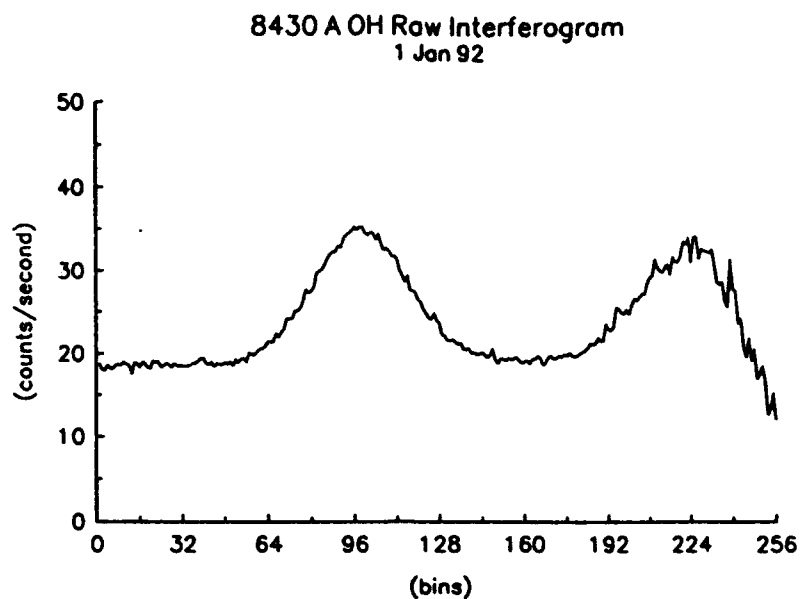


Fig. 26. Raw fringe profiles. (a) 8430 Å (b) 6300 Å.

The Fourier transform of the raw data is taken to obtain the weight of each of the frequency components present in the signal. Then a Hamming filter is used to limit the number of frequency components sent back through the reverse transform. The Hamming filter function is constructed using the following set of equations where the array $a(n)$ becomes the multiplication factor for the Fourier coefficient array. N_{cut} is the number of whole frequency components to be kept. Beyond N_{cut} the function has a 20% taper down to zero. After this "window" is multiplied by the coefficient array, the inverse transform is taken to obtain the smoothed function.

$$\begin{aligned}
 a(n) &= 1 & N &= 1, N_{\text{cut}} \\
 a(n) &= 0.5 \cos \frac{\pi(N - N_{\text{cut}})}{2(\text{int}(0.5 + 0.2N_{\text{cut}}))} & N &= N_{\text{cut}}, N_{\text{cut}} + 2(0.5 + 0.2N_{\text{cut}}) \\
 a(n) &= 0 & N &= N_{\text{cut}} + 2(0.5 + 0.2N_{\text{cut}}), 256
 \end{aligned}$$

It is important to use a cutoff function, or window, which does not abruptly eliminate all frequency components beyond a particular cutoff, but instead, tapers off gradually to zero. If the number of frequency components is cut off bluntly, the point at which the cut is made will appear in the Fourier transform routine as a discontinuity in the function that is being fit. This introduces a high frequency noise into the signal because at the point of apparent discontinuity the fit overshoots the actual data and creates ripples in the smoothed profile. This phenomenon, known as Gibb's phenomenon, and its presence would make the next step, determining the position of the peaks accurately using the slope of the curve, infinitely more difficult.

Two examples of the smoothed fringe profile obtained by Fourier methods are shown in Figure 27.

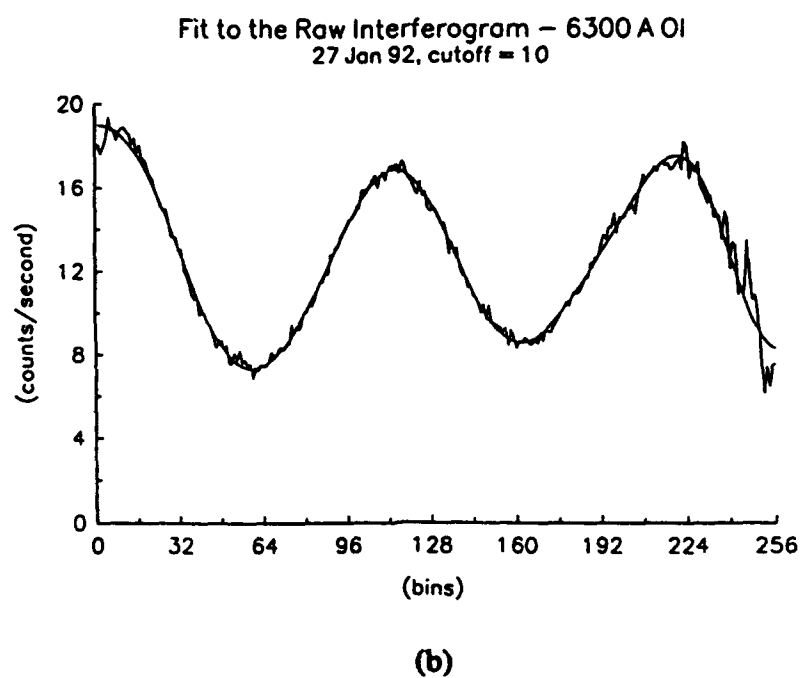
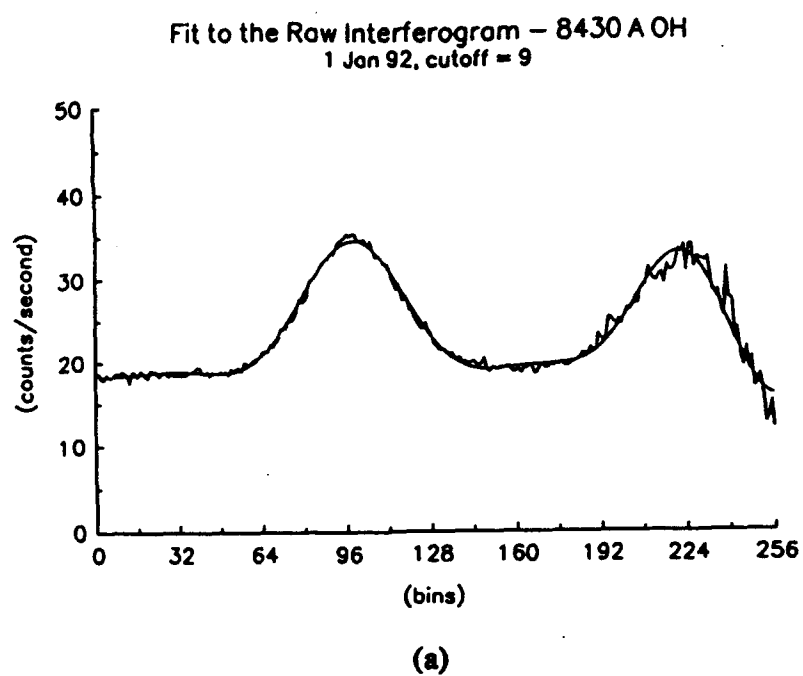


Fig. 27. Fourier smoothing of the raw data. (a) 8430 Å, (b) 6300 Å.

The fact that the smooth curve seems to fit the original data very well is no accident! The best possible fit for the data was found by experimenting with the cutoff frequency used in the filter function. To determine the optimal cutoff frequency for the Fabry-Perot data, several methods were employed. The first was simply to look at the fit obtained using different cutoffs, and visually define the best fit. To supplement this, a chi-square value was calculated comparing the fit of the raw data to the smoothed profile to determine the "goodness" of the fit for each selected cutoff using Equation 6.1.

$$\chi^2 = \sum_i \frac{(y_i - y(x_i))^2}{\sigma_i^2} \quad (6.1)$$

In this equation σ_i^2 is the variance on each point. It is desirable for chi-square to be a small number, with a value of around 2, giving a good fit to the Fabry-Perot data. A single cutoff does not produce the best fit for all measured emissions, however, because the intensity, and thus the sharpness of the emission peak, varies from emission to emission. Because the calibration sources have a high intensity compared to the nightglow emissions, they require higher cutoff frequencies than the corresponding airglow data.

The second method used to identify the optimum cutoff frequencies involved plotting the power spectral density (PSD) for individual fringes to see where the power of the signal was concentrated. This resulted in plots such as the one shown in Figure 28, which shows a representative PSD plot for 8430 Å OH data.

The third and final method examined the stability of the peak position found by the analysis routine as the cutoff frequency was varied. This analysis showed that there are well-defined lower and upper boundaries to the stability of the peak position. This result is reasonable because at very low cutoff frequencies the smoothed data are not representative of the actual data and therefore the peak found by the routine will be influenced greatly by the addition of each successive frequency term. At high

frequencies, the upper level of stability is defined by where the routine begins to fit the noise in the signal rather than the emission peak. Above this upper boundary, this also results in a peak position that changes significantly with the addition of consecutive frequency terms. Figure 29 shows several examples of how the determined peak position is only stable over a particular segment of cutoff frequency. This procedure allowed us to define the boundaries for an appropriate choice of cutoff frequency.

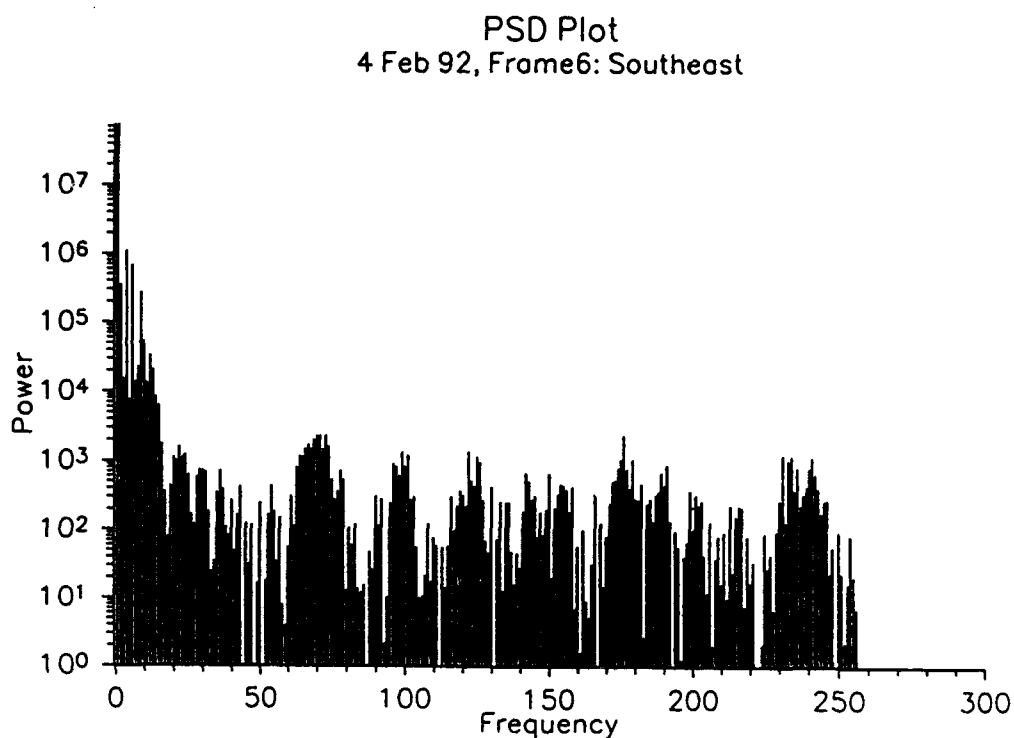


Fig. 28. Power Spectral Density for 8430 Å OH. The zero frequency component was omitted to allow a better scale.

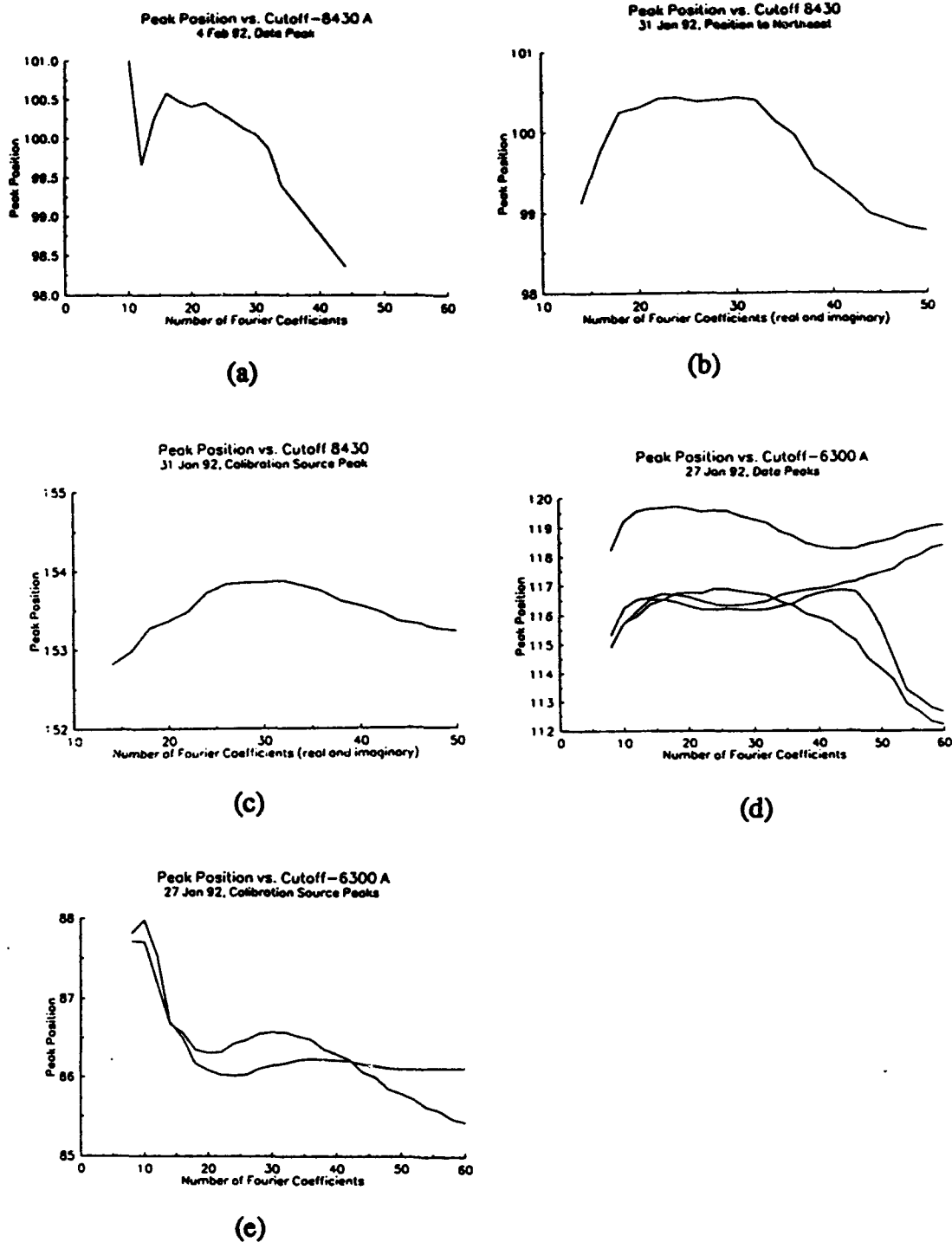


Fig. 29. The range of stability for the calculated peak position as a function of cutoff frequency. The numbers along the bottom axis of these plots are the total number of frequency components, real and imaginary. (a) and (b): 8430 Å OH data, (c): OH Calibration Source, (d): 6300 Å O(¹D) data, and (e): O(¹D) Calibration Source.

Based on the analysis described above, the final cutoff frequencies were chosen. These are given in Table 10 for 8430 Å and 6300 Å data, and their corresponding calibration source measurements. These numbers refer to the number of real components. Hence, they have the magnitude of the values in Figure 29, which include both the real and imaginary coefficient. These cutoffs result in smooth profiles representative of the data but not the noise.

TABLE 10. Number of Frequency Components Used

Emission	Data	Calibration Source	Old Calibration Source
8430 Å	9	14	16
6300 Å	12	15	

** Note: The reason there are two different calibration source cutoffs given for 8430 Å is because prior to August 1990, a different calibration source was used. This source displayed a double peak when viewed through the OH filter and thus it requires more frequency terms to get an adequate fit.

6.1.2 Peak Positions

Once the smoothed profile is obtained, the peak positions are found by differentiating the function to find where the maxima occur. The desired precision of the peak position was selected to be 0.05 bins. This translates into a wind speed error of approximately 1-2 m/s, and defines the maximum precision for any particular measurement. The formal name for the method used to find the maxima, i.e., the roots of the derivative, is the Newton-Raphson method.

The Newton-Raphson method basically says that if there is a function $f(x)$ with a derivative $df(x)/dx$ and this function has a root in the vicinity of a known value x_1 , then a more accurate root, x_2 , can be found using the equation

$$x_2 = x_1 - \frac{f(x_1)}{df(x_1)/dx} \quad (6.2)$$

The Newton-Raphson method evaluates the function and its first derivative at a selected value of x_1 and then uses the slope (derivative) to geometrically extend a tangent line at the current point x_1 until it crosses zero, i.e., until $f(x_2) = 0$. The next guess is selected as the abscissa of that zero crossing, x_2 . This method is used iteratively to get the precise root of the function. Algebraically the method is derived from the Taylor series expansion of a function in the neighborhood of a point, and is desirable over other methods because it converges quickly, usually requiring only three or four iterations to find the root.

To start the iteration in the analysis one must first give it a rough estimate of the position of the peak (x_1), which is accomplished simply by finding the particular bins which have a larger magnitude than the surrounding bins and using that as an input.

6.1.2.1 Error on the Position of the Peak

Because the position of the peak is established using the smooth curve instead of the original noisy data, the error in the peak position is directly related to how well the smooth curve actually represents the data. Since we have limited the number of frequency components in constructing the smooth curve, a measure of the uncertainty in the final position of the peak can be estimated by taking the average of the peak positions found while allowing the number of frequency components used to increase one at a time for some number of additional frequency components beyond the cutoff. In my analysis a new peak position is computed for an additional 20% of the frequency components beyond the selected cutoff. After computing these new peak positions, their average is taken. Although this is strictly a numerical result, it appears to give a reasonable approximation to the expected standard deviation of the peak position as well as an indication of the stability of the method. In particular, when the signal becomes smaller or the noise level bigger, the calculated error increases in the expected manner. Thus,

these values are assumed to represent the uncertainties to within a scale factor. That scale factor is derived in Section 6.2.3.

The uncertainties found using this method are typically in the range of 0.05 to 0.2 bins for the OH observations, which translate into a wind speed error of approximately 1 to 8 m/s.

6.1.2.2 First Moment Method-Peak Position and Error

Another method of finding the peak location is to perform a first moment calculation,

$$x_{peak} = \frac{\sum_{i=n_1}^{n_2} x_i N_i}{\sum_{i=n_1}^{n_2} N_i} \quad (6.3)$$

where the x_i are the bin numbers and the N_i are the corresponding count rates. Because there is usually more than one peak and the background level is varying, this method cannot be applied profitably or blindly to all 256 bins. Instead it can be applied to a range of bins (n_1 to n_2) approximately centered on the peak. On several examples tested, the method produced a good peak position. More important than finding the peak position, this approach enables the uncertainty in x_{peak} to be determined from the uncertainty in the count rates, $\sigma_i = \sqrt{N_i}$. In a straightforward calculation, the variance of x_{peak} is found to be

$$\sigma_{x_{peak}}^2 = \frac{\sum_{i=n_1}^{n_2} [x_i - x_{peak}]^2 N_i}{[\sum_{i=n_1}^{n_2} N_i]^2} \quad (6.4)$$

This equation can be used when x_{peak} is located at the origin and the signal is much, much greater than the background. The full equation has been applied to several

OH peaks, both the raw data and the smoothed Fourier fits. The same results were found, i.e., uncertainties were significantly larger than those found by the Fourier cutoff method. This suggests that those found by the Fourier cutoff method may need to be scaled upward. I will return to this point and find a scaling factor after determining the zero-velocity position.

6.1.3 Peak Height

After the position of the peak is found, the height of the peak at that position is determined again using the Fourier coefficients in the frequency domain. The cosine series function they represent is evaluated at the calculated peak position to get the peak magnitude.

6.1.3.1 Error on the Magnitude of the Peak

The uncertainty in the magnitude of the peak is found in the same way as that used to find the uncertainty of its position. The cutoff frequency is changed, allowing additional frequency terms to be used in the determination of the height of the peak. The average of these is taken to get a numerical measure of the standard deviation in the peak height. This uncertainty can be applied to the relative intensity calculation.

6.2 Wind Determination

Line-of-sight velocities are derived from the Doppler shift of the emission peak in each of 8 azimuthal directions plus the zenith measurement. The assumptions made in obtaining the winds from these measurements are given below:

1. The height of the emission layer is assumed to be constant.
2. A uniform horizontal wind field exists, on average.
3. The vertical winds are small compared to the horizontal winds, and nearly zero.
4. The wind field changes smoothly in time (no discontinuities).

6.2.1 Determining the Zero Doppler Shift—Position/Baseline

For monochromatic radiation of wavelength λ , molecules moving toward an observer with some velocity v along the line of sight will appear to emit a wavelength shorter (blue shift, $\lambda - \Delta\lambda$) than the actual, where

$$\Delta\lambda = \lambda \frac{v}{c} \quad (6.5)$$

and c is the speed of light. Conversely, molecules moving away from the observer with the same velocity will appear to have a wavelength longer (red shift, $\lambda + \Delta\lambda$) than the actual wavelength. It is this "Doppler effect" which allows us to calculate the winds based on a measured shift in wavelength.

A shift in the radial position of the fringe on the interferogram corresponds directly to the Doppler shift of the emission and hence the wind speed at the altitude of the emission. In the observed Fabry-Perot fringe profile, a red shift moves the peak closer to the center of the image whereas a blue shift moves the peak radially outward. Since this shift is only a relative measurement of the wind, it is necessary to determine the position of the fringe that represents zero velocity. Once this is accomplished, the wind speed is calculated from the relative movements of the peaks with respect to this zero.

The peak position of a stable calibration lamp will vary during the night and over longer periods of time as the FPI drifts within a distance of approximately half of a bin. This may occur because of temperature or pressure changes in the etalon cavity. Hence measurements of the peak position are essential for tracking system performance. Furthermore, if a laboratory source at 8430 Å were available, it would be possible to find the true zero velocity position of the 8430 Å emission peak. However, because the calibration source used is at a different wavelength than the emission, the zero wind position it represents is offset by some constant amount from the zero wind position of an 8430 Å emission. The first step is to find this offset. It can then be applied to the

calibration lamp peak position to arrive at the zero velocity positions for emissions at 8430 Å.

To find the offset, a uniform wind field is assumed, on average, and the zero Doppler shift position for the airglow emission is estimated using the long-term average of the mean peak position for opposite pairs of measurements (N-S, E-W, NE-SW, SE-NW). These are also averaged with the zenith peak position which we assume to be at nearly zero velocity. The individual estimates of the zero are then subtracted from the corresponding calibration peak position to find the offset. They are averaged for a whole night. These calculations are performed with full error propagation. If these offsets from individual days are averaged for many days, an even better estimate of the true offset can be found. This is then applied to the calibration-peak-curve to give the zero velocity positions for each day.

This overtly simple procedure is complicated by the fact that we do not make measurements in all of the directions simultaneously. Because one complete observing cycle takes approximately 42 minutes, the measurements taken in opposite viewing directions are not taken concurrently and thus cannot be directly compared. A further complication arises when measurements are missing in some of the viewing directions during the observing period. This is usually due to the presence of the moon in that direction.

To account for the time differences and to help fill in missing measurements, the peak positions in each direction are linearly interpolated to the times of the calibration lamp measurements throughout the observing period. This is done only when the total time between measurements in a given direction is less than two hours. The error associated with this procedure is assumed to be small because the peak positions do not vary rapidly and it is fairly reasonable to assume that the corresponding winds will vary

linearly over short intervals of time. The errors calculated for each peak position are also propagated to the time of the calibration measurement.

Once the interpolation is done, the mean peak position for opposite pairs of measurements is averaged with the zenith measurement as described above. For example, if you had measurements to the north, northeast, southeast, south, northwest, and a zenith, you would take the average of the north and south peak positions plus the average of the southeast and northwest peak positions and average those with the zenith peak to obtain an average peak position for that time. Note that even though a measurement to the northeast is available, it is not used since there is not a measurement to the southwest to balance it.

The average peak position found at each time is then subtracted from the calibration lamp peak position at that time to determine the offset. These offsets are tabulated and then averaged to get an average offset for the night. This average offset then can be applied to the calibration lamp peak position at each measurement time to give a zero Doppler shift position, or the "baseline." The overall accuracy of this method is also somewhat affected by the accuracy of the uniform wind field assumption. We can reduce this error considerably by using an average offset which is calculated over many days or months of data. The OH winds presented in this thesis from the winter of 1991/1992 were derived using a three-month average of the calculated offsets.

The baseline found using this method will not be a constant through the observing period, but rather will reflect the actual instrumental drift as mentioned above. While this drift theoretically is minute and slowly varying, the peak positions for the calibration lamp, and hence the baseline, for both 8430 Å and 6300 Å data had a large amount of noise associated with them. Furthermore, the 6300 Å calibration source appeared to be much less noisy than the 8430 Å source.

This noise could be directly attributed to the presence of and to variations in the intensity of the background signal present in each of the calibration source measurements. Because the signal intensity generated by the calibration source will be very constant over time (we did verify this behavior in the data), the statistical uncertainty associated with it should also be a constant. In the absence of any background emissions, the intensity and uncertainty would be constants. However, because the magnitude of the background directly affects the certainty of a measurement, and the background intensity is large and shows considerable variation, the associated uncertainty is much larger than expected and the resulting baseline is noisy.

This not only explains why this problem appears worse on cloudy nights, when the background is often much higher, it also explains why the 6300 Å calibration source suffered much less from this effect than the 8430 Å source. The 8430 Å calibration source typically has a background which is comparable in magnitude to the emission signal, while the 6300 Å source is usually 3 to 4 times larger than the background. Hence the 8430 Å peaks show a lot more variability through the night.

To reduce the influence of this statistical uncertainty on the zero-velocity baseline, it is appropriate to fit the noisy baseline with a polynomial. It will then represent the best estimate of the baseline. The experimental standard deviation of this fit and the data points from the calibration lamp represents the certainty to which we know the actual zero velocity at any point in time and provides a way of verifying or scaling the uncertainties found by the Fourier procedure.

In calculating the fit to the baseline, the data points are weighted by the reciprocal of the variance found by the Fourier cutoff procedure. The resulting fit through the data appears to be offset because the smallest points have the smallest uncertainties. (If a constant uncertainty is assumed, the resulting baseline is found to be unrepresentative of the actual zero.) The effect of weighting was also examined in depth by plotting the zero

position calculated using opposite pairs of measurements against the zero position found from the fit to the offset calibration peaks. When the weighted uncertainties are used, there is a much larger correlation between these two estimates. The results of this procedure are illustrated in Figure 30. It shows the zero velocity found from an E-W pair of positions, the calibration curve with the offset applied, and a third order polynomial through the offset-calibration positions.

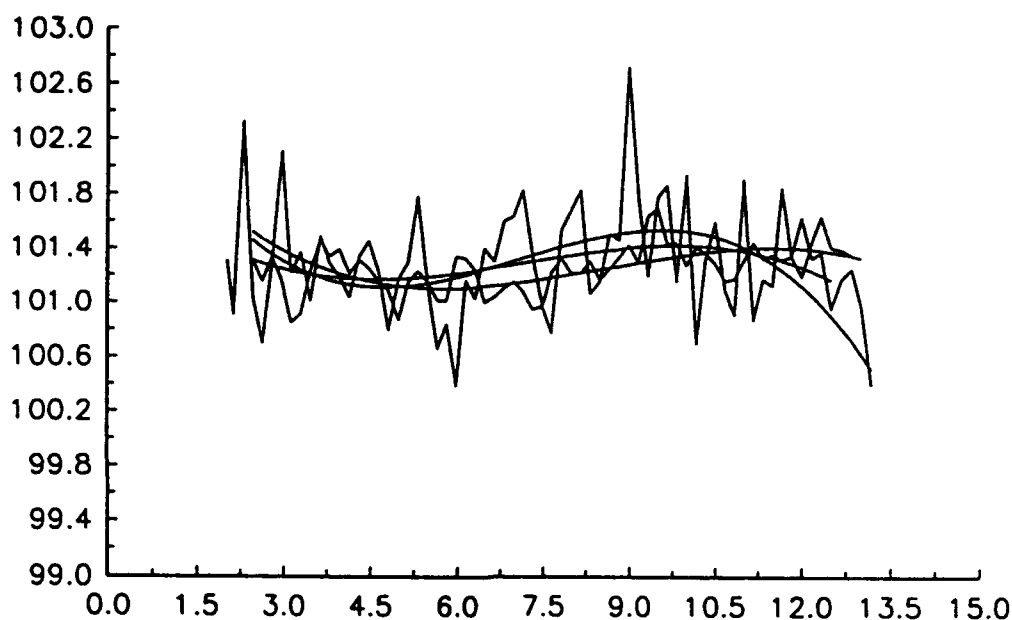


Fig. 30. Three estimates of the zero velocity position.

6.2.2 Wind Velocities from Doppler Shifts

After the baseline is calculated, wind speeds are found using the relationship:

$$v = c \frac{\Delta\lambda}{\lambda} \quad (6.6)$$

where v is the wind speed, c is the speed of light, $\Delta\lambda$ is the Doppler shift, and λ is the emission wavelength.

Of course it is not practical to use this form of the equation since the Doppler shifts associated with the interferograms are in the "bins" domain rather than the

wavelength domain. To convert these Doppler shifts of the peaks in "bins" to wind speeds in meters per second, the free spectral range is used. Because the value of the free spectral range can be determined directly from the interferograms, its units will also be "bins." The velocity (v) then can be found using Equation 6.7

$$v = \frac{\text{DopplerShift}(\text{bins})}{\text{FreeSpectralRange}(\text{bins})} \frac{c\lambda}{2t} \text{ m/s} \quad (6.7)$$

where t is the etalon plate spacing. Notice that this conversion is dependent on an accurate calculation of the free spectral range. For the instrument configuration at Utah State for 8430 Å data, Equation 6.7 becomes:

$$v = 41.7 * \text{DopplerShift}(\text{bins}) \text{ [m/s]} \quad (6.8)$$

For 6300 Å, the constant becomes 41.93. This equation is also used to convert the error in bins to an error in meters per second.

6.2.3 Total Error in the Calculated Wind Speed

In the calculations of the uncertainty to this point, we have used the estimate found during the Fourier analysis. Although it behaves as an uncertainty, e.g., doubling when the signal plus background is quadrupled, it is not a rigorous calculation of the uncertainty. Indeed, the first moment calculation indicated it should be increased in size. Thus we make the assumption that the final uncertainty in the wind magnitude is proportional to the precision of the peak found from the Fourier cutoff analysis, but is larger by some factor that can be estimated by comparing the smooth baseline and the measured calibration peaks.

By considering the calibration peaks with the offset applied, N_i , the uncertainty of those offsets found in the Fourier analysis σ_i' , and the polynomial fit to those peaks f_i , the idea is to find and compare two measures of the average variance for an observed peak. If the σ_i' are correct, then the average variance of a point derived from N points is

$$\sigma^2 = \frac{N}{\sum_i \frac{1}{\sigma_i'^2}} \quad (6.9)$$

By comparing the points and the fit, the weighted average variance is

$$\sigma^2 = \frac{\sum_i \frac{[x_i - f(x_i)]^2}{\sigma_i'^2}}{\sum_i \frac{1}{\sigma_i'^2}} \quad (6.10)$$

The new estimate of the variance for a peak position becomes

$$\sigma_i^2 = \sigma_i'^2 \left\{ \frac{\sigma^2}{\sigma_i'^2} \right\} = \sigma_i'^2 * f \quad (6.11)$$

and the \sqrt{f} will be used to scale the standard deviation found in the Fourier cutoff analysis. The result of this scaling generally gives errors of ± 3 -20 m/s for the OH observations. The small uncertainties are the most common. The large ones arise, for instance, under full moon conditions when the background is greatly enhanced. These appear to reflect well the uncertainty of the derived wind speeds.

In finding the experimental variance σ^2 defined in Equation 6.8, one has to be very careful to make sure any "bad points" are eliminated. A bad point can increase f by a factor of two to three. This editing is done by calculating σ^2 using all the points, eliminating any points more than three standard deviations away, and then recalculating σ^2 .

6.3 Presentation of Wind Data

There are several different methods of presenting the wind data obtained from the individual measurements. Each of the individual line-of-sight winds can be converted to an equivalent horizontal component by dividing by $\cos \theta$ where θ is 30° , the elevation angle of the observation. These can be individually presented as the horizontal line-of-

sight winds for a given azimuth. Alternatively, the individual wind vectors can be interpolated to a common time, such as the time of the calibration measurement, and combined using a least-squares fitting routine to find the overall wind vector. This vector can then be divided into its zonal and meridional components to give an overall view of the wind field. This method is effective in displaying gradients in the wind field on a night-to-night basis.

An alternative to presenting the winds "as obtained" is to linearly interpolate the Doppler shifts in each direction to 15-minute intervals through the observing period. These can then be used to show either the horizontal component of the calculated winds in each direction at every 15-minute interval, or they can be combined as above to find the overall zonal and meridional winds at 15-minute intervals. The interpolation process tends to smooth the results and thus it is good for presentation purposes.

CHAPTER 7

ANALYSIS

7.1 Observations of 8430 Å OH Near The Mesopause

One of the primary goals of this project was to allow comparison of several parameters taken from a single measurement. The fact that both winds and intensities (and the kinetic temperature) can be measured simultaneously with the Fabry-Perot greatly increases one's ability to look at the "whole picture" when analyzing the data. We have used this new capability to do a preliminary survey of the data from December 1991 through the first part of March 1992. The overwhelming conclusion to be drawn from the behavior of the winds near the mesopause during this period (winter) is that there are large day-to-day variations in what is observed. Figures 31 and 32 show the background intensity, relative intensity, and the calculated meridional and zonal velocity components for 9 Jan 92. This was known to be a cloud-free night. In looking at the intensity of the background, notice how the curves nearly overlap, or are "bunched" together. This is indicative of a uniform background intensity across the entire sky, with intensities of ~15 counts/second. This background intensity pattern is typical of a cloudless night. Because 9 January was only 5 days after new moon, there is no effect or enhancement in any of the directions due to the presence of the moon.

The relative OH intensities on this night (Figure 31) show a distinct wave-like pattern with a period of approximately 8 hours. Also, the intensities in the various directions are not closely bunched as they were for the background. This indicates spatial gradients in the observed OH emission field. We found that there was a direct correlation between the sharpness of this gradient (reflected in how widely spread the intensity curves in the various directions appeared) and the magnitude of the observed winds.

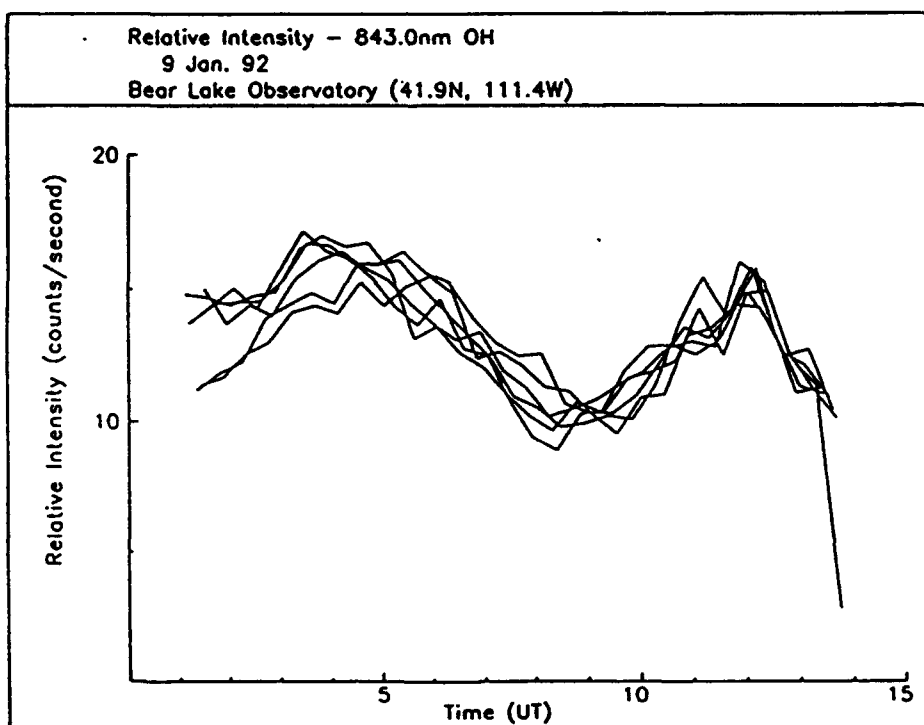
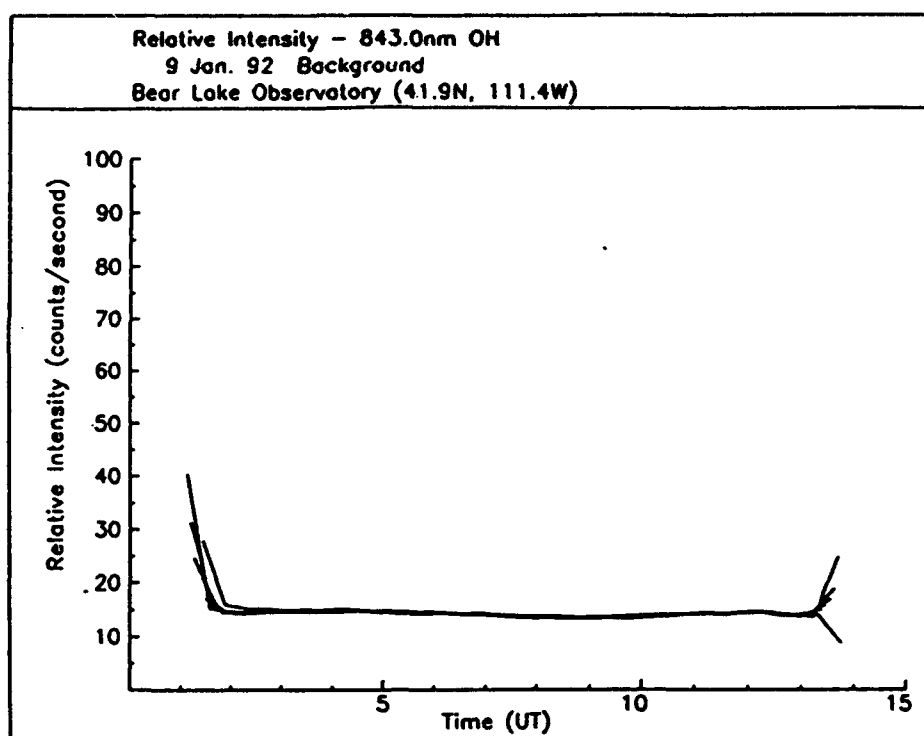


Fig. 31. Relative background (top) and OH (bottom) intensities observed near 87 km from Bear Lake Observatory on 9 Jan 92.

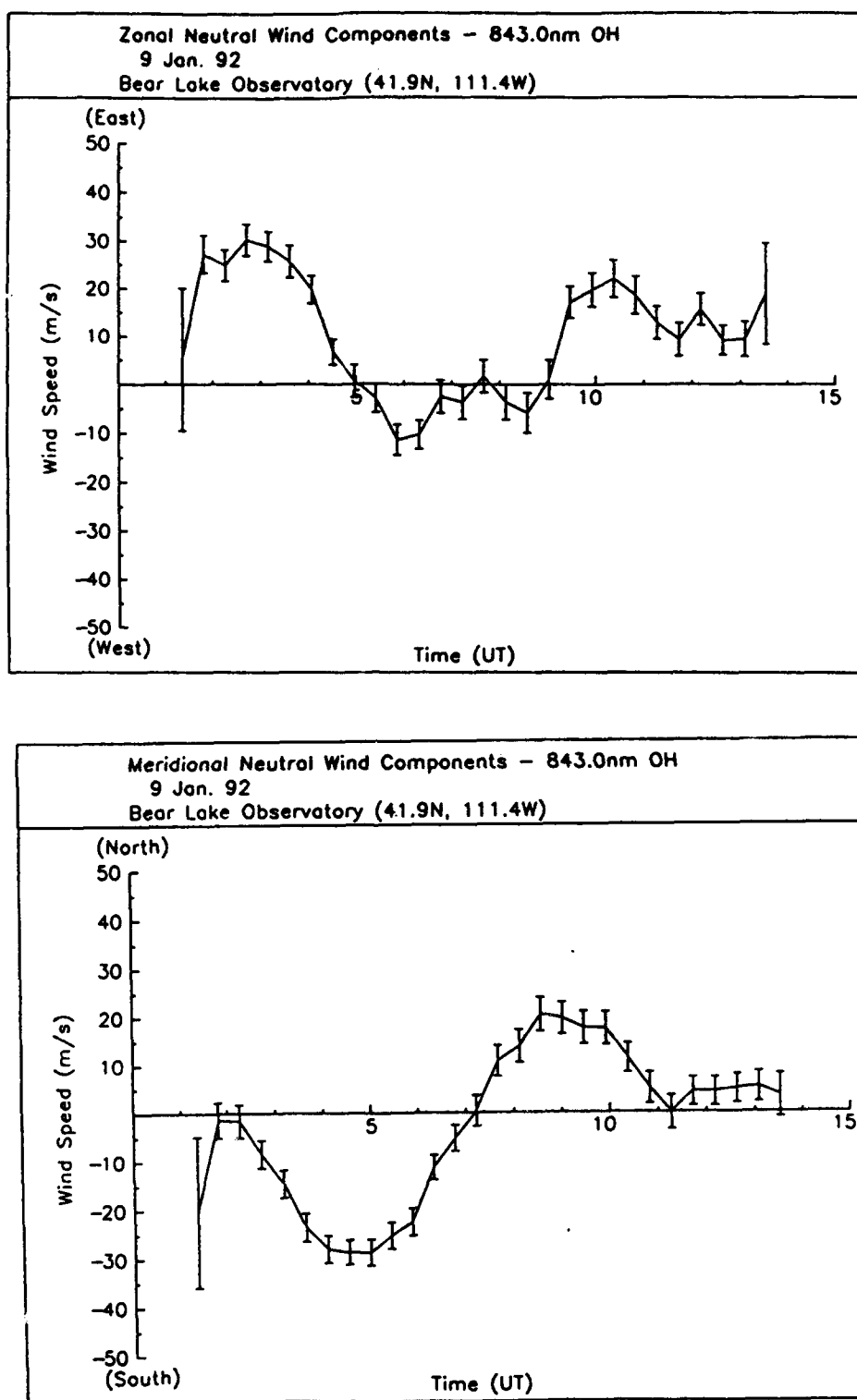


Fig. 32. Zonal (top) and meridional (bottom) neutral wind components observed near 87 km from Bear Lake Observatory on 9 Jan 92.

When the OH intensity lines were closely packed, the resulting wind field was small, with maximum winds of ~ 10 m/s, while larger gradients indicated larger winds.

A prominent feature of the winds on this day (Figure 32) is the apparent presence of a variation with a 8-hour period. The zonal and meridional components appear to be out of phase by approximately 3 hours, similar to what is expected for the semidiurnal tide. Although basic tidal theory predicts the dominance of the semidiurnal tidal component in this region of the atmosphere, this day was the exception rather than the rule, as there were only a few other days out of all of the data examined, which displayed this periodicity. The magnitude of the wind velocities on this day was 25 to 30 m/s.

Most days were more similar to what is shown in Figures 33 and 34, for the following day, 10 January 1992. The overall magnitude of both velocity components is quite small with no consistent pattern. This day appeared to be cloud-free based on the background intensity curves; however, in contrast to the previous day, the OH intensity curves are much more closely packed, indicating a reduced gradient, and a subsequent reduction in the overall wind speed. (The curve which falls well below the others on the OH intensity plot is the zenith, which is smaller because less signal is collected during the vertical observation for the same integration time.) The intensity begins very strong in all viewing directions, with more than 20 counts/second in several of the directions at the beginning of the night. This falls to half its original intensity over the course of about three hours, and then begins to rise again. The period of this variation is longer than the observation period. During the first few hours of the night, there is a slight spreading of the intensities, and this corresponds well to the slight increase in the winds during the first few hours of the night.

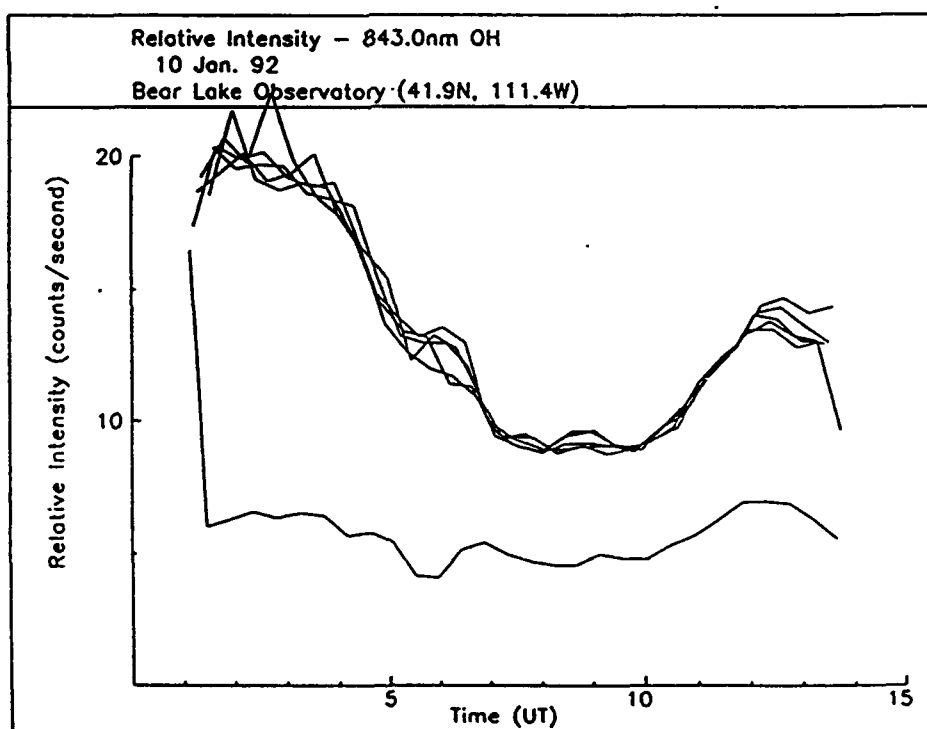
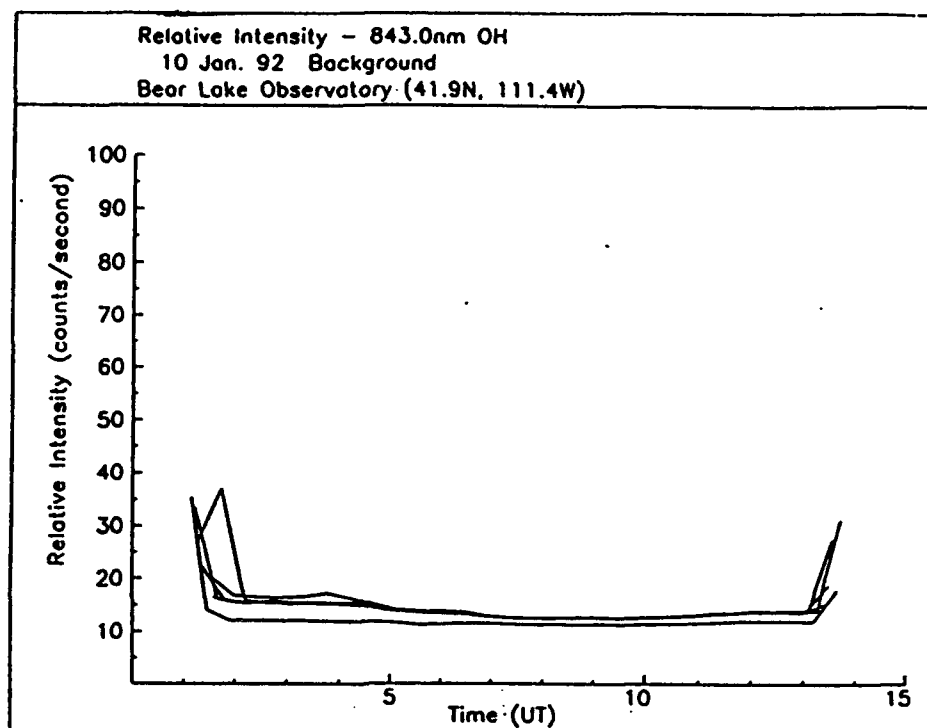


Fig. 33. Relative background (top) and OH (bottom) intensities observed near 87 km from Bear Lake Observatory on 10 Jan 92.

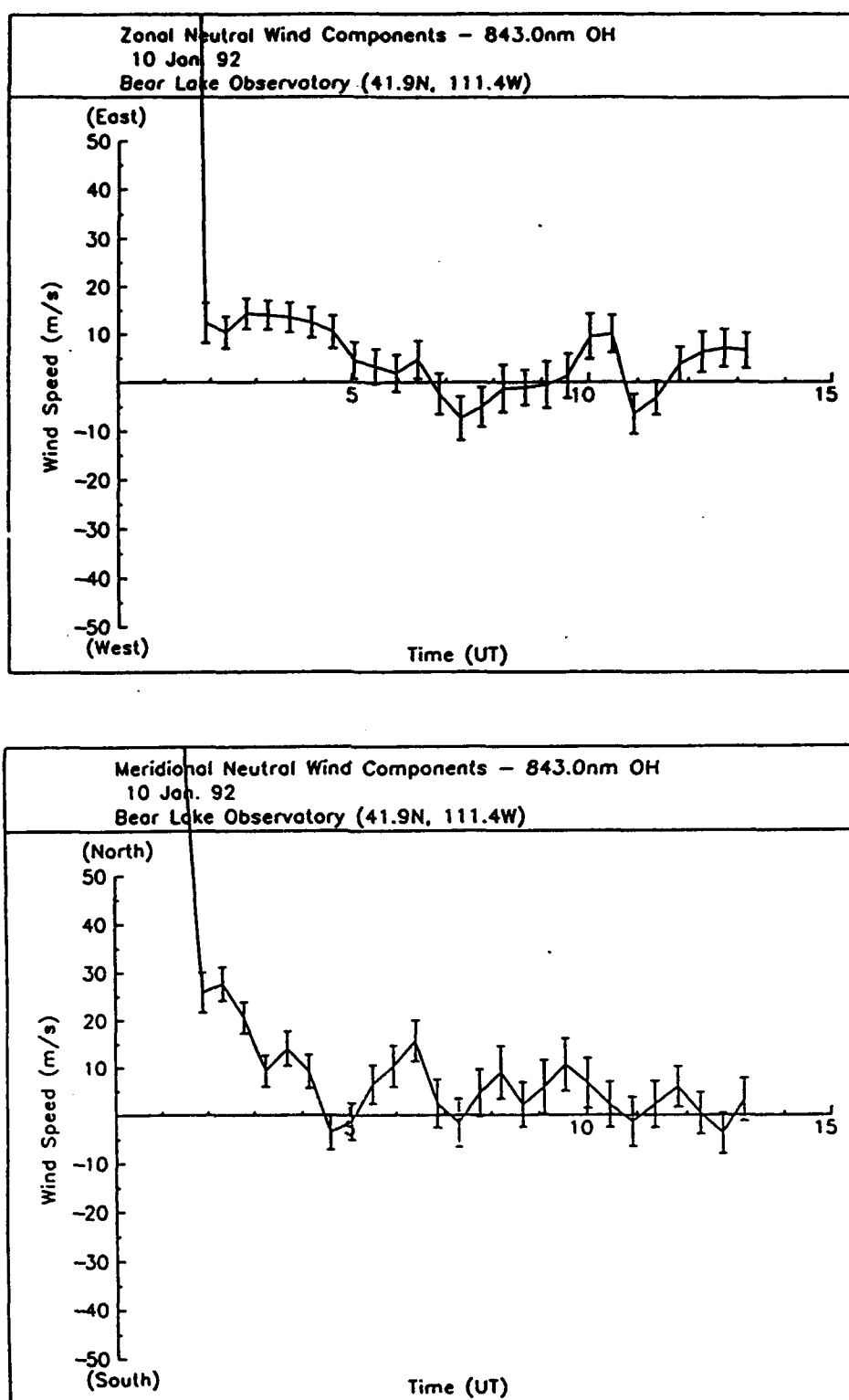


Fig. 34. Zonal (top) and meridional (bottom) neutral wind components observed near 87 km from Bear Lake Observatory on 10 Jan 92.

On 12 January 1992 (Figures 35 and 36), the unusual feature is the zonal wind which was strongly to the west the entire night. This is contrary to what is expected for winds due to diurnal thermal forcing, which should give winds to the east during the early part of the night. The small perturbation in the background during the first four hours of the night can be attributed to the moon being visible during those hours. One note on the moon is appropriate here. When we laid out the data by month, we could clearly see moonrise and moonset on each of the nights when thick cloud cover did not completely obscure the view. On clear or partly cloudy nights, the effects of sunrise and sunset are also clearly visible. During the periods close to full moon, the background signal is greatly enhanced such that it becomes a much greater part of the total signal collected by the Fabry-Perot. Consequently, the wind velocities calculated on these nights have very large error bars, rendering the data effectively useless. This may, in part, be due to a problem in operating HALO, which allowed the instrument to turn on when the moon is close to the observing direction.

On 30 January 1992 (Figure 37) the intensities were a maximum near local midnight. This was the only night examined which displayed this behavior. Based solely on the wide spread of the intensity curves and the magnitude and evenness of the background, one could predict that this was probably a clear night. The winds on this night (Figure 38) were predominately to the northeast through the entire period with velocities near 40 m/s.

In Figure 39, for 5 February 1992, the observed intensity variation through the night is exactly opposite to that observed on 30 January, with the lowest intensities occurring near local midnight as part of a wave-like pattern with an approximate 8-hour period. Their spread would indicate that we should expect to see some winds on this night. The background appears to be uniform with intensities comparable to that of the OH, indicating a clear night.

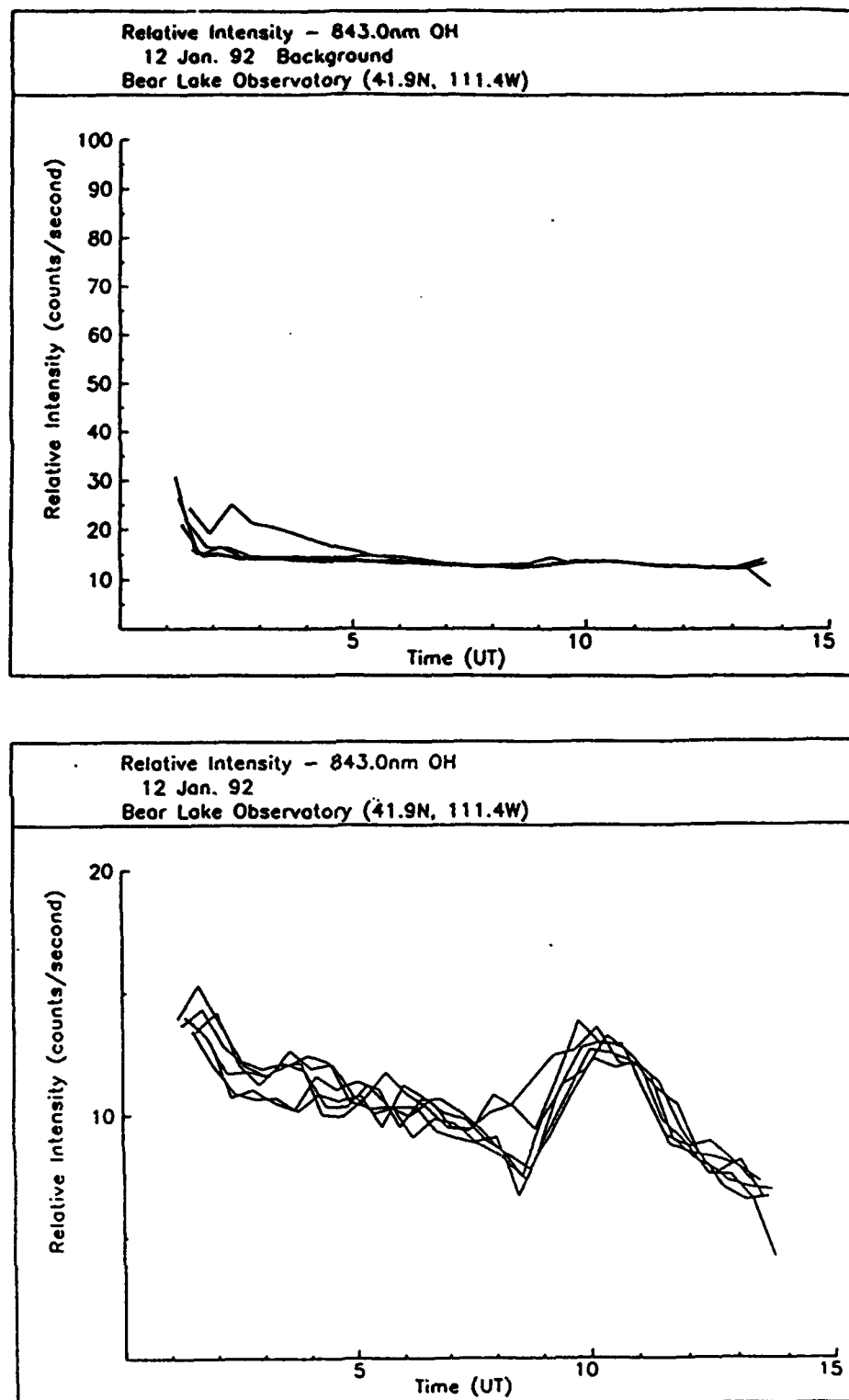


Fig. 35. Relative background (top) and OH (bottom) intensities observed near 87 km from Bear Lake Observatory on 12 Jan 92.

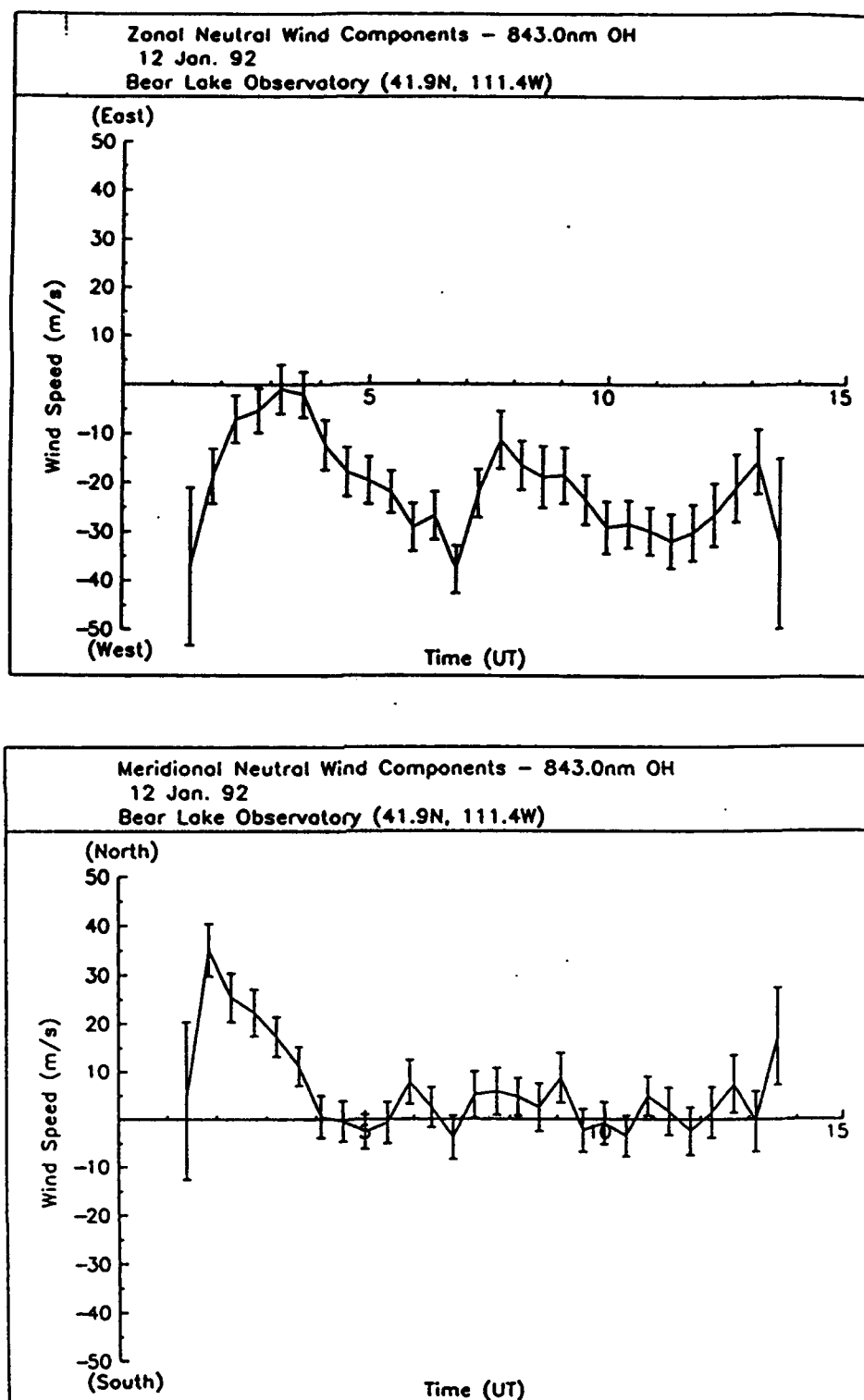


Fig. 36. Zonal (top) and meridional (bottom) neutral wind components observed near 87 km from Bear Lake Observatory on 12 Jan 92.

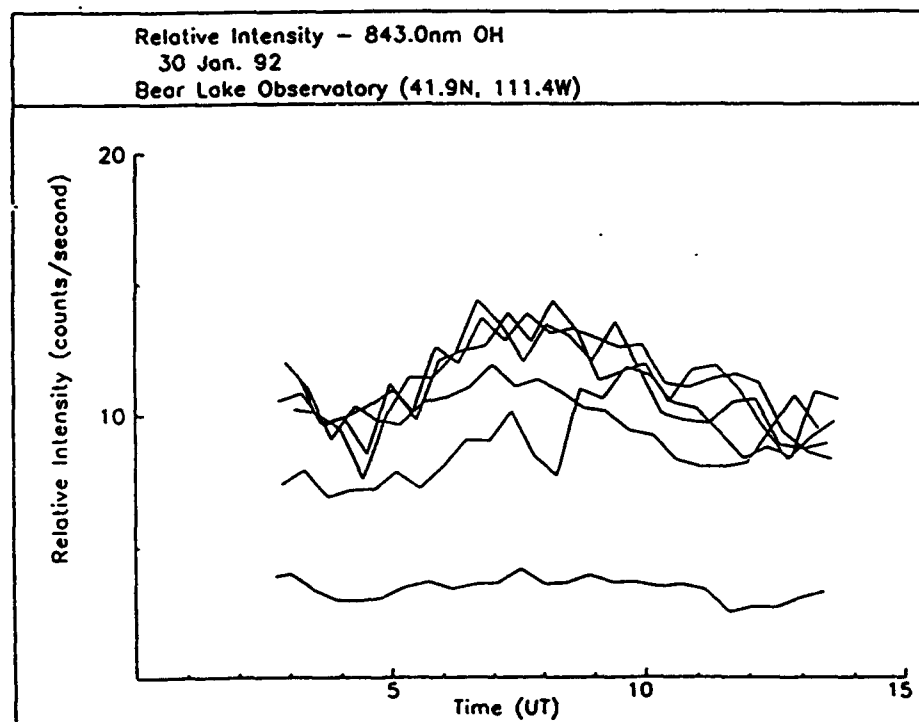
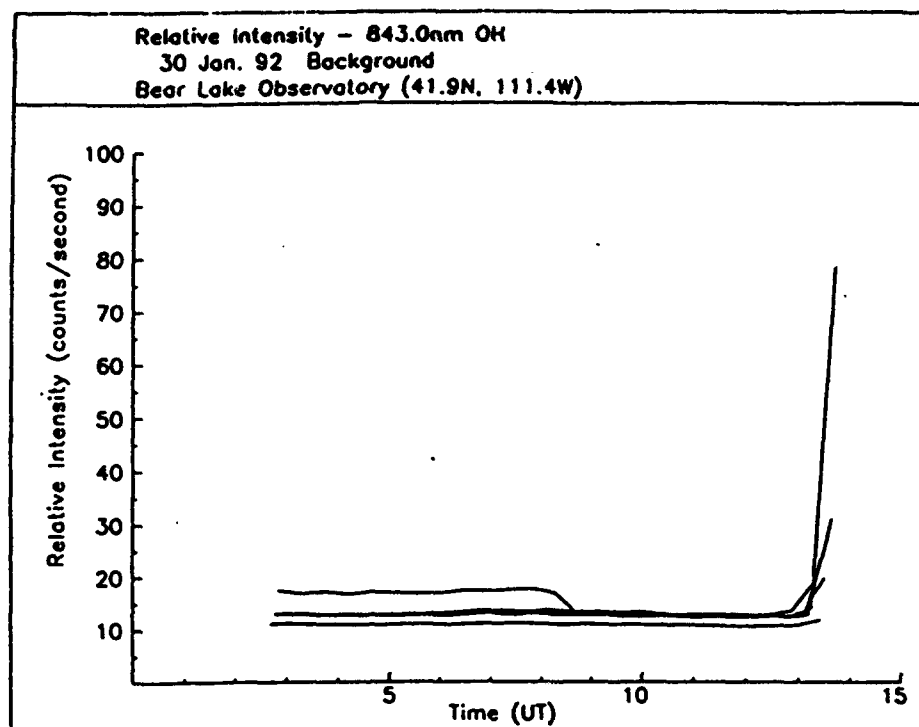


Fig. 37. Relative background (top) and OH (bottom) intensities observed near 87 km from Bear Lake Observatory on 30 Jan 92.

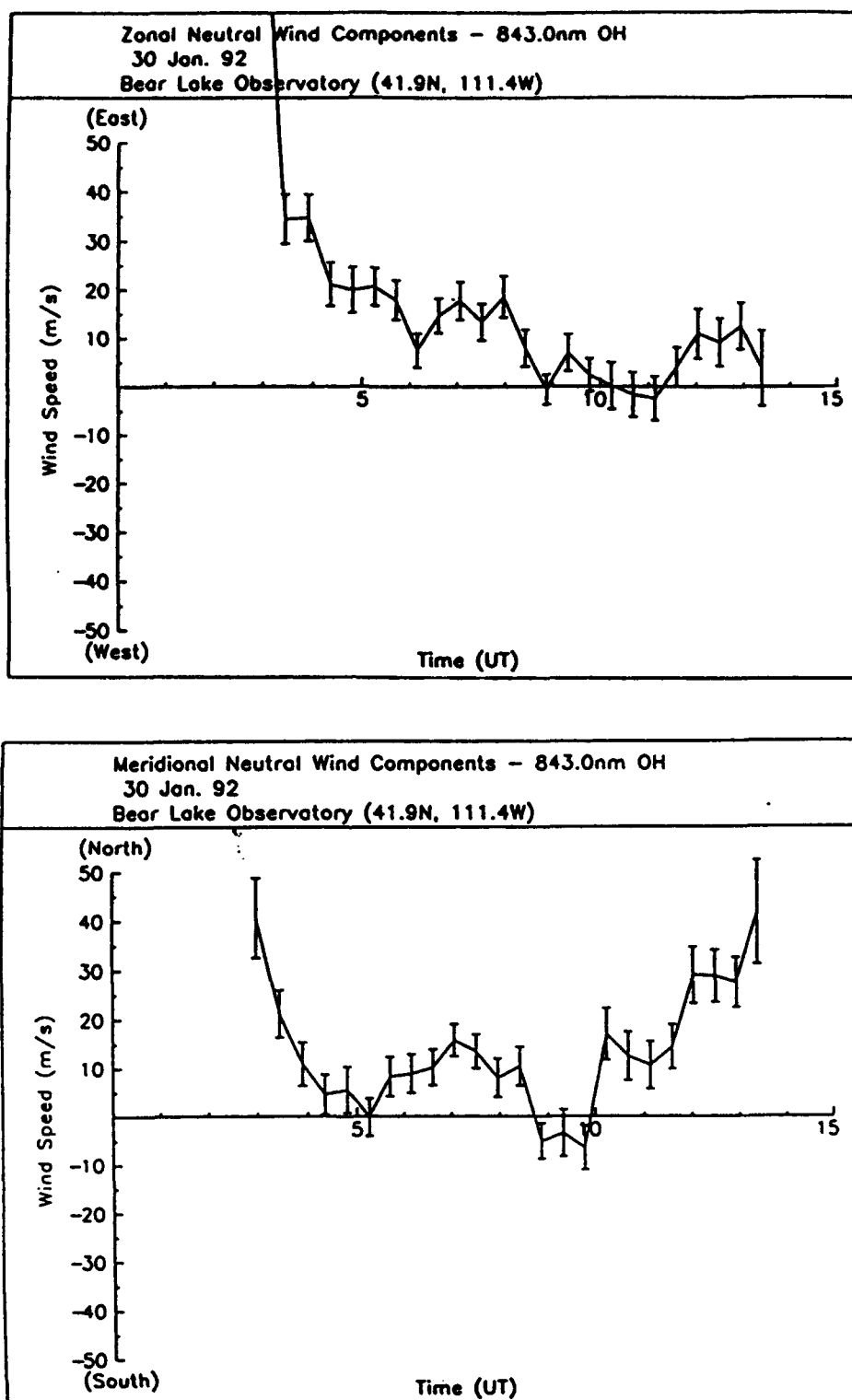


Fig. 38. Zonal (top) and meridional (bottom) neutral wind components observed near 87 km from Bear Lake Observatory on 30 Jan 92.

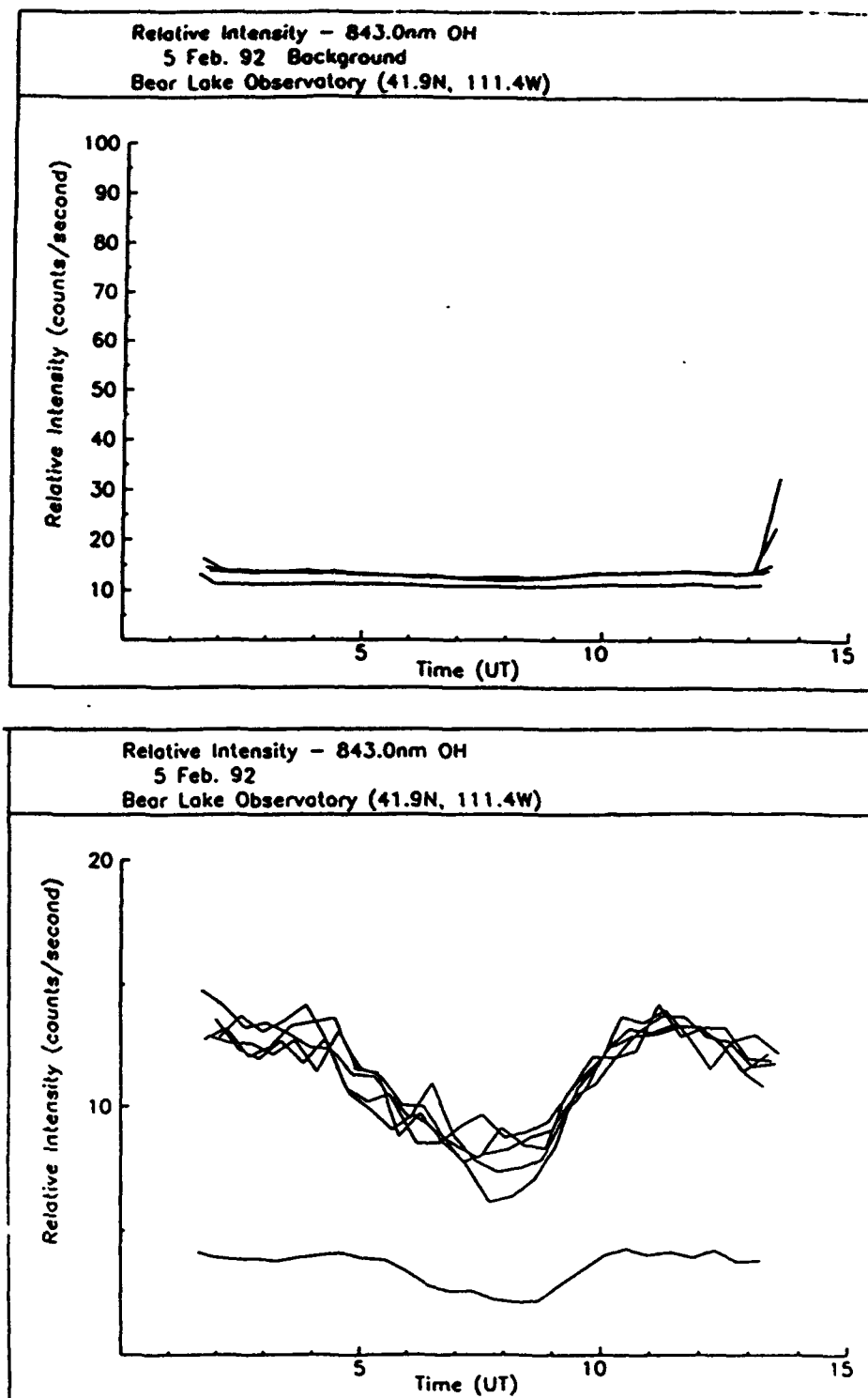


Fig. 39. Relative background (top) and OH (bottom) intensities observed near 87 km from Bear Lake Observatory on 5 Feb 92.

The zonal winds (Figure 40) are a bit unusual on this day as the winds are to the east at sunrise; however, the overall magnitude is what we expect.

Data from 27 December 1991 is shown in Figure 41. The obvious feature of the background intensity variation is the spike occurring near 10 UT. At present, it is unclear whether this is real or not. The perturbations which began in several viewing directions between 6 and 7 UT are associated with moonrise. The OH intensity pattern also shows a definite feature, which seemed to disturb all of the viewing directions between 6 and 12 UT. The spread of the pattern again suggests wind, and indeed, the zonal winds on this night were particularly large, and to the east through the entire night. The dip in the zonal wind curve (Figure 42) for a period between 6 and 12 UT corresponds well with the peak seen in the intensity curves. The meridional winds did not seem to be greatly affected by this feature.

The very next day, 28 December 1991, the wind pattern was observed to change dramatically. This is shown in Figure 44. On this day, the influence of the semidiurnal tide appears to dominate the wind field. These appear to be out of phase by approximately 3 hours, showing the phase quadrature expected for the semidiurnal tide. The background intensity (Figure 43) indicates a clear night, with the influence of the moon in the latter part of the night. The OH intensities showed a steady decrease during the first 5 hours of the night, and then appeared to level off.

One of the most interesting and unusual nights was 30 December 1991, only two nights later. The background (Figure 45) showed the typical behavior of a clear night. The OH intensity pattern shows a short (~2.5 hours) oscillation period that occurred continuously through the night. Notice how all of the directions were equally affected by this disturbance at nearly the same time, indicating a large-scale disturbance occurring

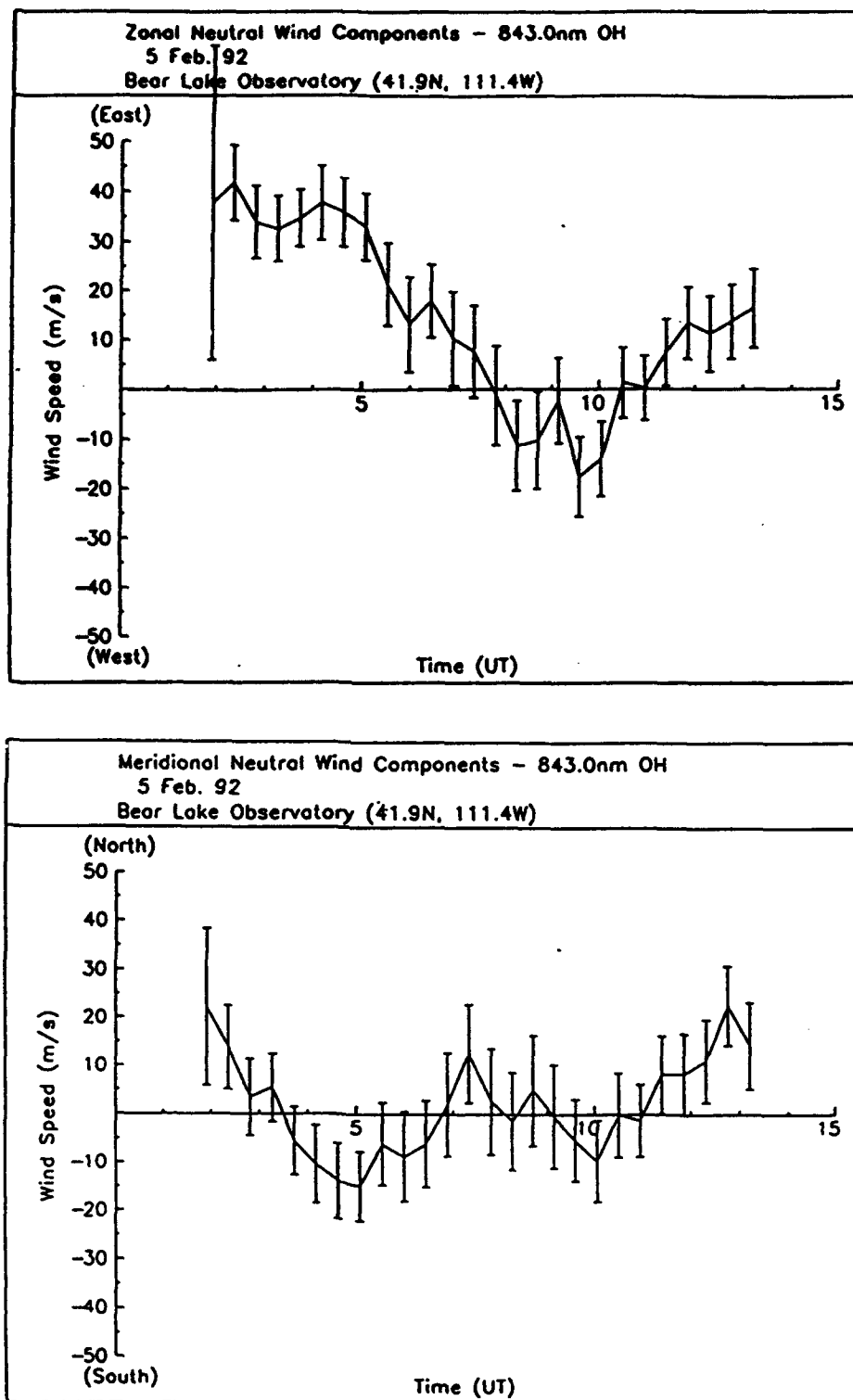


Fig. 40. Zonal (top) and meridional (bottom) neutral wind components observed near 87 km from Bear Lake Observatory on 5 Feb 92.

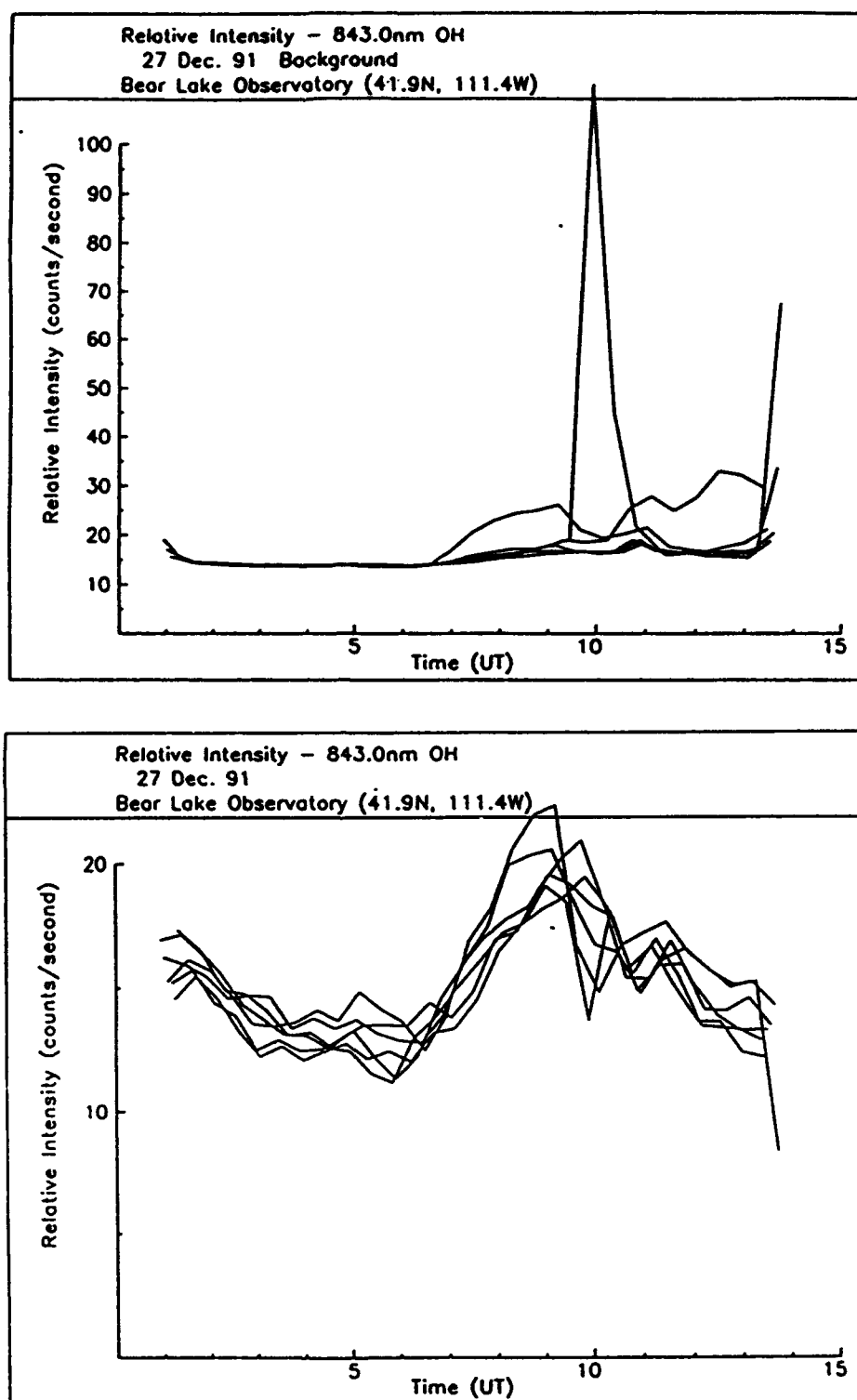


Fig. 41. Relative background (top) and OH (bottom) intensities observed near 87 km from Bear Lake Observatory on 27 Dec 91.

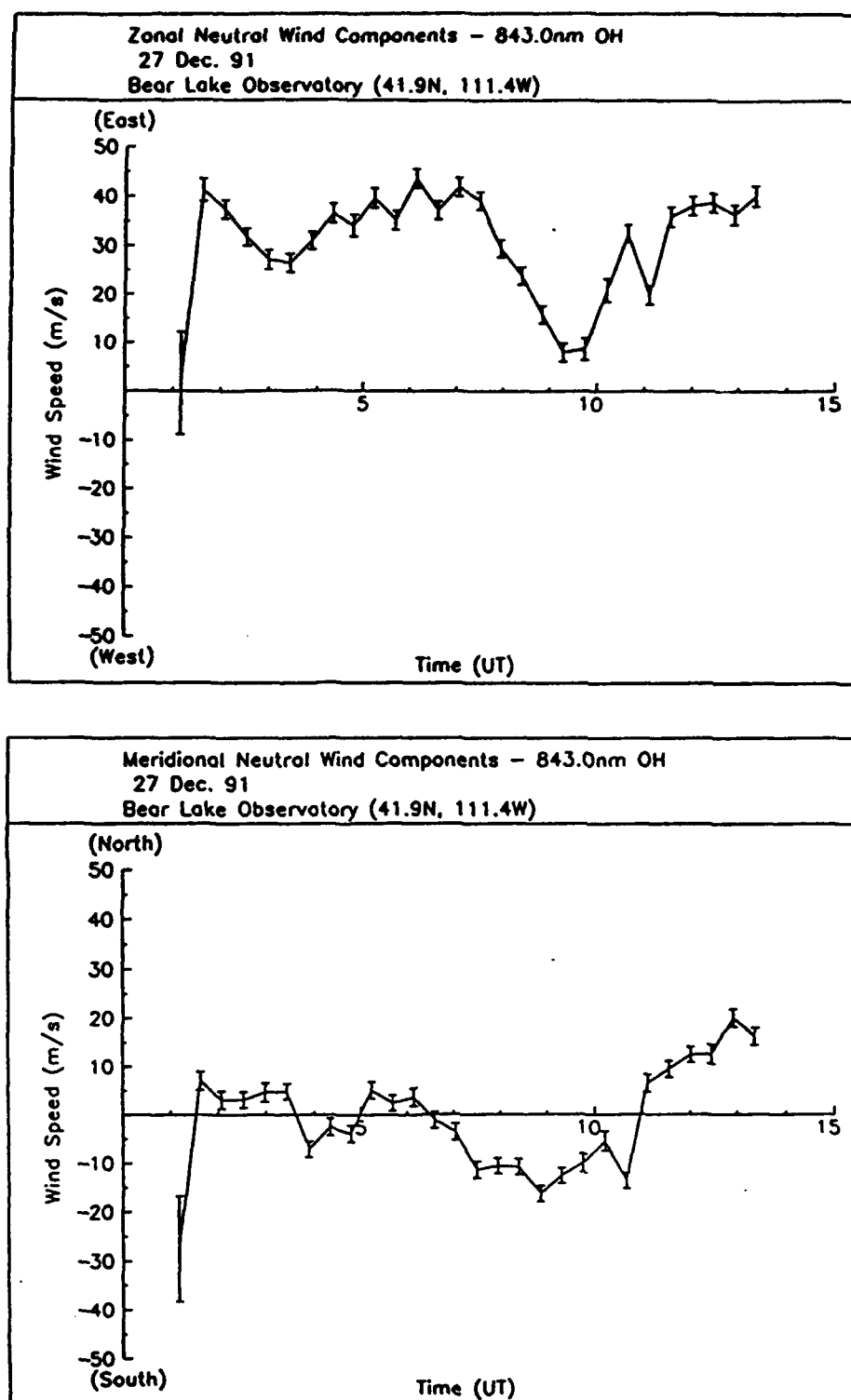


Fig. 42. Zonal (top) and meridional (bottom) neutral wind components observed near 87 km from Bear Lake Observatory on 27 Dec 91.

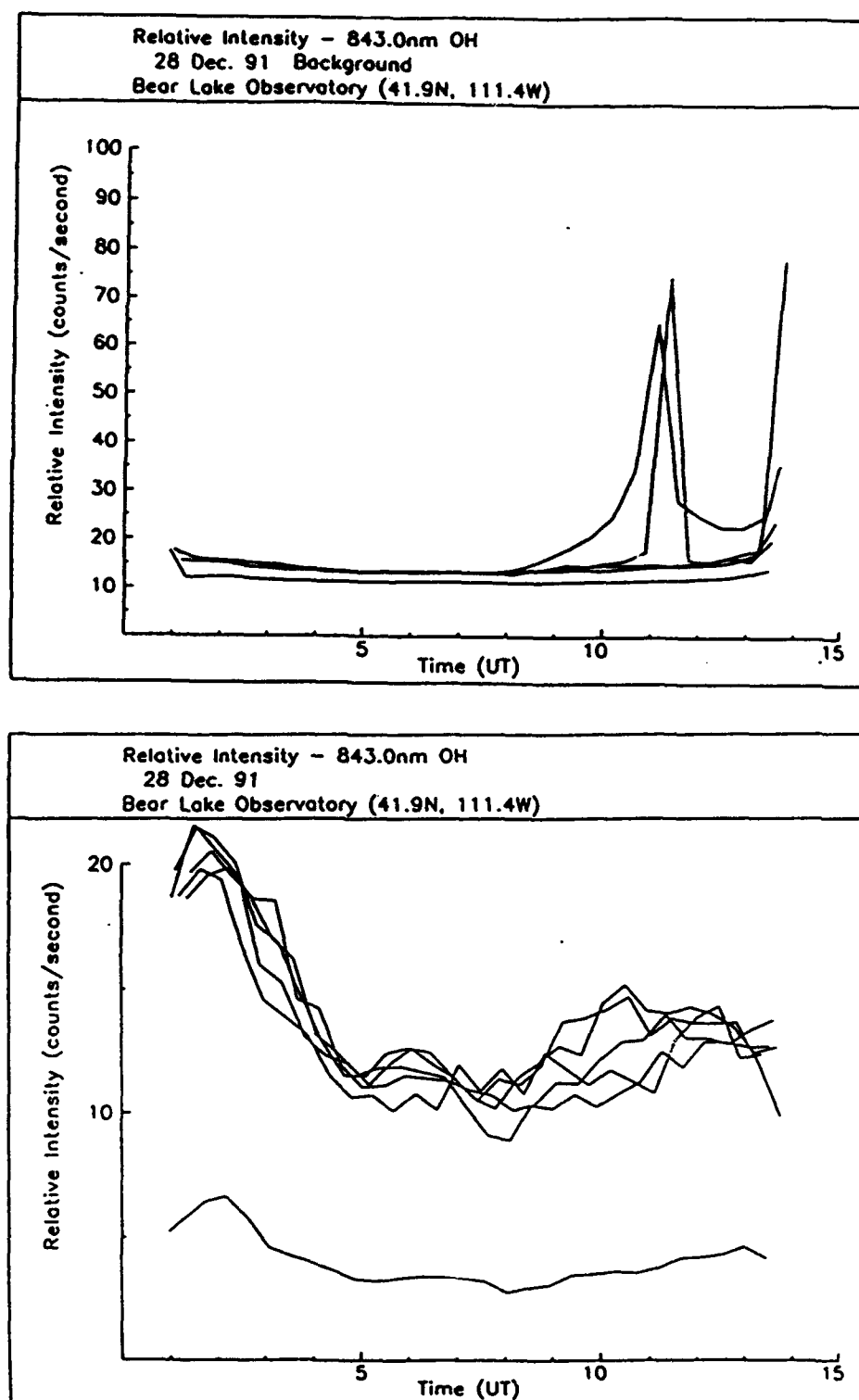


Fig. 43. Relative background (top) and OH (bottom) intensities observed near 87 km from Bear Lake Observatory on 28 Dec 91.

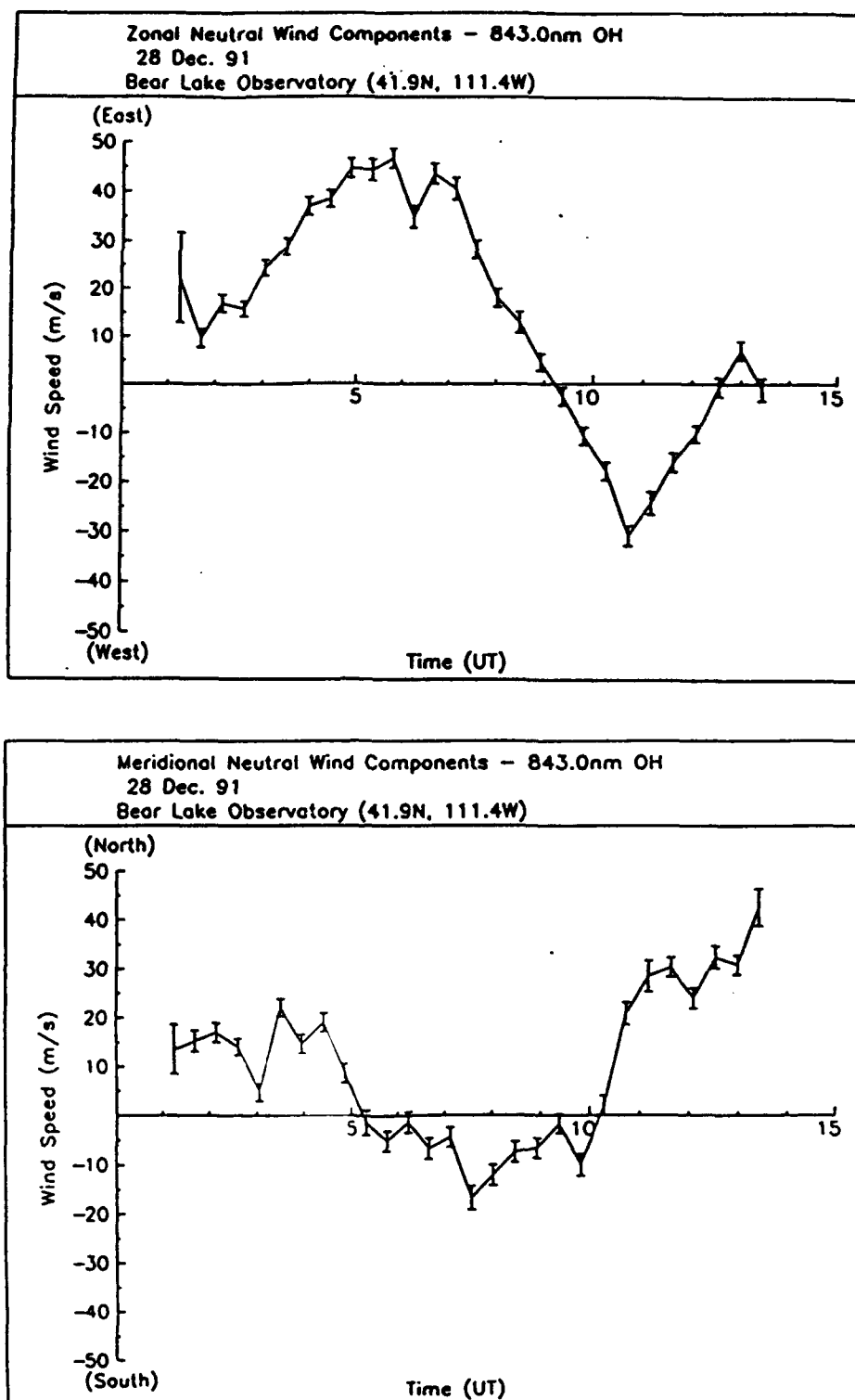


Fig. 44. Zonal (top) and meridional (bottom) neutral wind components observed near 87 km from Bear Lake Observatory on 28 Dec 91.

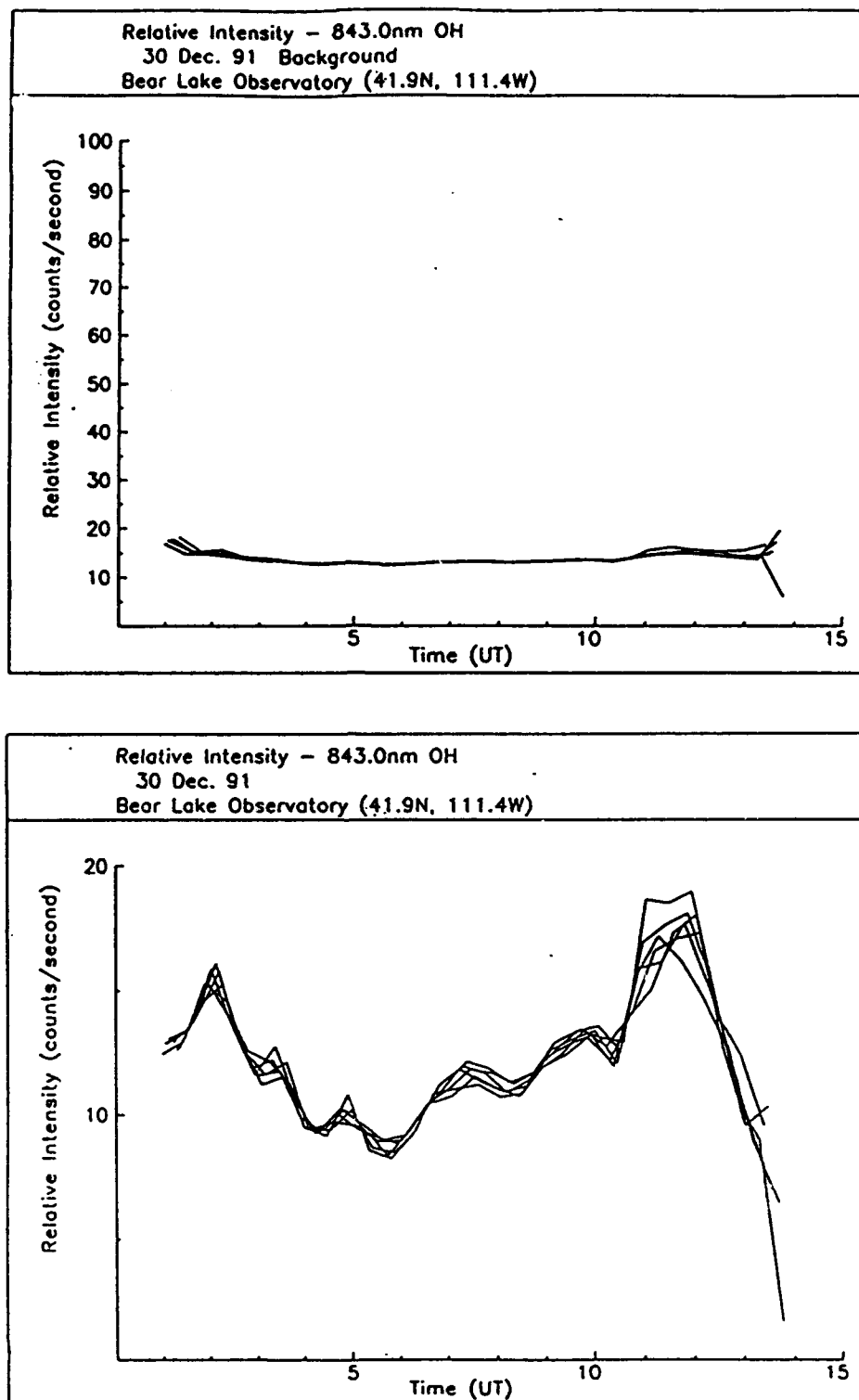


Fig. 45. Relative background (top) and OH (bottom) intensities observed near 87 km from Bear Lake Observatory on 30 Dec 91.

everywhere at once. The tight packing of the intensity lines denotes the absence of a gradient, and small horizontal winds. Indeed, both the zonal and meridional winds were very small throughout this night (Figure 46).

Overall, the zonal wind components appear to be larger than the meridional wind components, at least for the winter season. This is in line with theory. As was mentioned earlier, the most striking feature of both the intensities and the winds is the overall variability seen. It appears as though a pattern can appear for just one night with no hint of it on the day prior or the day after. The changes were indeed dramatic.

7.1.1 Interpretation of Clouds

All Fabry-Perot wind measurements are susceptible to corruption from atmospheric scattering due to pollution, aerosols, and clouds [Rees *et al.*, 1989]. Scattering by any mechanism is characterized by reduced mean Doppler winds or sudden large gradients if the scattering occurs only in a portion of the field of view. The presence of clouds causes scattering of the light emitted so that Doppler shifts from any direction are scattered and mixed together with the Doppler shifts from all other directions. As a result, the light collected by the FPI has lost most of its directional information and is an average of all of the Doppler shifts in the sky. If there is uniform emission over the whole sky and a uniform wind field, such that the light is scattered isotropically, then the observed Doppler shift in all directions averages out to zero.

Dense cloud cover is evident in the Fabry-Perot data not only as greatly reduced velocities but also by a significant reduction of intensity.

The interpretation of the effects of cloud cover become more difficult when only a portion of the sky is obscured or when thin and broken layers of cloud cover the observing site. If the sky is only obscured, say to the north, it will appear that a wind gradient existed since the winds will be near zero in the north, but will have a magnitude of say 30 m/s in the south.

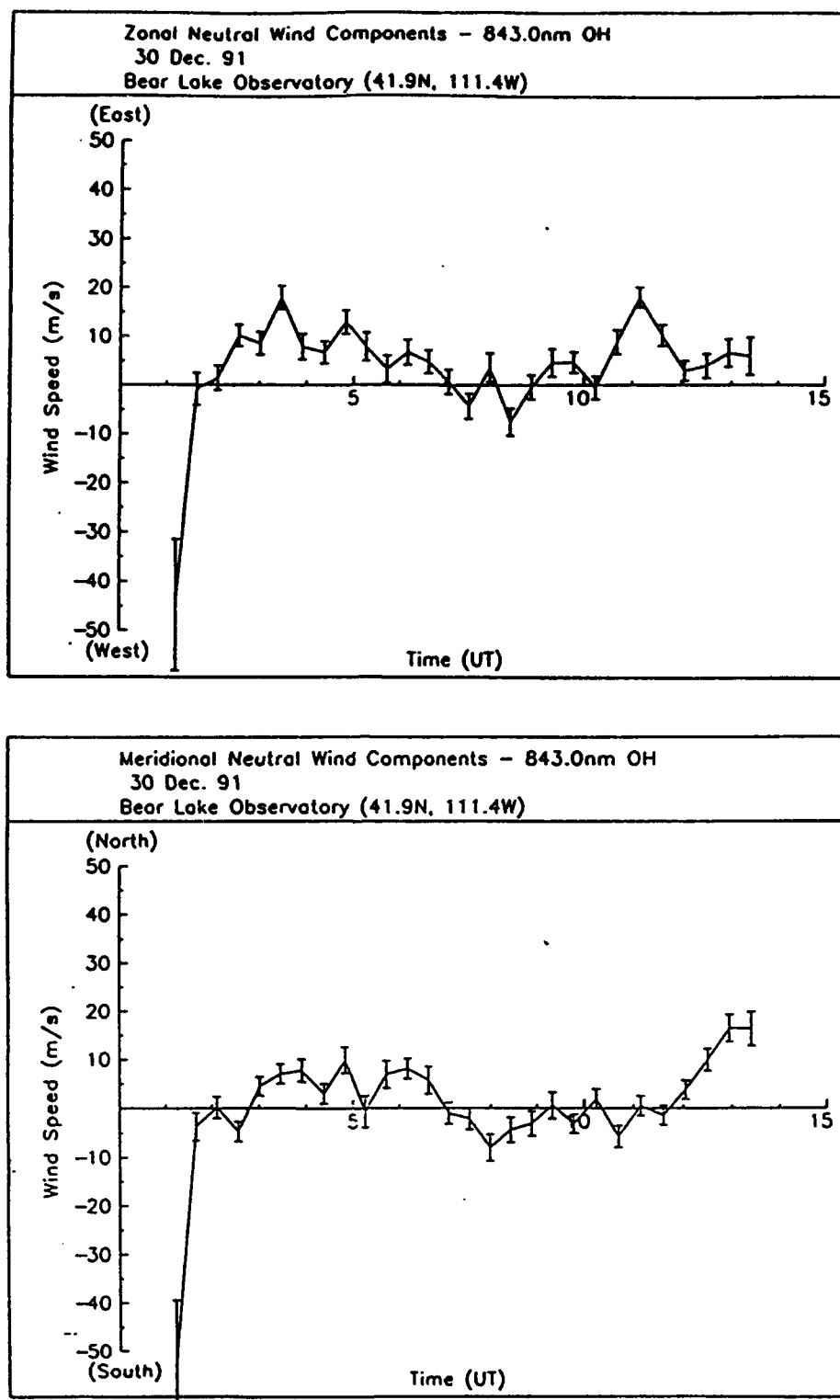


Fig. 46. Zonal (top) and meridional (bottom) neutral wind components observed near 87 km from Bear Lake Observatory on 30 Dec 91.

This emphasizes the importance of using a long-term average offset when determining the zero-velocity baseline. The use of a single average offset calculated on a night when there was variable cloudiness greatly affects the position of the calculated baseline and the error will affect all of the wind speeds calculated relative to this baseline.

The effects of scattering can be especially severe when large intensity gradients exist across the sky, such as when strong auroral activity is present. Careful interpretation of clouds must be done when auroral activity is present, because during auroral activity there are definite Doppler shifts even when conditions are cloudy. This may be a problem at Bear Lake because the station is far enough south in latitude that the auroral activity is seen mostly to the north and sometimes to the east. This will mean that there will no longer be uniform illumination of the entire sky due to clouds and the averaging out process due to cloud scatter will show a Doppler shift dominated by that in the north. This average Doppler shift will be observed in all directions, giving the appearance of a convergent or divergent wind field.

7.1.2 UARS

There have been two periods of correlative observations between BLO and the WINDII instrument on the UARS satellite: 4 November to 5 December 1991, and 13 January to 16 February 1992. During these periods there have been several nights when the FPI and WINDII were both observing OH and other nights when they were both observing 6300 Å. Although it has not yet happened, the intention is to compare velocities. This would be a very useful cross-calibration.

7.2 Observations in the F-Region

7.2.1 6300 Å O(¹D) Intensities and Winds

Figures 47 through 54 display some of the variations seen in the 6300 Å O(¹D) winds and intensities. Figure 47 from 28 February 1992 shows the intensity variation typically expected during quiet magnetic conditions. The preliminary magnetic data in Tables 11 and 12 do indicate this is a geomagnetically quiet day.

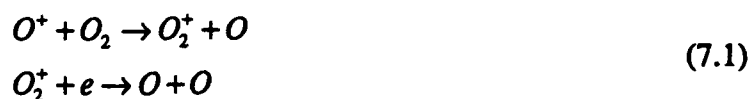
TABLE 11. K_p Indices for 6300 Å Data Analysis

Date	1-3 (UT)	4-6 (UT)	7-9 (UT)	10-12 (UT)	13-15 (UT)	16-18 (UT)	19-21 (UT)	22-24 (UT)
27 Jan 92	5	5	3	3	2	2	3	4
28 Jan 92	4	4	2	2	3	2	2	3
28 Feb 92	2	1	1	2	2	2	3	1
29 Feb 92	2	2	2	6	6	7	5	4
1 Mar 92	2	4	5	4	2	2	2	1

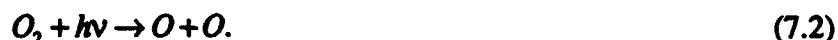
TABLE 12. A Indices for 6300 Å Data Analysis

Date	A Index
27 Jan 92	22
28 Jan 92	14
28 Feb 92	7
29 Feb 92	44
1 Mar 92	10

Right after sunset the rate of exciting O(¹D)'s in the F-region by dissociative recombination



is very high. This gives rise to strong OI(6300) emissions. The intensity decays during the night as the F layer decays. In the morning the intensity increases rapidly because of O₂ dissociation in the Schumann Runge continuum



As expected, this sharp increase occurs first when the FPI is observing to the east.

The zonal winds on the 28th (Figure 48) were initially blowing to the east at around 100 m/s, with a smooth reduction in speed, and a general reversal occurring between 9 and 10 UT. This is the expected direction of zonal flow due to solar thermal forcing. The meridional component began to the north and became southerly near 3 UT which is also consistent with solar thermal forcing, with a maximum observed speed near 80 m/s to the south. These results are quite similar to those for winter solstice conditions during solar cycle maximum shown by *Hernandez and Roble* [1979] for Fritz Peak.

On the 29th of February (Figure 49), the intensity pattern started as on the previous night, but then there was a disturbance to the normal pattern beginning between 9 and 10 UT, several hours before sunrise. This disturbance was seen by the Fabry-Perot, first to the north, then to the northeast, and finally to the northwest, and appeared to last beyond the observation period with peak intensities near 25 counts per second (off of the graph). The zonal winds on this night (Figure 50) began to the east as on the 28th at nearly 90 m/s, but instead of a continual progression toward the west, the flow stayed predominately toward the east the entire night. The meridional component overall was fairly small until near 9 UT when the winds in the east and north quickly jumped to velocities over 200 m/s toward the south and in the west they jumped to over 100 m/s toward the south. A weak zonal wind appeared to the north of BLO, but a strong one appeared in the east directed toward the east. The timing of this sudden increase in the winds to the east and south correlates very well to the timing of the disturbance seen in the intensities. The intensity and wind variations observed point to an auroral disturbance to the north of Bear Lake. The winds to the southeast suggest convection velocities.

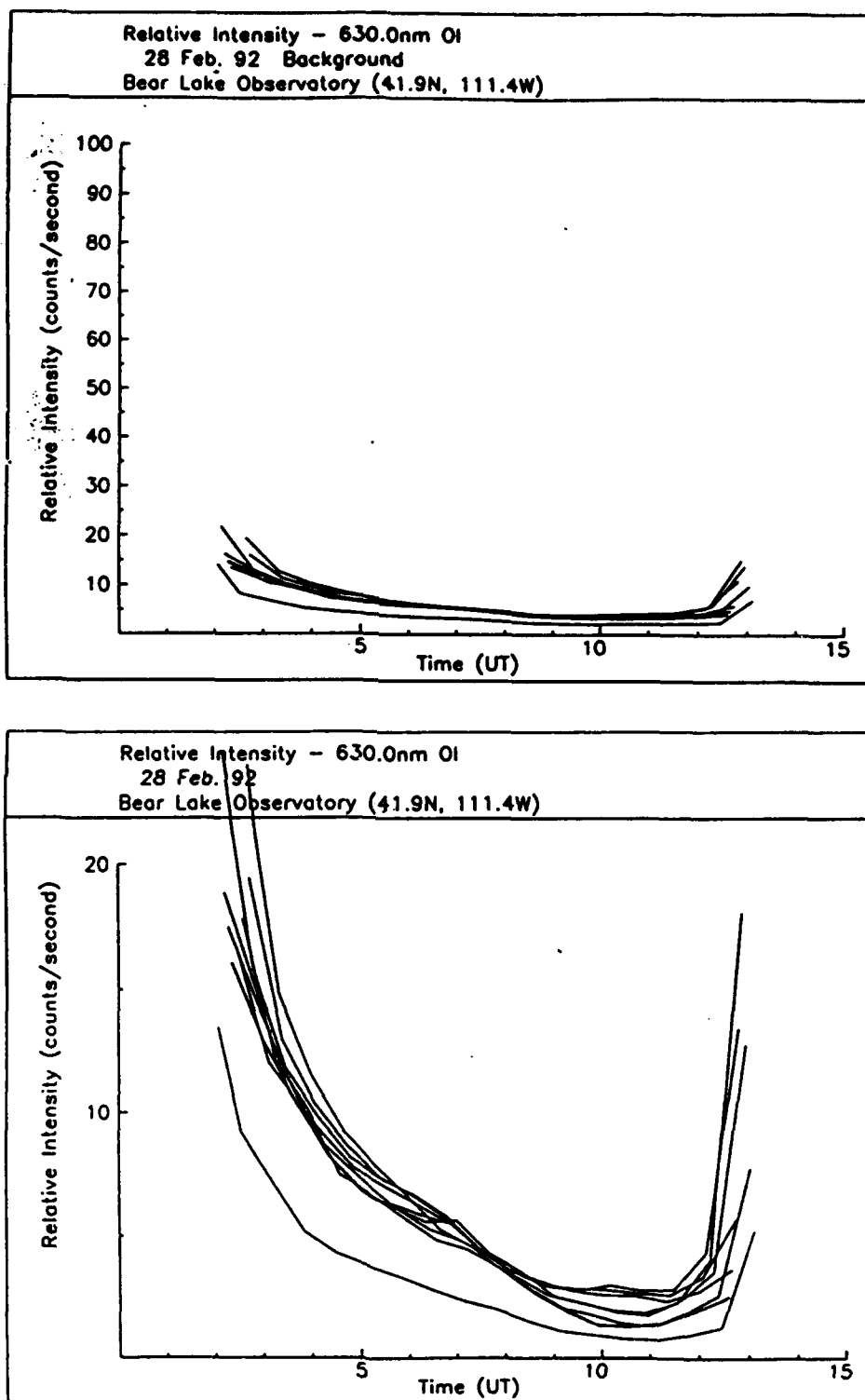


Fig. 47. Relative background (top) and O(¹D) (bottom) intensities observed near 250 km from Bear Lake Observatory on 28 Feb 92.

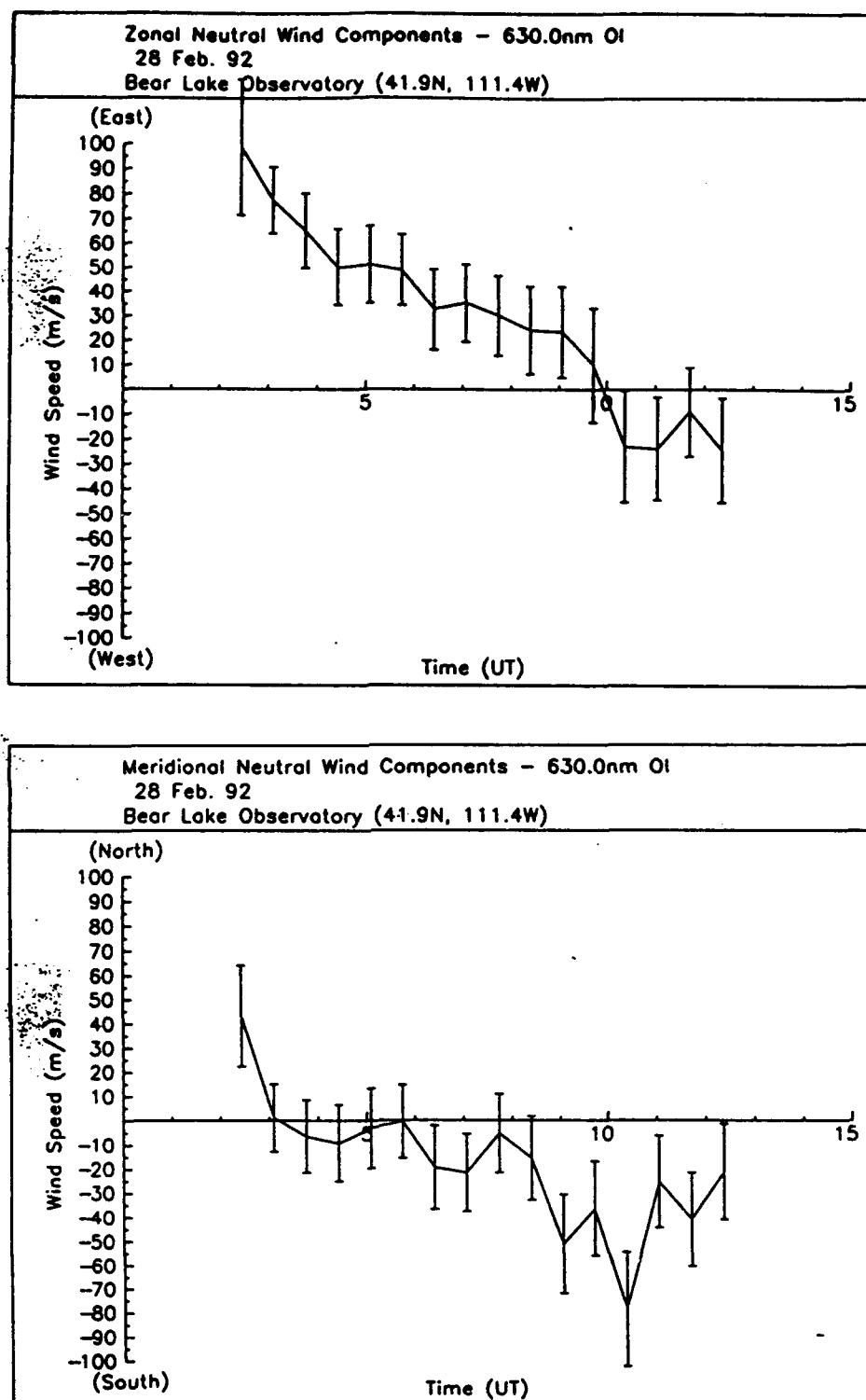


Fig. 48. Zonal (top) and meridional (bottom) neutral wind components observed near 250 km from Bear Lake Observatory on 28 Feb 92.

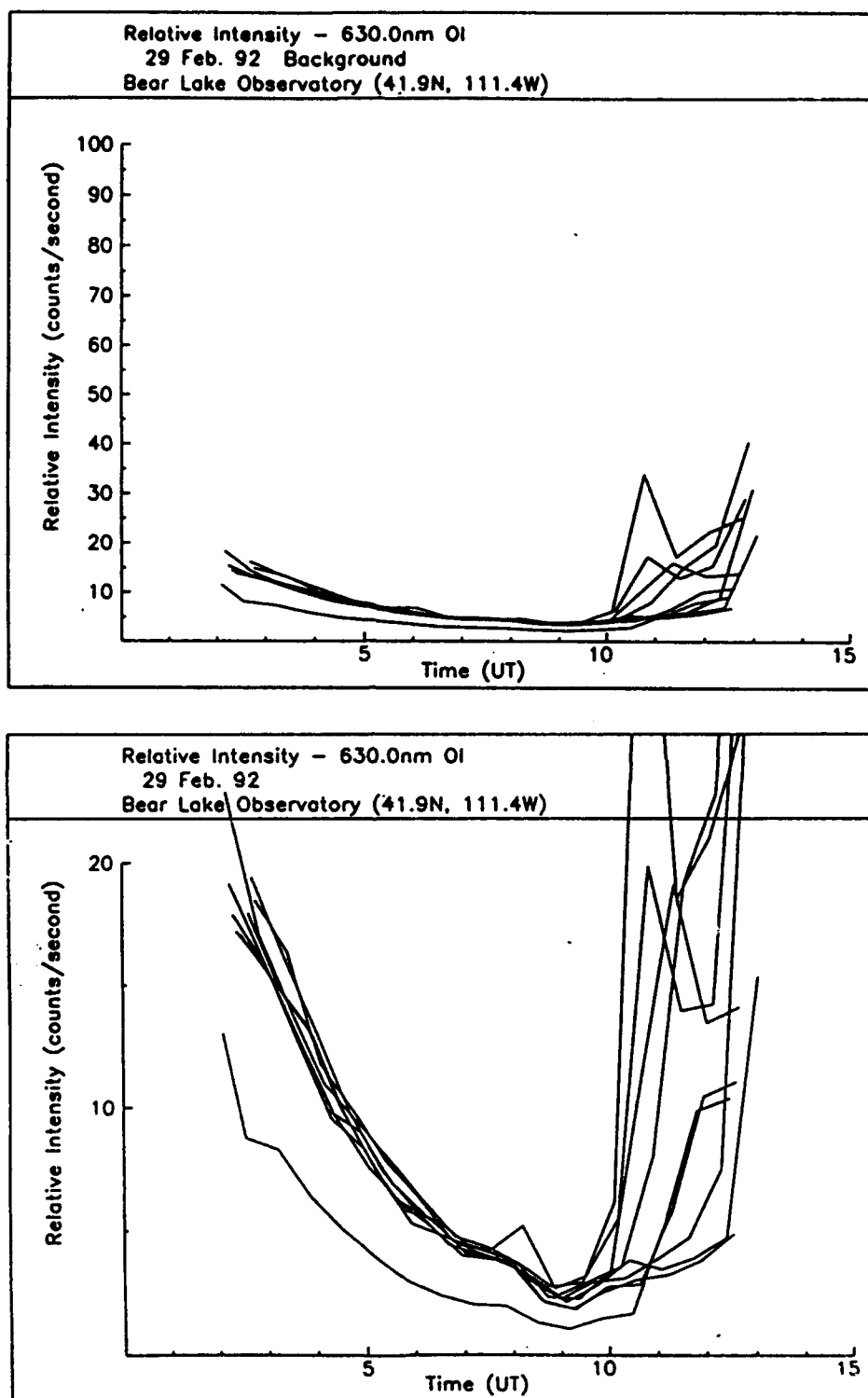


Fig. 49. Relative background (top) and O(¹D) (bottom) intensities observed near 250 km from Bear Lake Observatory on 29 Feb 92.

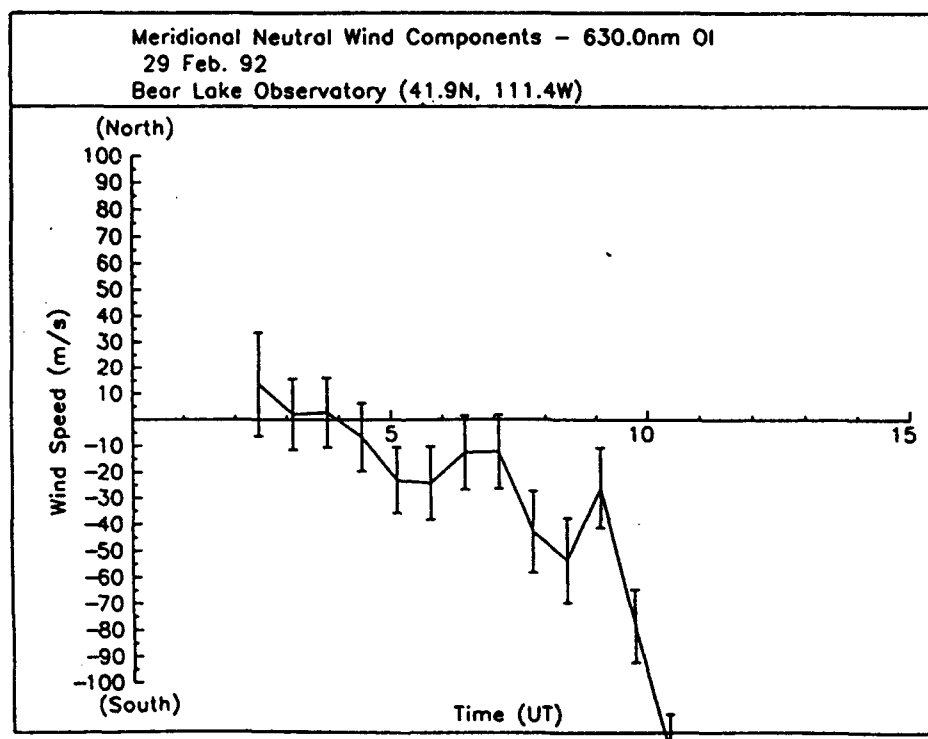
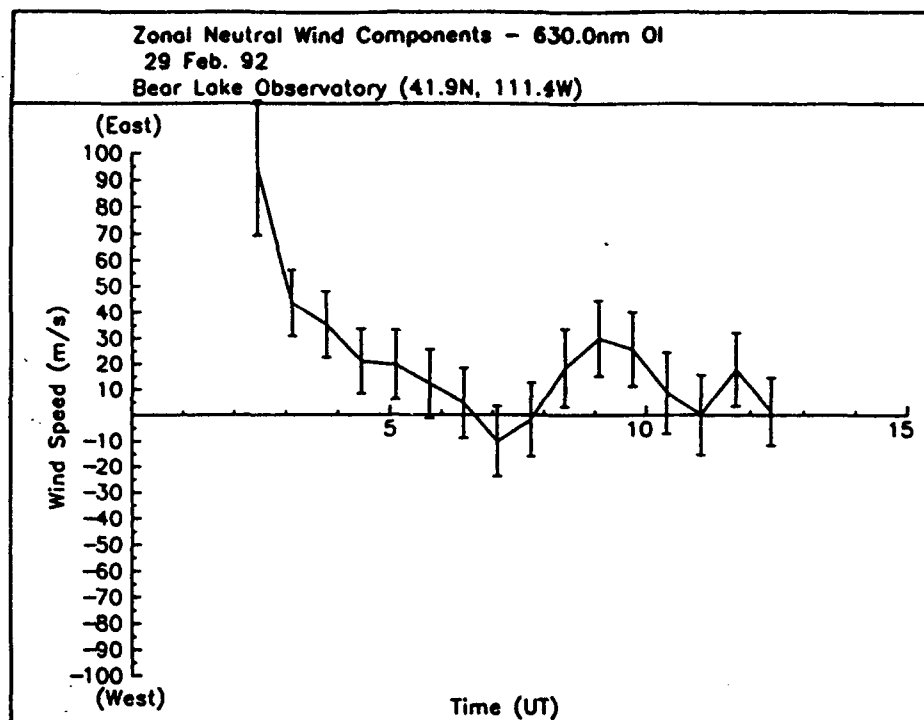


Fig. 50. Zonal (top) and meridional (bottom) neutral wind components observed near 250 km from Bear Lake Observatory on 29 Feb 92.

The intensity pattern observed on March 1st is striking (Figure 51). Initially the intensities after sunset were less than on the previous two nights. This might be the result of composition changes arising from the previous night's activity level. Then between 05 and 09 UT the intensities increased in the northeast, then in the north, and then in the northwest. They stayed enhanced until after 08 UT. Coincident with this intensity maximum there developed a strong neutral wind (150 m/s) to the west that is seen in the northern part of the sky, but not elsewhere (Figure 52). A reasonable interpretation would be that there was westward convection with ion velocities exceeding 200 m/s that was dragging the neutrals along. The precipitation was occurring in this region of westward convection. As this disturbance developed, a southward meridional wind developed in the east. Slightly later a northward meridional wind developed in the west. This wind was contrary to anything that would be expected on a quiet night. It undoubtedly was a consequence of the geomagnetic activity. It might have been the response to atmospheric heating, but the enhanced intensities were to the north, not the south. Therefore it seems more likely the northward meridional wind arose from ion drag. Thus the ion velocity would have components to the north and to the west.

Another active and interesting day was 27 January 1992 (Figure 53). Early in the evening, around 0330 and 0500 UT there were intensity enhancements to the north and northeast. At the same time there was a strong neutral wind to the west (Figure 54), which opposed thermal forcing, and a weak neutral wind toward the south, in the southeast. As on 29 February and 1 March, it appeared there was precipitation in a region of strong neutral motion brought about by ion drag. Later in the night, near 0730 UT there was a new feature, an intensity enhancement that occurred everywhere and had the same magnitude everywhere. There was a weak neutral velocity to the north and to the east. The uniformity of this emission feature and its location outside a region of

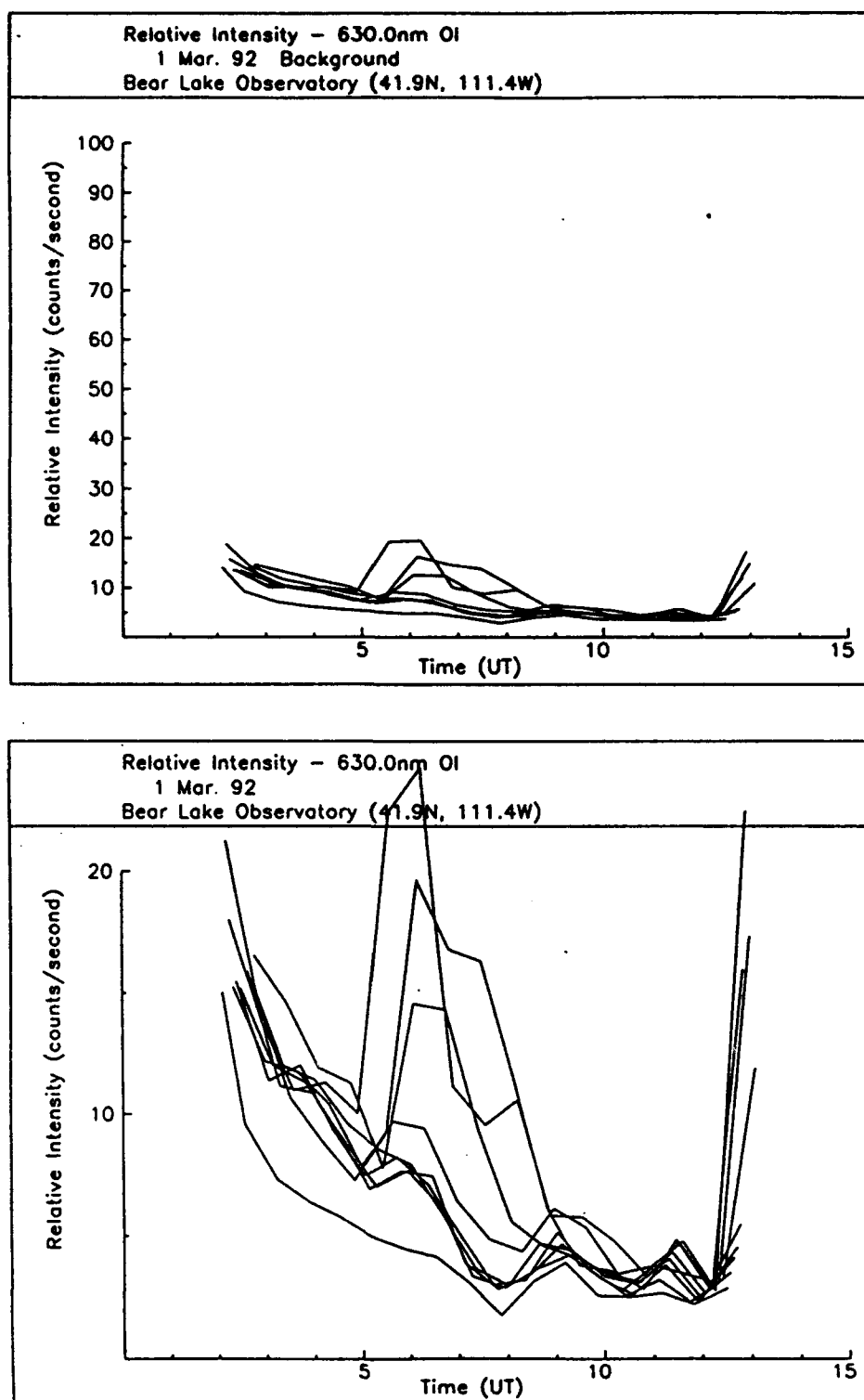


Fig. 51. Relative background (top) and O(I D) (bottom) intensities observed near 250 km from Bear Lake Observatory on 1 Mar 92.

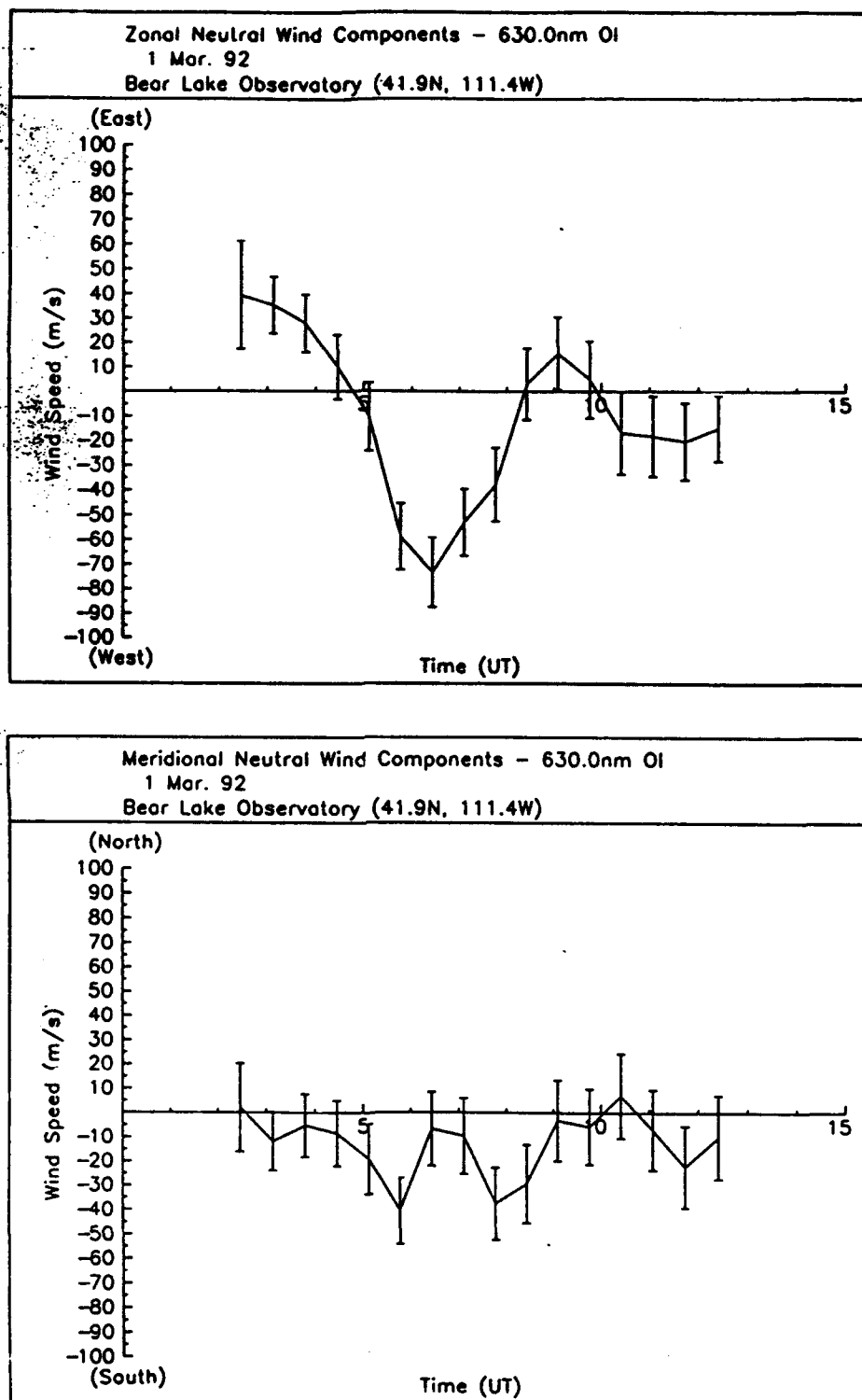


Fig. 52. Zonal (top) and meridional (bottom) neutral wind components observed near 250 km from Bear Lake Observatory on 1 Mar 92.

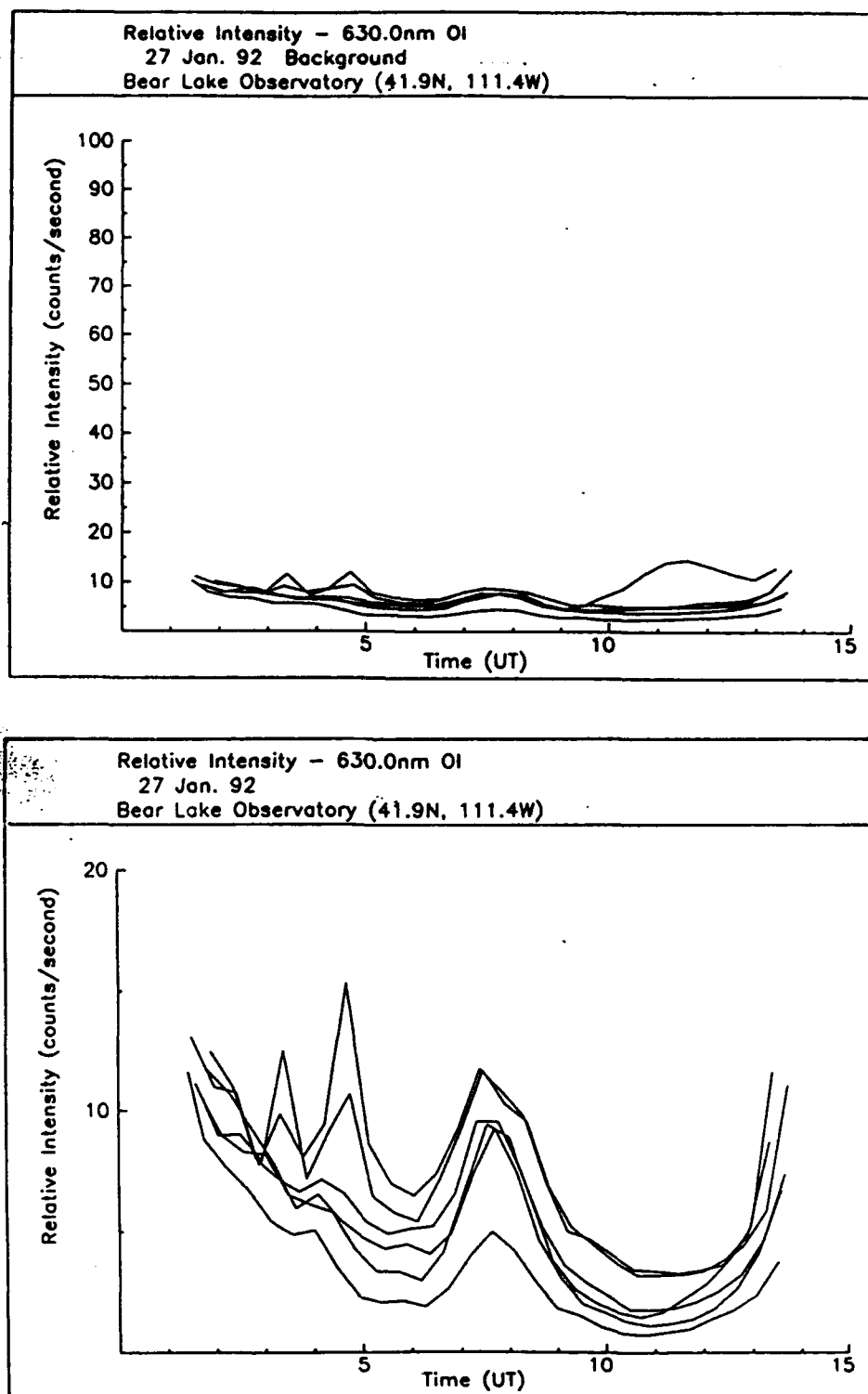


Fig. 53. Relative background (top) and O(¹D) (bottom) intensities observed near 250 km from Bear Lake Observatory on 27 Jan 92.

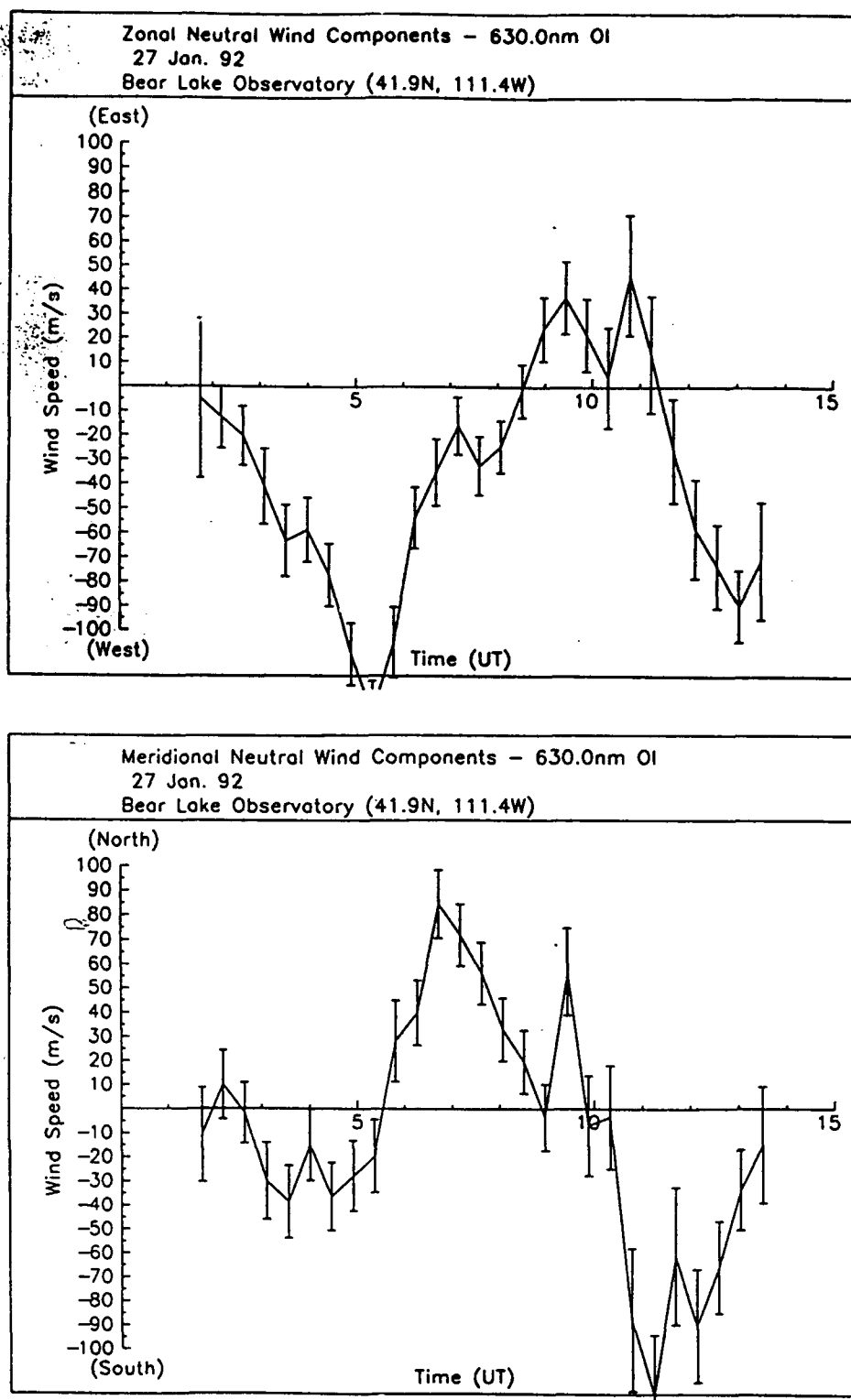


Fig. 54. Zonal (top) and meridional (bottom) neutral wind components observed near 250 km from Bear Lake Observatory on 27 Jan 92.

strong neutral motion suggest that this may be a SAR arc instead of auroral particle precipitation. However, it would have to be very extensive.

We have looked at eight days of 6300 Å data. Of these eight, only one resembled totally quiet magnetic conditions. This is a bit surprising, but also rather exciting because future observations may exhibit a lot of magnetic activity, leading to a greater understanding of the effects of auroral excitation in the mid-latitudes.

7.3 Instrumental Drift

A sharp drift, corresponding to a movement of several bins, in the calibration lamp peak position during the first hour or two of observation often characterizes the data from our instrument. This has been attributed to the fact that the high voltage is not turned on to the IPD control box during the day and allows the components to cool off. This was described earlier to be a safety measure designed to eliminate the possibility of turning the detector on during the day. While this is a desirable precaution, it also allows the components to cool off during the day. As the instrument warms up when turned on after dark, the focus and scale size of the image could be affected by the rapid change in temperature.

The fact that the calibration lamp peak drifts in this manner early in the evening eliminates the data from this period because the offsets calculated relative to those calibration peaks cannot reasonably be included in the average offset calculation. If we simply interpolated the fitted curve representing the zero-velocity back to the earlier times, we cannot be confident that the data peaks were not equally affected by the sharp drift. Data that were collected during periods when the high voltage was turned on an hour or more before data collection began do not display this drift, and lend credibility to this diagnosis.

7.4 Zenith Winds

The thickness of the emission layer is assumed to be constant. Because the zenith measurement is made perpendicular to the emitting layer, the number of emitting molecules in the integrated column is less by a factor of 3 to 4 than when the emission layer is viewed at a 30° elevation angle. This is called the Van Rhijn effect. The resulting uncertainties in the zenith measurements are two times greater, making it much less reliable as a measurement of the zero-wind position than the zero found by averaging of the opposite pairs of measurements.

The data showed this clearly. When plotted against the zero positions found by averaging opposite pairs of measurements, there were large deviations in the zenith position while the opposite pairs seemed to follow each other closely. Since these are all averaged to determine the final zero position, the calculated baseline much more closely resembles the opposite pairs than the zenith.

The vertical wind speeds which result from using the final zero-velocity baseline are often on the order of 50 to 100 m/s. It is very unlikely that these are actual winds. Rather, it is a reinforcement for the need for a longer integration time in the zenith to reduce the uncertainty to values comparable to the other directions. However, the greater uncertainty does not fully explain these large vertical winds.

In the long term, it is possible that our zenith mirror might come out of alignment. A tilt in the instrument or the zenith mirror system should be apparent in the zenith peak positions. The zenith winds will correlate well with the horizontal wind in the direction of the tilt. Such a correlation is not seen.

If the uncertainty on the zenith can be improved by increasing the integration time, it should be checked often to ensure that on average the zenith Doppler shift lies midway between Doppler shifts obtained from opposite cardinal directions. If it does not, this might also indicate that the mirrors are out of alignment, or that such strong vertical winds really do exist. These winds need further examination.

CHAPTER 8

OH INTENSITY ANALYSIS

8.1 Background Intensity

The two major contributors to the background present in the total measured signal are stellar emissions and the airglow continuum from NO_2 . Because each of these sources represents a continuum, there should not theoretically be any structure associated with them, and they should appear as a line at constant intensity across each individual interferogram. The height of the background is calculated in the analysis by averaging several points on both sides of the peak in the vicinity of half a free spectral range away. An example of the calculated background intensity for 8430 \AA OH is shown in Figure 55.

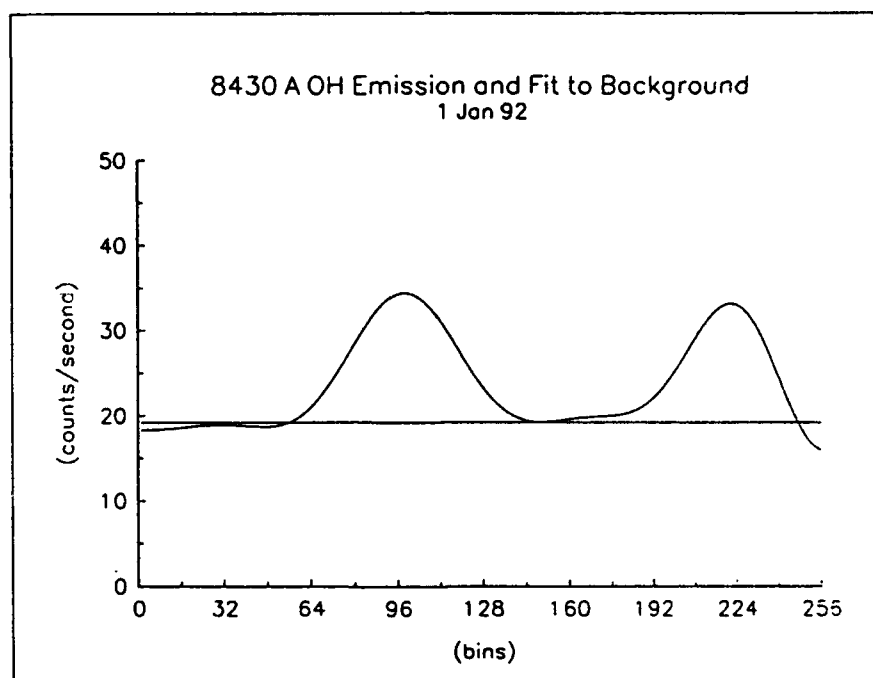


Fig. 55. The background intensity at 8430 \AA .

An accurate estimate of the background intensity is necessary for the calculation of the relative intensity of the emission, which is found simply by subtracting the background from the height of the emission peak. For these two emissions, the background is usually flat after the flat-field correction is applied. Hence the background is fitted with a horizontal line.

The intensity calculated from the Fabry-Perot data in the manner above is a relative intensity because the instrument has not been compared to a calibration source or to the output from a calibrated instrument. However, we do know that the 8430 Å line represents 10% of the total intensity [Espy, private communication, 1992], which is roughly 730 Rayleighs for the whole (6,2) OH band. Thus, 10 counts per second corresponds to approximately 50 Rayleighs. By taking into account the difference in quantum efficiency, 10 counts per second at 6300 Å corresponds to approximately 100 Rayleighs.

8.2 Relative Intensities

The calculated relative intensities can be plotted for the observing period to examine the time variation of the emission due to waves, winds, chemical changes or magnetic activity. The intensity variation can also be useful in determining the presence and extent of cloud cover. For thick clouds the airglow intensity can be reduced to 50% or 25% of its usual value.

In the initial analysis of OH relative intensities we found that there was an obvious correlation between time variations seen in the OH intensity and the variation seen in the continuum background emission. This is shown for 5 February 1992 in Figure 56. The variation observed in the background was about one quarter to one fifth of the magnitude of the variation seen in the OH emission. The possibility of other OH emissions falling within the passband of the filter and causing this behavior was explored and ruled out. While there are several lines which are close enough in wavelength to be

the culprit, their intensity was nearly 500 times weaker [Espy, private communication, 1992] than the emission necessary to cause such a large-scale change in the background continuum.

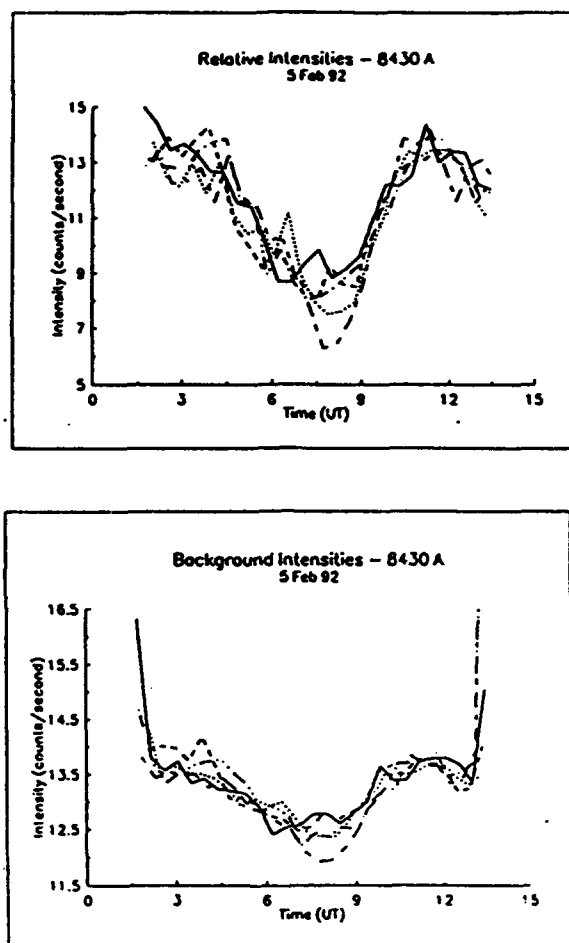


Fig. 56. Intensity and background variations for 5 Feb 92.

The background has two contributions. The first is starlight. The second is most likely from the NO_2 continuum. This is the part that would vary with the OH intensity. The NO_2 continuum arises from



[Chamberlain, 1961]. The OH emission, as shown earlier, arises from



but the O_3 in turn arises from



which is the rate limiting reaction. Thus, both emissions depend on the atomic oxygen density. The contribution from the continuum will be proportional to the 10-Å width of the passband filter.

8.3 Intensity Comparisons

To gain confidence in the relative intensity results, comparisons were performed with both an All-Sky Imaging system and a Bomen Michelson interferometer. These two instruments along with the Fabry-Perot take simultaneous measurements of OH intensities from the Bear Lake Observatory. None of these three instruments has been formally calibrated so that the intensities calculated by all three are relative intensities. The nights we have chosen for comparison, 5 and 6 February 1992, were selected because they were known to be relatively free of cloud cover.

8.3.1 The All-Sky Imager

The all-sky imager located at Bear Lake, operated by Gary Swenson of Lockheed, collects light radiated from horizon to horizon (180° FOV) through a wide spectral band, taking an image approximately every 4 minutes. The nightglow spectrum is filtered to eliminate all wavelengths shorter than 750 nm, with the upper limit being the high end of the CCD (charge-coupled device) response near 930 nm. It is also "notched" to eliminate a contribution from O_2 near 865 nm. The spatial resolution is determined by the CCD array, which has 1024×1024 pixels. However, the pixels are grouped 2×2 giving rise to an effective array of 512×512 pixels. Each pixel has a very large dynamic range. An image taken on 5 Feb 92 is shown in Figure 57. A small amount of wave-like structure is visible on the right side of the image (to the east).

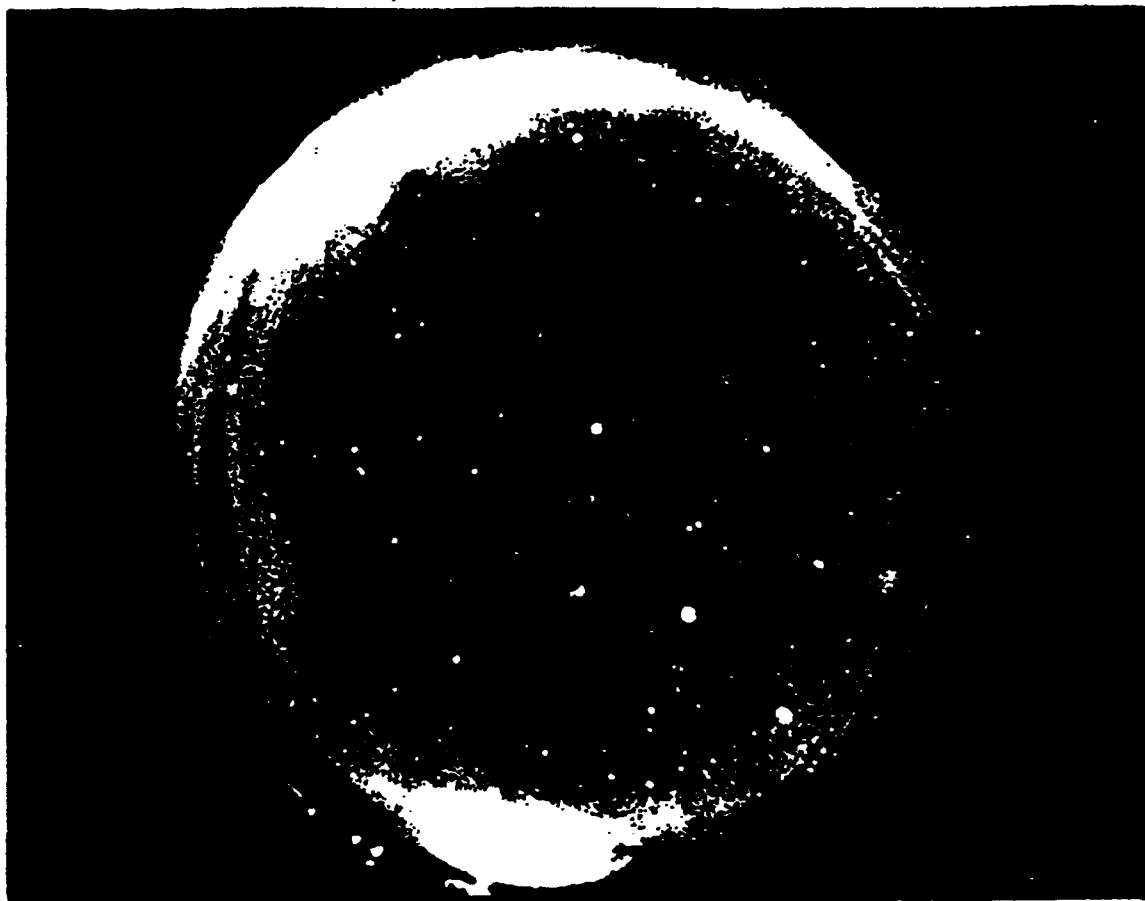


Fig. 57. Image taken by an All-sky imager at the Bear Lake Observatory on 5 Feb 92 [Photo compliments of Mike Taylor].

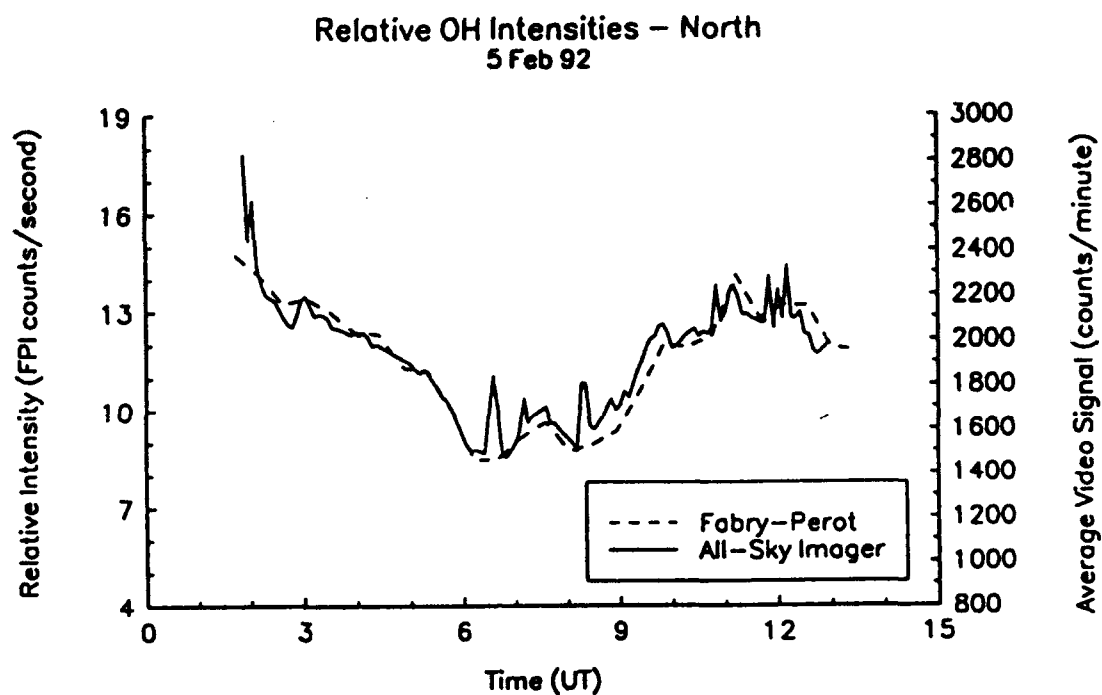
These images include many OH bands and the atomic oxygen lines at 7774 \AA and 8446 \AA , in contrast to the single emission line observed with the IFPI. As a result of including many bands, the observed intensity is much larger. Because we are only interested in a relative variation, a good comparison can be made.

To get the data from the all-sky images in a form useful for comparison, Mike Taylor of USU calculated where each of the Fabry-Perot observation points, including the zenith, falls on the all-sky images. After pinpointing these positions, he calculated the average intensity of an area 11×11 computer pixels wide around the determined position. These intensities were then plotted as a function of time for each of the Fabry-Perot positions, allowing a comparison between the two. The results are shown in Figure 58, a through l. Overall we found good correlation in each of the positions with many of the smaller-scale features evident in both measurements. This effectively confirms that most of the observed signal is from OH emissions. Because the time resolution of the all-sky camera is 4 minutes, while the time resolution of the Fabry-Perot is about 40 minutes, the all-sky data show more temporal variation than the Fabry-Perot data. (Data to the east, south, and southeast are omitted because the Fabry-Perot skipped these positions.)

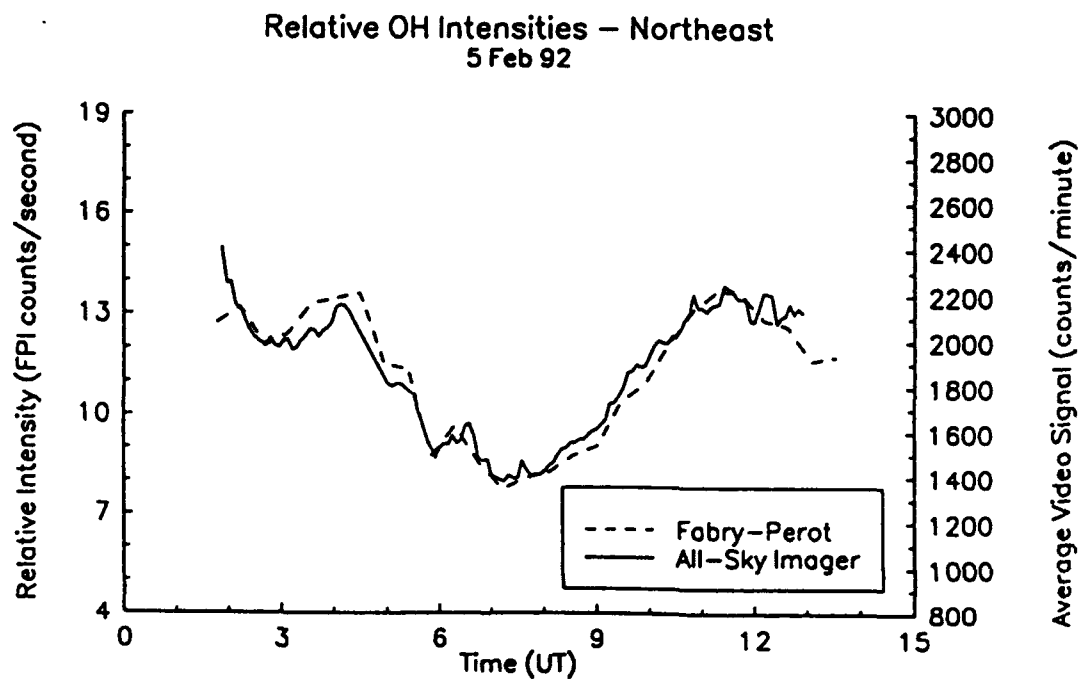
The geographic position of the individual structures seen in the all-sky images is known to a high degree of accuracy because structures are superimposed on a background of star constellations. An analysis program written by Visnja Taylor allows each image to be positionally calibrated to the known star positions.

8.3.2 The Bomen Michelson Interferometer

The Bomen Michelson interferometer at Bear Lake is operated by Pat Espy of USU. It covers the region from 1.00 to $1.67 \mu\text{m}$ with a resolution of 1 or 4 cm^{-1} , and observes the zenith with a field of view comparable to that of the IFPI. The integration time is approximately 4 minutes. Figure 59 shows the intensity comparison for 5 and 6 February 1992. To reduce the Bomen data, it is fitted with a synthetic spectrum. In Figure 59 the Bomen intensities, integrated over the 3-1 band near $1.5 \mu\text{m}$, are compared to the usual 6-2 $P_1(3)$ intensities at 8430 \AA observed with the IFPI. As with the all-sky imager, the agreement is very good.



(a)



(b)

Fig. 58. a and b Relative intensity comparison between the All-Sky Imager (solid curve) and the Fabry-Perot interferometer (dashed curve), 5 Feb 92.

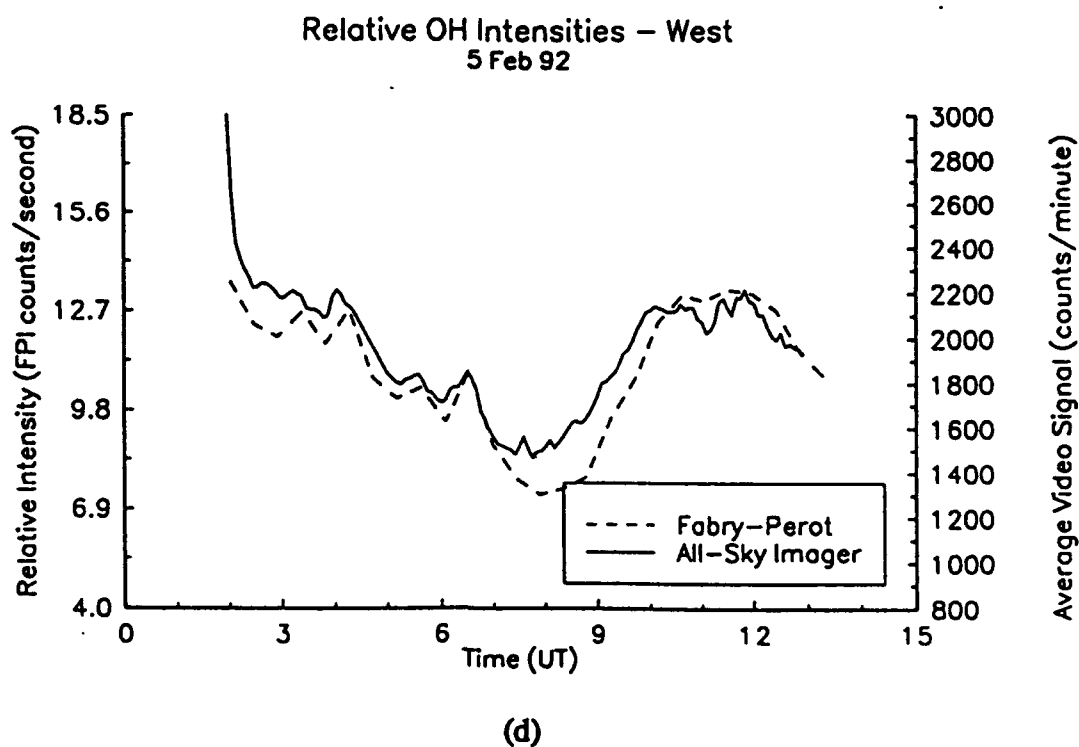
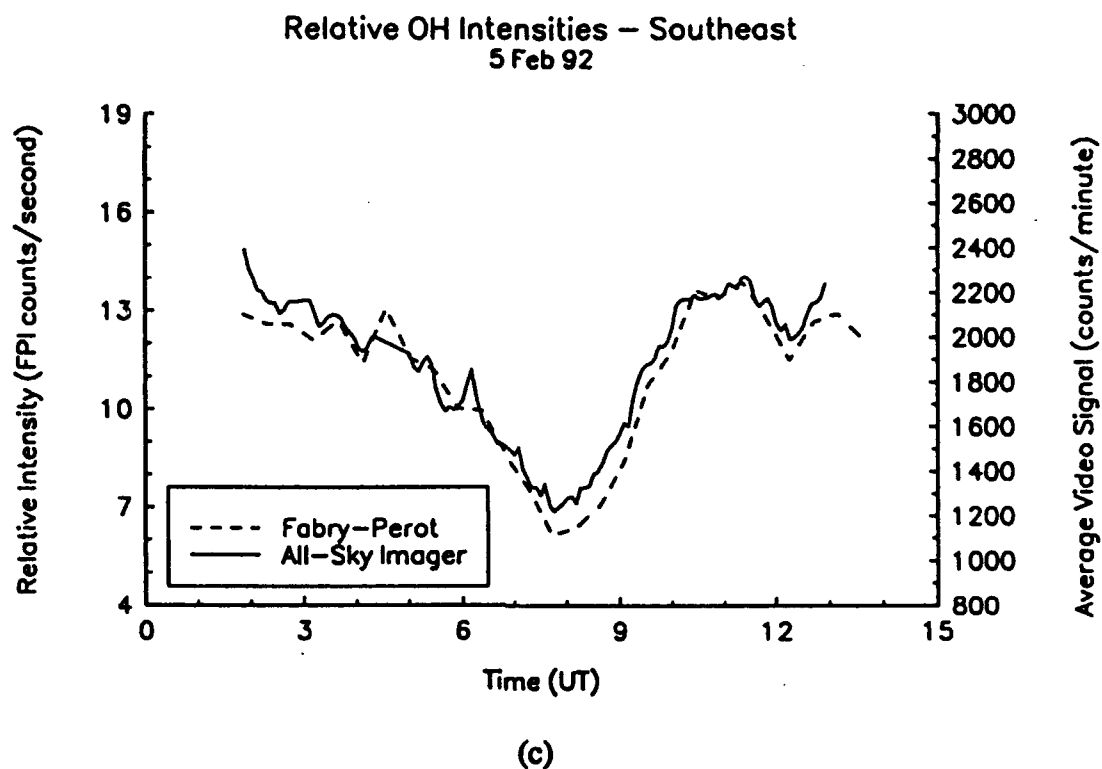
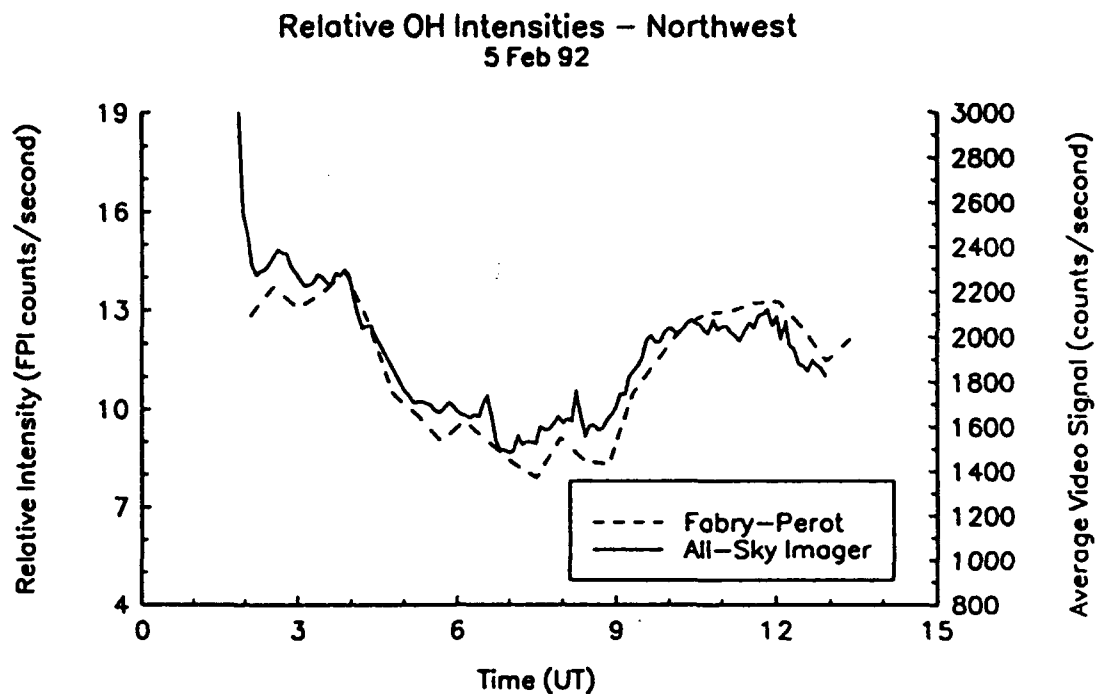
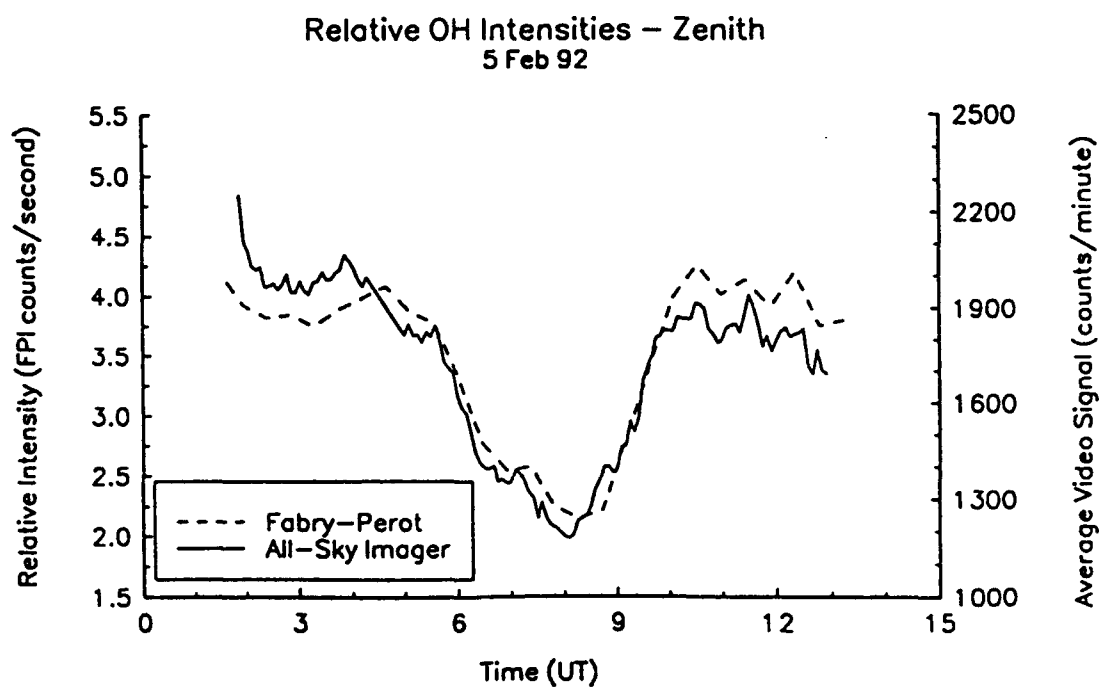


Fig. 58. c and d Relative intensity comparison between the All-Sky Imager (solid curve) and the Fabry-Perot interferometer (dashed curve), 5 Feb 92.

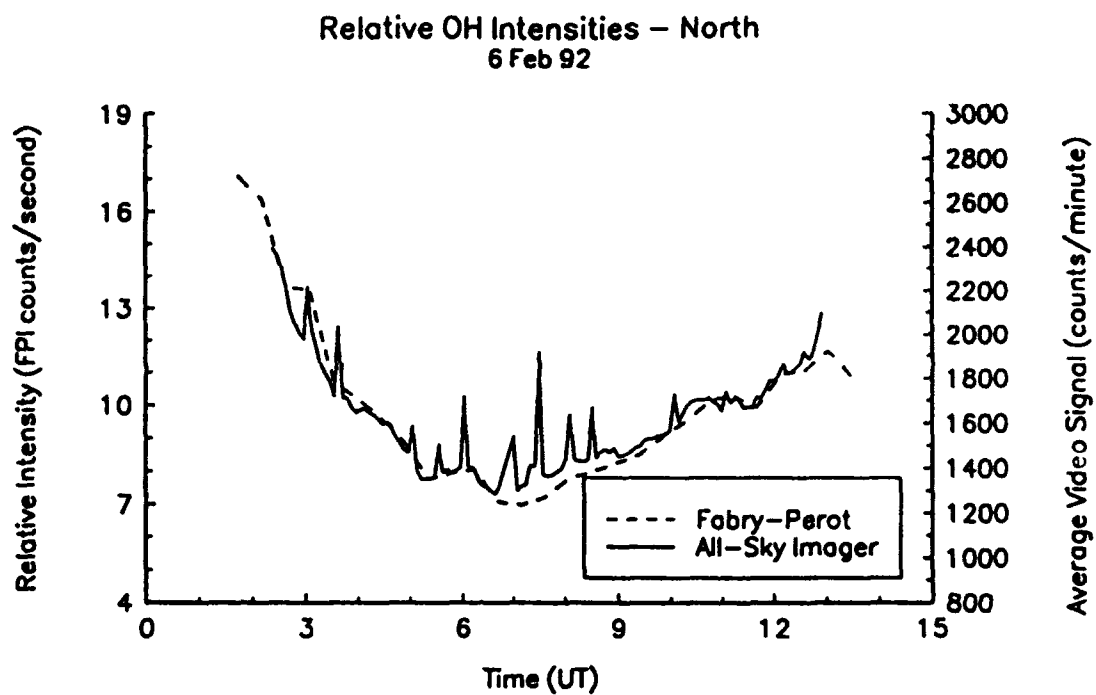


(e)

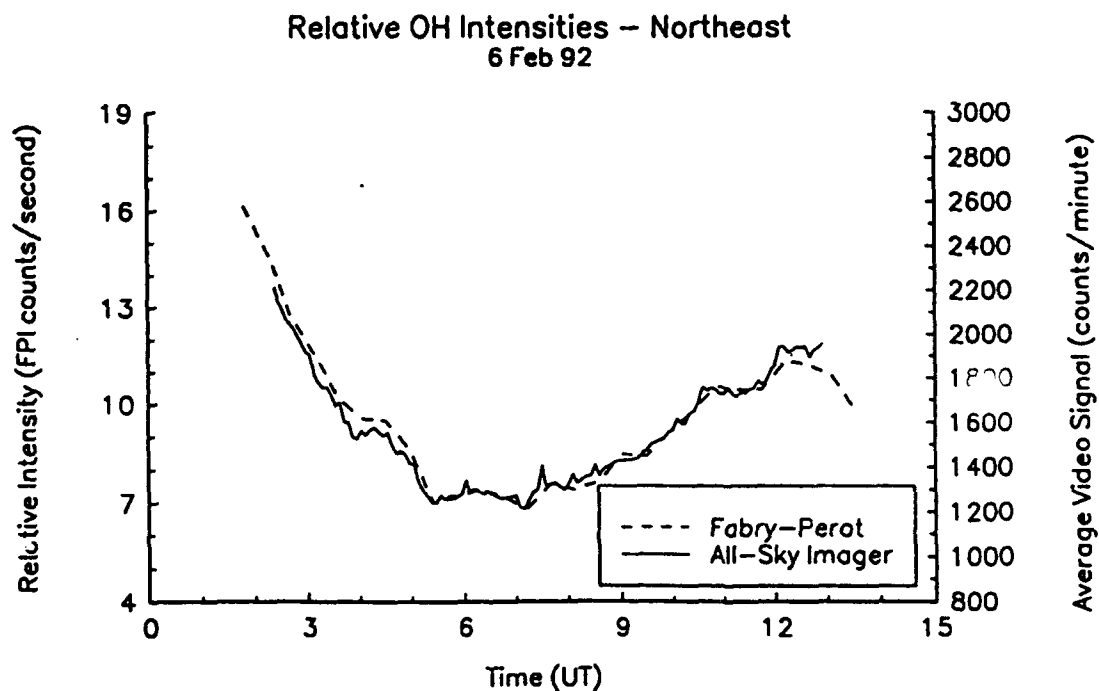


(f)

Fig. 58. e and f Relative intensity comparison between the All-Sky Imager (solid curve) and the Fabry-Perot interferometer (dashed curve), 5 Feb 92.

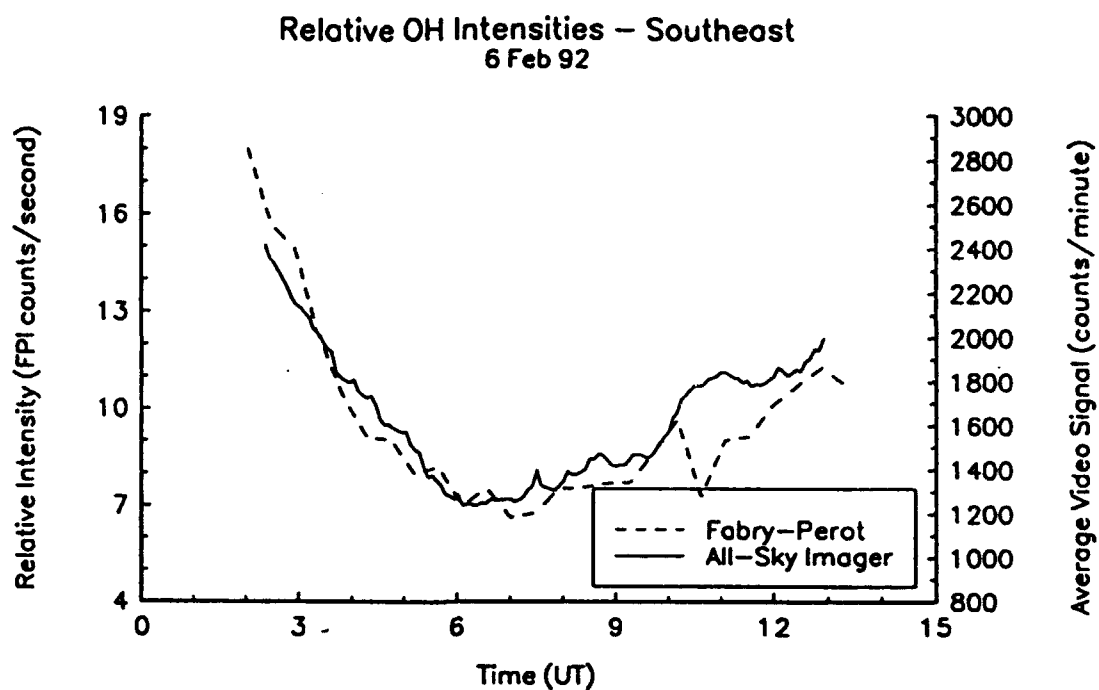


(g)

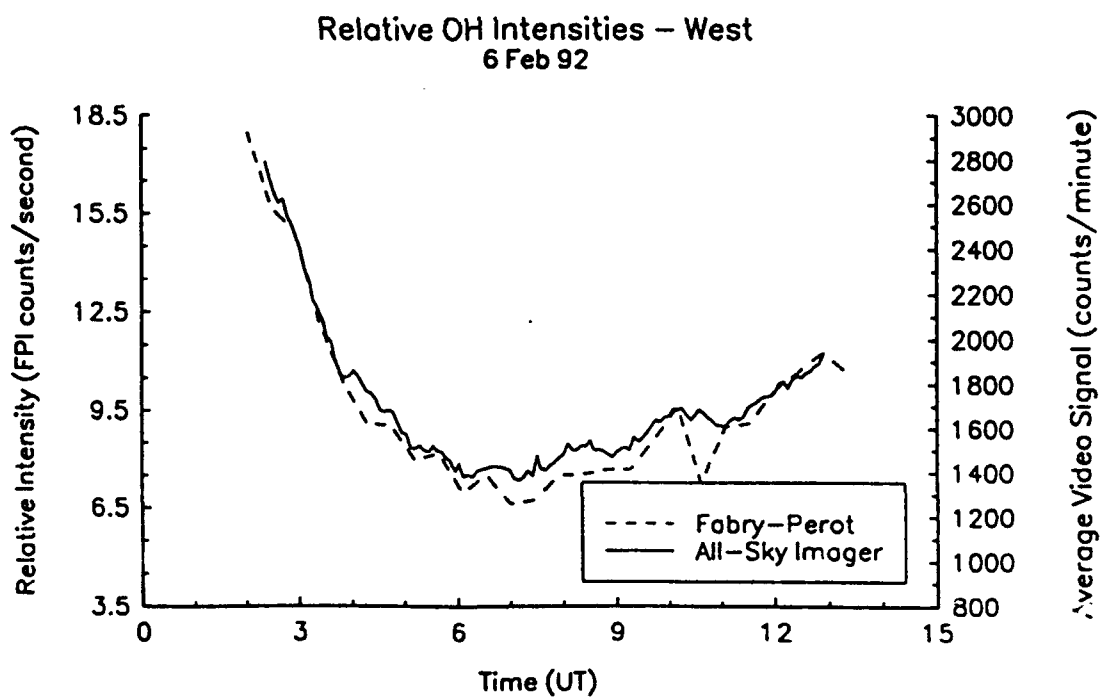


(h)

Fig. 58. g and h Relative intensity comparison between the All-Sky Imager (solid curve) and the Fabry-Perot interferometer (dashed curve), 6 Feb 92.



(i)



(j)

Fig. 58. i and j Relative intensity comparison between the All-Sky Imager (solid curve) and the Fabry-Perot interferometer (dashed curve), 6 Feb 92.

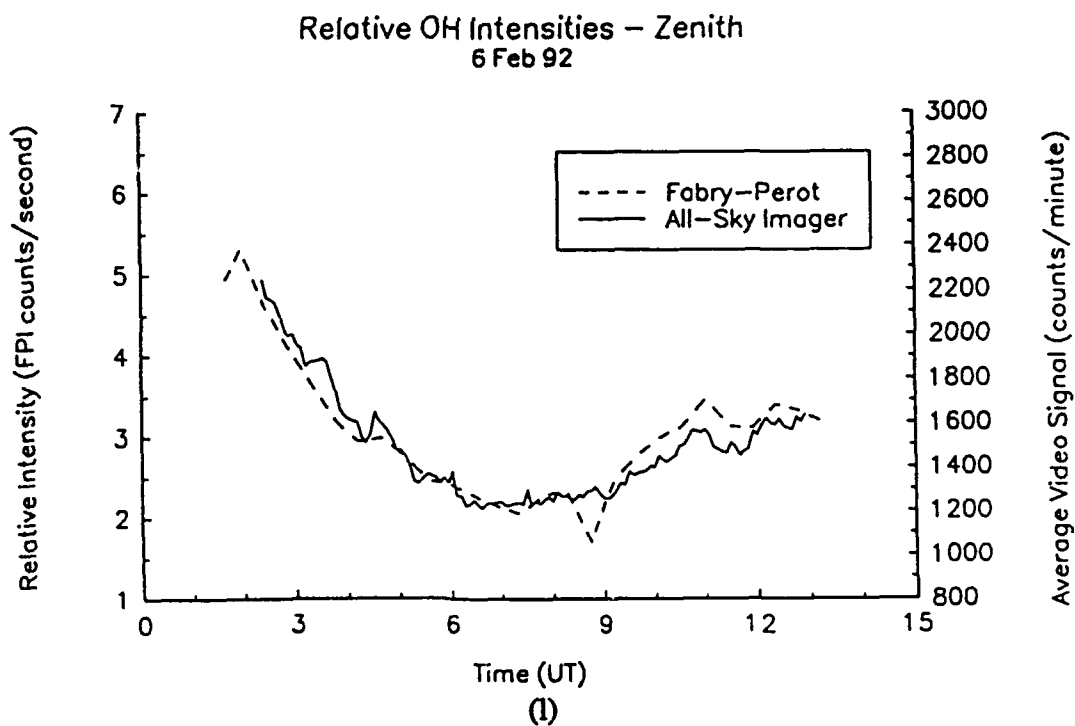
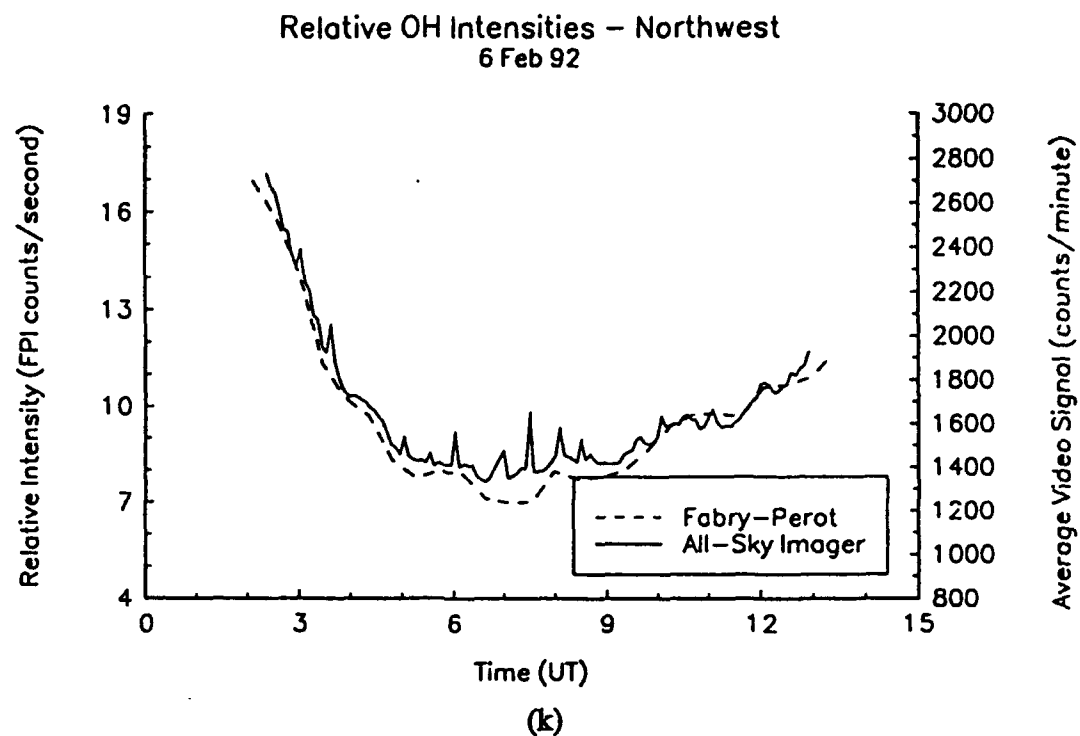


Fig. 58. k and l Relative intensity comparison between the All-Sky Imager (solid curve) and the Fabry-Perot interferometer (dashed curve), 6 Feb 92.

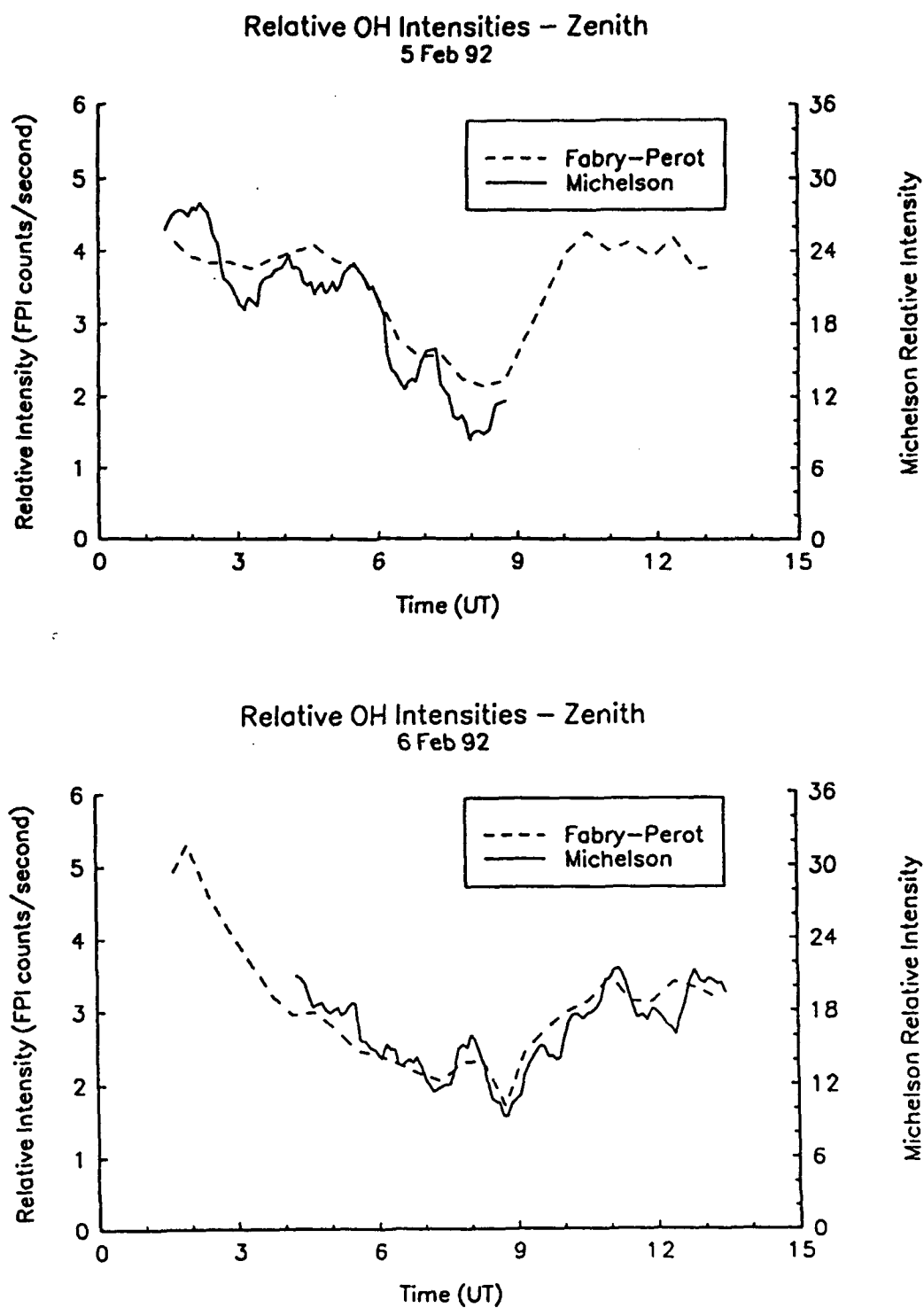


Fig. 59. Relative intensity comparison between the Bomem Michelson interferometer (solid curve) and the Fabry-Perot interferometer (dashed curve), 5 Feb 92 (top) and 6 Feb 92 (bottom).

CHAPTER 9

MESOSPHERIC TEMPERATURES

The temperature of the mesosphere is an important physical parameter of vital interest to studies on D-region ion chemistry and mesospheric dynamics. Chemical reaction rates are strongly temperature dependent [Meriwether, 1984]. Temperature measurements of atmospheric emissions have been made by many investigators who mostly study thermospheric emissions such as the 6300 Å O(¹D) where temperatures are on the order of a thousand degrees. Precise measurements become more difficult near the mesopause where temperatures may be as low as 180°K, which significantly shrinks the width of the emission profile. A careful correction has to be made for the instrumental width. The other difficulty in finding the true width of the 8430 Å emission is whether the hyperfine structure (doublet) has been exactly superimposed or whether they are offset. This possibility will need to be accounted for in the analysis.

Much of the temperature work that has been done previously to find OH temperatures involves finding rotational temperatures rather than the kinetic temperature. Rotational temperatures are calculated using the ratio of the observed intensities of two or more individual OH rotational lines. This procedure can be accomplished with limited resolution instruments such as the Bomen Michelson interferometer since it only requires relative intensities rather than an accurate line width. Many papers have been published using this technique, including Pendleton *et al.* [1988].

9.1 Recovering the Emission Line

Earlier it was said that the shape of the source profile will be primarily Gaussian. Because the source emission passes through the instrument to be recorded, the instrumental function is convolved with the Gaussian. Theoretically, the instrument function can be measured and numerically deconvolved from the recorded profile, giving

a resulting shape which represents the source function; however, a better method is to try to reproduce the measured profile by convolving the measured instrumental shape with the analytic function describing the source (a Gaussian) and adjusting the parameters of the Gaussian until the measured emission profile is matched. The steps in this process are briefly outlined below.

9.1.1 Find the Instrument Profile

The single-mode He-Ne laser can be used to measure the instrument profile of the Fabry-Perot. This is possible because of the almost negligible Doppler broadening of the laser emission profile, due to the spectral purity of its output. The profile produced by the laser should consist solely of the broadening functions due to the reflective properties of the plates, the surface roughness defects, and the aperture function [Roble, 1969].

9.1.2 Create the Analytic Function (Gaussian)

The second step in determining the temperature will be to write a program which produces the analytic function: the Gaussian which will represent the emission profile. The width of this function should be a variable, i.e. depend on temperature. For the 8430 Å data the program should allow for two Gaussian shapes separated by some constant which is also a variable, to represent the hyperfine doublet.

9.1.3 Convolve the Laser Profile and the Double Gaussian

The final step will be to convolve the measured instrument profile with the double Gaussian and then compare the new shape to the Fabry-Perot measured profile. The best fit will be obtained by varying the width of the individual Gaussian shapes and adjusting the separation constant between the two Gaussian shapes until the convolved profile matches the measured profile. The temperature is then determined from the Gaussian which gives the best fit.

9.1.4 Comparison of Fabry-Perot and Michelson Temperatures

The Fabry-Perot temperature analysis should be compared to rotational temperatures obtained from the Michelson interferometer. This may be essential to find the separation of the hyperfine lines. It will certainly be interesting to compare the Doppler and rotational temperatures.

9.2 Current Progress

At present, although the single-mode He-Ne laser is available, the instrument profile has not been measured. The groundwork has been laid for the eventual analysis, however, because the current analysis programs create the smoothed profile of the measured emission and find the background, which can then be subtracted.

We can calculate the approximate contribution of the instrument profile and hyperfine structure to the total measured width using some basic theory. The purely Doppler line shape will have a full width at half maximum proportional to the square root of the neutral gas temperature [Roble, 1969], according to

$$S = 7.16 \times 10^{-7} \lambda_0 \sqrt{\frac{T}{M}} \quad (9.1)$$

where λ_0 is the emission wavelength in Angstroms, T is temperature in degrees Kelvin, and M is the molecular weight of OH (17).

At 8430 Å, using T=180 K, the full width is ~19.6 mÅ, and for 6300 Å at 1000 K a full width of 35 mÅ is calculated. These of course are the widths of the emission profile calculated assuming no instrumental broadening or affects of hyperfine structure in the OH. The HWHH can be determined from the Fabry-Perot data using equation 9.2.

$$HWHH(m\text{\AA}) = \frac{HWHH(bins) \lambda^2}{FSR(bins) 2t} \quad (9.2)$$

At 8430 Å the average measured half width is approximately 21.75 bins. Using a free spectral range of 148 bins, the full width in mÅ is ~51.0 mÅ. At 6300 Å the

average measured half width is approximately 24.4 bins, which translates to a full width of 43.0 mÅ.

At 6300 Å and 1000 K the full width at half maximum is expected to be 35 mÅ, where it is observed to be 43 mÅ. The difference suggests that the instrumental function adds 8 mÅ at this wavelength. Assuming the width added by the instrumental function is proportional to wavelength, then it would become 11 mÅ at 8432 Å. The calculated full width at half maximum for 180 K – a very low temperature – is 20 mÅ, whereas the observed is 51 mÅ. This is a very big discrepancy. After accounting for the instrumental function in this crude way, it suggests that the spectrum is roughly twice as wide as expected. Possible explanations are that the OH is very poorly focused on the photocathode of the IPD or that the two parts of the doublet appear separated by an amount approaching 20 mÅ. It could not, however, be quite that amount or the OH spectrum would have a much flatter peak. There would be a significant separation.

Knowledge of the temperature at these altitudes along with its variability would lead to a much greater understanding of the dynamics of the region, and possibly the opportunity to observe planetary wave activity.

CHAPTER 10

POTENTIAL FOR FUTURE RESEARCH

There are many possibilities for future research since this thesis embodies only the very beginnings of analysis done on the Fabry-Perot data from the Bear Lake Observatory. Not only will much additional information be gleaned from the 8430 Å OH data from the mesopause region and the 6300 Å O(¹D) data from the thermosphere, the variable filter capability will allow study of several emissions originating at different altitudes such as O₂ atmospheric bands at 95 km, which can lead to information about vertical structure. A partial list of additional research possibilities is given here.

1. A thorough comparison of the winds observed during different seasons should be done. The winds near 86 km should show a substantial amount of seasonal variation, because tides, gravity waves, and planetary waves all have seasonal variation. In addition to the winds, the relative intensities and temperatures can be compared to get a fuller picture of the dynamics of the region as a function of season.

2. A consistent method for discerning the presence of clouds in the Fabry-Perot wind data needs to be developed.

3. Two similar Fabry-Perots are operating in Calgary (~51° N, -114° W) and Saskatoon (~52° N, -106° W). Winds from these sites could be compared to winds observed at Bear Lake and examined for similarities and differences. Some similarity in the large-scale wind patterns should exist between the three sites due to their general proximity. However, considerable differences are expected because of the latitudinal dependence of tides, proximity to auroral forcing, and influence of orography on gravity-wave generation.

4. Currently the UARS satellite is collecting a vast amount of data. Some of these data are intensity and wind measurements derived from the OH Meinel (8,3)

rotation band, which the satellite maps as a function of latitude. The Fabry-Perot measurements of velocity and relative intensity, collected as a function of time, could be compared to the UARS data.

5. A comparison of winds obtained from emissions at different altitudes needs to be done. A good starting point might be the O₂ atmospheric band that occurs near 95 km. A filter is already installed in the Bear Lake instrument, but we have not yet detected any significant emission. Another possibility includes the 5577 Å green line from atomic oxygen at 96+/-2 km [Donahue *et al.*, 1973]. These measurements can be combined to yield a height profile from which it should be possible to calculate the vertical wavelengths of upward propagating waves. Knowledge of the vertical wavelength will allow the identification of tidal modes. The study of upward propagating waves will add to our knowledge of energy transport through the region.

6. Complete a study of the effects of stratospheric warmings ("mesocools") and their propagation in the mid-latitudes. These are possibly related to the presence of planetary waves, which theoretically can be detected using Fabry-Perot temperature measurements.

7. Relate the presence of gravity waves in the Fabry-Perot data to orographic features, weather phenomena, and possibly magnetic activity.

8. A Doppler Imaging System can be used to construct the two-dimensional velocity field. This can be correlated to the wind field derived using the Fabry-Perot and can be used to examine the uniformity of the wind field.

9. Using the Fabry-Perot, study the affects of magnetic activity on 6300 Å intensity and neutral winds. Correlate the Kp index to observed features. Look for supporting evidence for particle precipitation. See how the wind varies in different parts of the sky. A Meridional Imaging Spectrometer (MIS) can be used to determine the

presence of SAR arcs and other emissions and to determine the origin of features seen in the Fabry-Perot data.

10. Develop the kinetic temperature analysis capability. Compare OH rotational temperatures from the Bomen Michelson to the kinetic temperatures found using the Fabry-Perot.

11. Lidar observations from USU will provide knowledge of the region below 87 km. This will provide altitude continuity for the study of upward propagating waves, i.e., when they deposit energy in the stratosphere or lower in the mesosphere, or when they pass through to 87 km.

12. Compare thermospheric winds deduced by the FPI and the Dynasonde. With the latter, winds are determined from the altitude of the F-layer peak.

REFERENCES

- Andrews, D. G., J. R. Holton, and C. B. Leovy, *Middle Atmosphere Dynamics*, Academic Press Inc., New York, 1987.
- Aruliah, A., The synoptic variety of the thermosphere and mesosphere winds observed using a Fabry-Perot interferometer, Ph. D. Thesis, University of London, 1992.
- Baker, D. J., Studies of Atmospheric Infrared Emissions, AFGL-TR-78-0251, AFGL, Hanscom AFB, Massachusetts, 1978.
- Baker D. J., and A. T. Stair Jr., Rocket Measurements of the Altitude Distributions of the Hydroxyl Airglow, *Physica Scripta*, 37, 611-622, 1988.
- Beer, T., *Atmospheric Waves*, John Wiley & Sons, New York, 1974.
- Bernard, R., A comparison between meteoric radar and incoherent scatter measurements in the lower thermosphere, *Radio Sci.*, 9, 295-300, 1974.
- Bevington, P. R., *Data Reduction and Error Analysis for the Physical Sciences*, McGraw-Hill Book Co., New York, 1969.
- Chamberlain, J. W., *Physics of the Aurora and Airglow*, Academic Press, New York, 1961.
- CIRA 1972, *COSPAR International Reference Atmosphere 1972*, Akademie-Verlag, Berlin, 1972 (Committee for the COSPAR International Reference Atmosphere (CIRA) of COSPAR Working Group 4).
- Clark, R. R., and J. E. Salah, Propagation of the solar semidiurnal tide in the mesosphere and lower thermosphere at mid-latitudes, *J. Geophys. Res.*, 96, 1129-1133, 1991.
- Clough, S. A., F. X. Kneizys, L. S. Rothman, and W. O. Gallery, Atmospheric Spectral Transmittance and Radiance: FASCOD1B, *SPIE Vol. 277 Atmospheric Transmission*, 152-166, AFGL, Hanscom AFB, Massachusetts, 1981.
- Donahue, T. M., B. Guenther, and R. J. Thomas, Distribution of atomic oxygen in the upper atmosphere deduced from Ogo 6 airglow observations, *J. Geophys. Res.*, 78, 6662-6689, 1973.
- Forbes, J. M., Atmospheric Tides 1. Model description and results for the Solar Diurnal Component, *J. Geophys. Res.*, 87, 5222-5240, 1982.

- Forbes, J. M., and F. Vial, Monthly simulations of the solar semidiurnal tide in the mesosphere and lower thermosphere, *J. Atmos. Terr. Phys.*, **51**, 649-661, 1989.
- Forbes, J. M., and M. E. Hagen, Diurnal propagating tide in the presence of mean winds and dissipation: A numerical investigation, *Planet. Space Sci.*, **36**, 579-590, 1988.
- Franke, S. J., T. Beatty, D. Thorsen, C. H. Liu, C. S. Gardner, F. L. Roesler, and J. Harlander, Simultaneous Na lidar and HF radar observations of vertical velocities in the mesosphere above Urbana, Illinois, *Geophys. Res. Lett.*, **17**, 69-72, 1990.
- Gardner, C. S., M. S. Miller, and C. H. Liu, Rayleigh LIDAR observations of gravity wave activity in the upper stratosphere at Urbana, Illinois, *J. Atm. Sci.*, Feb. 1988.
- Geller, M. A., Dynamics of the middle atmosphere, *Space Sci. Rev.*, **34**, 359-375, 1983.
- Hauchecorne, A., and M. L. Chanin, A mid-latitude ground-based lidar study of stratospheric warmings and planetary wave propagation, *J. Atmos. Terr. Phys.*, **44**, 577-583, 1982.
- Hauchecorne, A., and M. L. Chanin, Mid-latitude LIDAR observations of planetary waves in the middle atmosphere during the winter of 1981-1982, *J. Geophys. Res.*, **88**, 3843-3849, 1983.
- Hecht, E., *Optics*, Addison-Wesley Publishing Co., Reading, Massachusetts, 1987.
- Hernandez, G., Lower-Thermosphere Temperatures Determined From the Line Profiles of the OI 17,924-K (5577Å) Emission in the Night Sky 1. Long-Term Behavior, *J. Geophys. Res.*, **81**, 5165-5171, 1976.
- Hernandez, G., *Fabry-Perot Interferometers*, Cambridge University Press, Cambridge, UK, 1986.
- Hernandez, G., and J. L. Smith, Mesospheric wind determination and the $P_1(2)_{c,d}$ lines of the $X_2\Pi$ OH (8-3) band, *Geophys. Res. Lett.*, **11**, 534-537, 1984.
- Hernandez, G., and R. G. Roble, Thermospheric dynamics investigations with very high resolution spectrometers, *Appl. Opt.*, **18**, 3376-3385, 1979.
- Holton, J. R., *An Introduction to Dynamic Meteorology*, Academic Press Inc., New York, 1979.
- Hooke, W. H., *Rossby-Planetary Waves, Tides, and Gravity Waves in the Upper Atmosphere*, National Academy of Sciences, Washington, D.C., 1977.

- Kato, S., *Dynamics of the Upper Atmosphere*, D. Reidel Publishing Co., Boston, 1980.
- Kazimirovsky, E. S., and E. I. Zhovty, Mid-latitude seasonal behaviour of tides near the mesopause level, *J. Atmos. Terr. Phys.*, 51, 683-687, 1989.
- Killeen, T. L., P. B. Hays, B. C. Kennedy, and D. Rees, Stable and rugged etalon for the Dynamics Explorer Fabry-Perot interferometer 2. Performance, *Applied Optics*, 21, 3903-3912, 1982.
- Le Texier, H., S. Solomon, and R. R. Garcia, Seasonal variability of the OH Meinel bands, *Planet. Space Sci.*, 35, 977-989, 1987.
- Lindzen, R. S., *Dynamics in Atmospheric Physics*, Cambridge University Press, Cambridge, 1990.
- Liou, K., *An Introduction to Atmospheric Radiation*, Academic Press, Inc., San Diego, California, 1980.
- Lloyd, N. D., Measurement of neutral thermospheric winds using ground-based Fabry-Perot interferometers, Ph. D. Thesis, University of London, 1985.
- Manson, A. H., C. E. Meek, H. Teitelbaum, F. Vial, R. Schminder, D. Kurschner, M. J. Smith, G. J. Fraser, and R. R. Clark, Climatologies of semi-diurnal and diurnal tides in the middle atmosphere (70-110 km) at middle latitudes (40-55), *J. Atmos. Terr. Phys.*, 51, 579-593, 1989.
- McWhirter, I., D. Rees, and A. H. Greenaway, Miniature imaging photon detectors, II. An assessment of the performance of the resistive anode IPD, *J. Phys. E: Sci. Instrum.*, 15, 145-150, 1982.
- Meek, C. E., I. M. Reid, and A. H. Manson, Observations of mesospheric wind velocities, 1, *Radio Sci.*, 20, 1363-1382, 1985.
- Meriwether, J. W., *Ground-Based Measurements of Mesosphere Temperatures by Optical Means, Middle Atmosphere Handbook*, Vol. 13, Edited by R. A. Vincent, University of Illinois, Urbana, 1984.
- Meriwether, J. W. Jr., A review of the photochemistry of selected nightglow emissions from the mesopause, *J. Geophys. Res.*, 94, 14629-14646, 1989.
- Nicholls, D. C., Hydroxyl rotational temperatures in the airglow, Ph. D. Thesis, University of Saskatchewan, Saskatoon, Canada, 1971.

- Pendleton, W., Jr., P. Espy, D. Baker, A. Steed, M. Fetrow, and K. Henriksen, Observation of OH Meinel (7,4) P_{1,2}(N''=13) transitions in the night airglow, *J. Geophys. Res.*, **94**, 505-510, 1988.
- Rees, D., I. McWhirter, P. A. Rounce, F. E. Barlow, and S. J. Kellock, Miniature imaging photon detectors, *J. Phys. E: Sci. Instrum.*, **13**, 763-770, 1980.
- Rees, D., T. J. Fuller-Rowell, A. Lyons, T. L. Killeen, and P. B. Hays, Stable and rugged etalon for the Dynamics Explorer Fabry-Perot interferometer 1. Design and construction, *Applied Optics*, **21**, 3896-3902, 1982.
- Rees, D., I. McWhirter, A. Aruliah, and S. Batten, Upper atmospheric wind and temperature measurements using imaging Fabry-Perot interferometers, In *World Ionosphere/Thermosphere Study, WITS HANDBOOK*, vol. 2, edited by C. H. Liu, SCOSTEP Secretariat, University of Illinois, Urbana, Illinois, 1989.
- Rees, D., A. Aruliah, T. J. Fuller-Rowell, V. B. Wickwar, and R. J. Sica, Winds in the upper mesosphere at mid-latitude: first results using an imaging Fabry Perot interferometer, *Geophys. Res. Lett.*, **17**, 1259-1262, 1990.
- Richmond, A. D., S. Matsushita, and J. D. Tarpley, Ionospheric current and field production, *J. Geophys. Res.*, **81**, 547-555, 1976.
- Roble, R. G., A theoretical and experimental study of the stable mid-latitude red arc (SAR-Arc), Ph. D. Thesis, University of Michigan, 1969.
- Salby, M. L., and R. G. Roper, Long-period oscillations in the meteor region, *J. Atm. Sci.*, **37**, 237-244, 1980.
- Taylor, M. J., and M. A. Hapgood, On the origin of ripple-type wave structure in the OH nightglow emission, *Planet. Space Sci.*, **11**, 1421-1430, 1990.
- Taylor, M. J., M. A. Hapgood, and P. Rothwell, Observations of gravity wave propagation in the OI (557.7 nm), Na (589.2 nm) and the near infrared OH nightglow emissions, *Planet. Space Sci.*, **35**, 413-427, 1987.
- Taylor, M. J., P. J. Espy, D. J. Baker, R. J. Sica, P. C. Neal, and W. R. Pendleton Jr., Simultaneous intensity, temperature and imaging measurements of short period wave structure in the OH nightglow emission, *Planet. Space Sci.*, **39**, 1171-1188, 1991.
- Teitelbaum H., F. Vial, A. H. Manson, R. Giraldez, and M. Massebeuf, Nonlinear interaction between the diurnal and semidiurnal tides: terdiurnal and diurnal secondary waves, *J. Atm. Terr. Phys.*, **51**, 627-634, 1989.

- Tolansky, S., *An Introduction to Interferometry*, John Wiley & Sons Inc, New York, 1955.
- Tsuda, T., S. Kato, T. Yokoi, T. Inoue, M. Yamamoto, T. E. VanZandt, S. Fukao, and T. Sato, Gravity waves in the mesosphere observed with the middle and upper atmosphere radar, *Radio Sci.*, 26, 1005-1018, 1990.
- Vallance Jones, A. V., Overview of auroral spectroscopy, In *Auroral Physics*, 463 pp., Edited by C. Meng, M. J. Rycroft, L. A. Frank, Cambridge University Press, Cambridge, 1991.
- Vincent, R. A., and I. M. Reid, HF Doppler measurements of mesospheric gravity wave momentum fluxes, *J. Atmos. Sci.*, 40, 1321-1333, 1983.
- Vincent R. A., T. Tsuda, and S. Kato, Asymmetries in mesospheric tidal structure, *J. Atmos. Terr. Phys.*, 51, 609-616, 1989.
- Volland, H., *Atmospheric Tidal and Planetary Waves*, Kluwer Academic Publishers, Dordrecht, The Netherlands, 1988.
- von Zahn, U., and H. Kurzawa, Near-Mesopause Temperatures at 69°N Latitude in late Summer, Proc. Ninth ESA/PAC Symposium on 'European Rocket and Balloon Programmes and Related Research,' *ESA SP291*, 63-77, 1989.
- Ware, G. A., OH rotational temperatures using optimal interferometric techniques, Ph. D. Thesis, Utah State University, 1980.
- Witt G., J. Stegman, B. H. Solheim, and E. J. Llewellyn, A measurement of the $O_2(b^1\Sigma_g^+ - X^3\Sigma_g^-)$ atmospheric band and the $OI(^1S)$ green line in the nightglow, *Planet. Space Sci.*, 27, 341-350, 1979.
- Yamamoto, M., T. Tsuda, and S. Kato, Gravity waves observed by the Kyoto meteor radar in 1983-1985, *J. Atmos. Terr. Phys.*, 48, 597-603, 1986.

APPENDICES

Appendix A. Bibliography

- Brasseur, G. and S. Solomon, *Aeronomy of the Middle Atmosphere*, D. Reidel Publishing Co., Dordrecht, Holland, 1984.
- Chapman, S. and R. S. Lindzen, *Atmospheric Tides*, D. Reidel Publishing Co., Dordrecht, Holland, 1970.
- Craig, R. A., *The Upper Atmosphere, Meteorology and Physics*, Academic Press Inc., New York, 1965.
- Forbes, J. M., Atmospheric Tides 2. The solar and lunar semidiurnal components, *J. Geophys. Res.*, 87, 5241-5252, 1982b.
- Francon, M., *Optical Interferometry*, Academic Press, New York, 1966.
- Greer, R. G. H., D. P. Murtagh, I. C. McDade, P. H. G. Dickinson, L. Thomas, D. B. Jenkins, J. Stegman, E. J. Llewellyn, G. Witt, D. J. Mackinnon, and E. R. Williams, ETON 1: a data base pertinent to the study of energy transfer in the oxygen nightglow, *Planet. Space Sci.*, 34, 771-788, 1986.
- Halliday, David, and Resnick, Robert, *Physics*, John Wiley & Sons, Inc., New York, 1960.
- Hauchecorne, A., M. L. Chanin, and R. Wilson, Mesospheric temperature inversion and gravity wave breaking, *Geophys. Res. Lett.*, 14, 933-936, 1987.
- Herzberg, G., *Spectra of Diatomic Molecules*, D. Van Nostrand Company, Inc., Princeton, New Jersey, 1950.
- Karl, J. *An Introduction to Digital Signal Processing*, Academic Press, Inc., London, 1989.
- Lindzen, R. S., Tides and gravity waves in the upper atmosphere, In *Mesospheric Models and Related Experiments*, Edited by G. Fiocco, European Space Research Institute, Frascati, Italy, pp. 122-129, Reidel Pub. Co., Dordrecht, Holland, 1971.
- Rees, M., *Physics and Chemistry of the Upper Atmosphere*, Cambridge University Press, Cambridge, 1989.
- Rishbeth, H. and O. K. Garriott, *Introduction to Ionospheric Physics*, Academic Press, New York, 1969.

- Smith, R. W., G. J. Romick, R. Viereck, and G. Hernandez, Measurements of temperature and wind at the mesopause by high resolution spectroscopy of the OH (6-2) and (8-3) bands, *EOS, Transactions, Amer. Geophys. Union*, 67, 319, 1986.
- Thomas R. and R. Young, Measurement of Atomic Oxygen and Related Airglows in the Lower Thermosphere, *J. Geophys. Res.*, 86, 7389, 1981.
- Vial, F., and J. M. Forbes, Recent progress in tidal modeling, *J. Atmos. Terr. Phys.*, 51, 663-671, 1989.
- von Zahn, U., K. H. Fricke, R. Gerndt, and T. Blix, Mesospheric temperatures and the OH layer height as derived from ground-based lidar and OH* spectrometry, *J. Atmos. Terr. Phys.*, 49, 863-869, 1987.
- Webb, W. L., editor, Stratospheric Circulation, *Progress in Astronautics and Aeronautics*, Vol. 22, 469-491, Academic Press Inc., New York, 1969.

Appendix B. Letters of Permission

9 Feb 93
Carolyn M. Vadnais
1173 Cardinal Drive, Enon, OH 45323
513-864-2604/513-255-2207

Dear Mr. Andrews:

I am in the process of preparing my thesis in the Physics Department at Utah State University. I hope to complete in the Spring of 1993.

I am requesting your permission to include the attached material as shown. I will include acknowledgments and/or appropriate citations to your work as shown and copyright and reprint rights information in a special appendix. The bibliographical citation will appear at the end of the manuscript as shown. Please advise me of any changes you require.

Please indicate your approval of this request by signing in the space provided, attaching any other form or instruction necessary to confirm permission. If you charge a reprint fee for use of your material, please indicate that as well. If you have any questions, please call me at the number above.

I hope you will be able to reply immediately. If you are not the copyright holder, please forward my request to the appropriate person or institution.

Thank you for your cooperation,

Carolyn M. Vadnais

I hereby give permission to Carolyn M. Vadnais to reprint the following material in her thesis.

From the text *Middle Atmosphere Dynamics*, Academic Press Inc., New York, 1987, Figures 1.3, 1.4, and 2.9.

Bibliographical Citation:


Andrews, D. G., J. R. Holton, and C. B. Leovy, *Middle Atmosphere Dynamics*.
Academic Press Inc., New York, 1987.

PLEASE TURN OVER

February 17, 1993

RE: Figures 1.3, 1.4 and 2.9

PERMISSION GRANTED, provided that 1) complete credit is given to the source, including the Academic Press copyright notice; 2) the material to be used has appeared in our publication without credit or acknowledgement to another source and 3) if commercial publication should result, you must contact Academic Press again.



Martha Strassberger
Contracts, Rights and Permissions
ACADEMIC PRESS, INC.
Orlando, FL 32887

18 FEB. 1993

182

9 Feb 93
Carolyn M. Vadnais
1173 Cardinal Drive, Enon, OH 45323
513-864-2604/513-255-2207

Dear Mr. Kato:

I am in the process of preparing my thesis in the Physics Department at Utah State University. I hope to complete in the Spring of 1993.

I am requesting your permission to include the attached material as shown. I will include acknowledgments and/or appropriate citations to your work as shown and copyright and reprint rights information in a special appendix. The bibliographical citation will appear at the end of the manuscript as shown. Please advise me of any changes you require.

Please indicate your approval of this request by signing in the space provided, attaching any other form or instruction necessary to confirm permission. If you charge a reprint fee for use of your material, please indicate that as well. If you have any questions, please call me at the number above.

I hope you will be able to reply immediately. If you are not the copyright holder, please forward my request to the appropriate person or institution.

Thank you for your cooperation,

Carolyn M. Vadnais

I hereby give permission to Carolyn M. Vadnais to reprint the following material in her thesis.

From the text *Dynamics of the Upper Atmosphere*, D. Reidel Publishing Co., Boston, 1980, Figure 2.5.

Bibliographical Citation:

Kato, S., *Dynamics of the Upper Atmosphere*, D. Reidel Publishing Co., Boston, 1980.



**Kluwer
academic
publishers**

Spuiboulevard 50
P.O. Box 17
3300 AA Dordrecht
The Netherlands

Telex: 29245
Telefax: (0)78-334254
Telephone (central): (0)78-334911

Bankers: ABN Bank, Dordrecht
Account Number 51.34.52.206

Postal Cheque Account Number 4447384

Chamber of Commerce Dordrecht
Commercial Register Number 51097

Telephone (direct): (0)78- 334 210
Date 25 February 1993

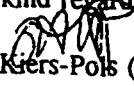
Mrs. C.M. Vadnais
1173 Cardinal Drive
ENON, OH 45323
U.S.A.

Dear Mrs. Vadnais,

With reference to your request (copy herewith) to reproduce material on which Kluwer Academic Publishers control the copyright, I confirm that you have our permission, free of charge, for the use indicated in your enquiry.

In all cases, including those where the original copyright notice cites the name of another, we request that you add this statement:
Reprinted by permission of Kluwer Academic Publishers.

With kind regards,


Odet Kiers-Pols (Mrs.)
Rights and Permissions

Encl.

9 Feb 93
Carolyn M. Vadnais
1173 Cardinal Drive, Enon, OH 45323
513-864-2604/513-255-2207

Dear Mr. Holton:

I am in the process of preparing my thesis in the Physics Department at Utah State University. I hope to complete in the Spring of 1993.

I am requesting your permission to include the attached material as shown. I will include acknowledgments and/or appropriate citations to your work as shown and copyright and reprint rights information in a special appendix. The bibliographical citation will appear at the end of the manuscript as shown. Please advise me of any changes you require.

Please indicate your approval of this request by signing in the space provided, attaching any other form or instruction necessary to confirm permission. If you charge a reprint fee for use of your material, please indicate that as well. If you have any questions, please call me at the number above.

I hope you will be able to reply immediately. If you are not the copyright holder, please forward my request to the appropriate person or institution.

Thank you for your cooperation,

Carolyn M. Vadnais

I hereby give permission to Carolyn M. Vadnais to reprint the following material in her thesis.

From the text *An Introduction to Dynamic Meteorology*, Academic Press Inc., New York, 1979.

Bibliographical Citation:

Holton, J. R., *An Introduction to Dynamic Meteorology*, Academic Press Inc., New York, 1979.

7 June 93
Carolyn M. Vadnais
1173 Cardinal Drive, Enon, OH 45323
513-864-2604

Dear Mr. Hernandez:

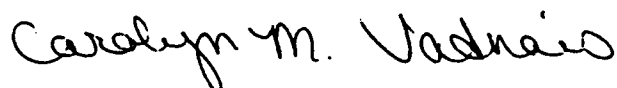
I am in the process of preparing my thesis in the Physics Department at Utah State University. I hope to complete in the Summer of 1993.

I am requesting your permission to include the attached material as shown. I will include acknowledgments and/or appropriate citations to your work as shown and copyright and reprint rights information in a special appendix. The bibliographical citation will appear at the end of the manuscript as shown. Please advise me of any changes you require.

Please indicate your approval of this request by signing in the space provided, attaching any other form or instruction necessary to confirm permission. If you charge a reprint fee for use of your material, please indicate that as well. If you have any questions, please call me at the number above.

I hope you will be able to reply immediately. If you are not the copyright holder, please forward my request to the appropriate person or institution.

Thank you for your cooperation,



I hereby give permission to Carolyn M. Vadnais to reprint the following material in her thesis.

From the text *Fabry-Perot Interferometers*, Cambridge University Press, Cambridge, UK, 1986, Figure 15.